

2014

High Resolution Maps of the Vasculature of An Entire Organ

Oppenheim N. Jacob

Follow this and additional works at: http://digitalcommons.rockefeller.edu/student_theses_and_dissertations



Part of the [Life Sciences Commons](#)

Recommended Citation

Jacob, Oppenheim N., "High Resolution Maps of the Vasculature of An Entire Organ" (2014). *Student Theses and Dissertations*. Paper 210.



HIGH RESOLUTION MAPS OF THE VASCULATURE OF AN ENTIRE ORGAN

A Thesis Presented to the Faculty of
The Rockefeller University
in Partial Fulfillment of the Requirements for
the degree of Doctor of Philosophy

by
Jacob N. Oppenheim
June 2014

HIGH RESOLUTION MAPS OF THE VASCULATURE OF AN ENTIRE ORGAN

Jacob N. Oppenheim, Ph.D.

The Rockefeller University, 2014

The structure of vascular networks represents a great, unsolved problem in anatomy.

Network geometry and topology differ dramatically from left to right and person to person as evidenced by the superficial venation of the hands and the vasculature of the retinae. Mathematically, we may state that there is no conserved topology in vascular networks. Efficiency demands that these networks be regular on a statistical level and perhaps optimal. We have taken the first steps towards elucidating the principles

underlying vascular organization, creating the first map of the hierarchical vasculature (above the capillaries) of an entire organ. Using serial blockface microscopy and fluorescence imaging, we are able to identify vasculature at 5 μm resolution. We have designed image analysis software to segment, align, and skeletonize the resulting data,

yielding a map of the individual vessels. We transformed these data into a mathematical graph, allowing computationally efficient storage and the calculation of geometric and topological statistics for the network. Our data revealed a complexity of structure unexpected by theory. We observe loops at all scales that complicate the assignment of hierarchy within the network and the existence of set length scales,

implying a distinctly non-fractal structure of components within.

To Joseph Goldstein and Norman Oppenheim, who brought me here.
and To Arnold Goldberger, who showed the way.

Acknowledgments

Many years back, when I was an overenergetic child, I would try to find the valves in my veins. My father, a surgeon, showed me how a vein that is cut off from behind will gradually empty upstream until it merges with another vessel or hits a valve. As long as you put pressure on the vein upstream of a valve, you can flatten any superficial vein in your hands or your feet. But why is this possible? Venous pressure is low, on the order of 5 to 10 mmHg, versus 70 to 110 mmHg in the arteries, and circulation in your veins is passive [61]. To prevent blood from falling back towards your extremities due to the force of gravity, there exist valves that allow flow only in one direction. This is the reason, for instance, that thrombosis can develop from sitting on an airplane for too long: blood collects above the veins in your feet and legs, in the absence of muscle movements to push it back towards the heart [33]. But I digress.

Another amusing but more puzzling demonstration is to examine the network structure of those same veins. I invite readers to put their hands in their lap, or otherwise below their heart, so that the veins in the backs of their hands fill with blood, rendering them more visible. A quick glance will show that the venation patterns differ, often to a great degree, between the left hand and the right. Common structures include one large vessel that curves across the hand with branches going to each finger; a large loop; and two smaller, independent trees, or even loops. As a case study, I present my hands in Figure 1.1. Note the pair of trees in the left hand and the loop in the right. Geometrically, these patterns are clearly quite different. This distinction is the principle by which retinal scanning works. The blood vessels (mostly capillaries) in each of your retinae are distinct from those in any other human.

It was observations of this sort that stoked my interest in vascular morphology; this thesis is the result. For this scientific curiosity, I owe a great deal to my father, Dr. Josh Oppenheim, my mother, Dr. Ellen Goldberger, and my grandfathers, Norman Oppenheim and Arnold Goldberger, both of whom, in a different world, would have received their own doctorates.

It takes a lot of work to turn a theoretical physicist into an experimental biologist. First and foremost, my thanks go to Marcelo Magnasco, who prodded me into turning an odd curiosity about

the veins in the backs of my hands into a thesis project. Perhaps most importantly, Marcelo understood which problems to assist me with and which to let me figure out on my own.

I would like to thank my friends and colleagues Carl Modes, Eleni Katifori, Pradeep Kumar, Thibaud Taillefumier, and Phil Kidd for helping me pretend to be a physicist these past five years. I suspect I learned more from them over happy hours than during the workday. From Carl and Pradeep especially I learned more than from any graduate course. The seminar series of the Center for Physics and Biology and the Fellows who organized it have been integral to my education. I have never seen a better collection of speakers.

I am also indebted to the Magnasco Lab as a whole, especially Alex Petroff, Carl Modes, and Leandro Alonso, whose comments, questions, and occasional skepticism spurred my work along, and greatly improved its presentation.

In the realm of biology, my thanks go especially to Jim Hudspeth, who served as chair of my thesis committee. He brought valuable anatomical and physiological knowledge and a healthy dose of skepticism. Two courses he taught at Rockefeller, one on neuroscience, the other on the origin of life, were the best courses that I took as a graduate student.

Not only was this work behind this thesis interdisciplinary, it involved building new equipment and an immense number of moving parts. I owe a deep debt of gratitude to numerous people at Rockefeller who provided their advice, technical knowledge, and specialty skills over the past five years, aiding me with the design, implementation, and execution of what had once been a set of vague plans, drawn up on Marcelos whiteboard.

In the construction of the apparatus, I am heavily indebted to Vadim Sherman of the Rockefeller Machine Shop, who machined many of the original parts, including the microtome head and the macroscope fluorescence unit. Many days of trading designs back and forth with Vadim led to a considerably better design than I could have envisioned when I started. In the past year, I have also leaned heavily on the assistance of Kunal Shah of the Fabrication Facility, who helped me laser-cut several adapters and three-d print numerous coarse-grained models of liver vasculature, one of which actually turned out successfully.

As everyone who has ever met me knows, I am a klutz. Anaesthetizing and perfusing rats did not come easily to me. I am deeply grateful to Alejandra Gonzalez and especially to Craig Hunter, who chose, sacrificed, and perfused numerous rats for me, even though it was not part of their job description. More than any other person, Craig Hunter was the keystone of this project.

My work was funded by the Rockefeller University Graduate Program, which supported me these past five years, and allowed me the freedom to pursue multiple side projects, and two pilot

projects of the Center for Clinical and Translational Studies (Towards a Detailed Quantification of Hierarchical Vasculature in 2010, and Mapping the Vasculome in 2013) that provided funding for my experimental work.

Choosing to go to graduate school is an act of calculated insanity. I owe Clinton Smith for showing me that it was the correct choice. I would be remiss not to thank the purveyors of liquid assets at the Rockefeller University Faculty Club, especially the recently retired Pat Griffin, one of the few people on campus with whom I could discuss politics without hiding my true opinions.

Finally, there are the people who kept me sane: my family (Josh and Ellen, my parents, and my sisters Rebecca and Shoshana), my friends both at Rockefeller and elsewhere in New York (especially Sam Zeitlin and Aaron Buchman, Alex Kirst and three Dans [Fraklin, Moulton, and Maass]), and my fiance, Joanna, all of whom helped to celebrate the highs and smooth out the lows during my time in graduate school. For this I am eternally grateful.

Table of Contents

Acknowledgments	iv
List of Figures	ix
1 Introduction: The Problem of Vascular Network Morphology	1
1.1 Four Features of Vascular Networks	2
1.2 Narrative Contents	4
2 Blood Vessels and Vasculature Networks	5
2.1 Anatomy	5
2.2 Current Techniques for Mapping	7
2.3 Applications of Vascular Research	11
3 The Theory of Hierarchical Distribution Networks	16
3.1 Random Networks	16
3.2 River Networks and Optimal Trees	18
3.3 The Problem of Quantifying Angiogenesis	22
3.4 Leaves and Loops	23
3.5 Vasculature in Three Dimensions	27
3.6 Analyzing Hierarchies	29
4 How to Image the Vasculature of Entire Organs: Serial Blockface Microscopy	31
4.1 Hepatic Morphology	34
4.2 Slicing	36
4.3 Imaging	38
4.4 Fluorescence and the Search for Signal	40
4.5 Automation	44
5 Image Analysis	50
5.1 What Exactly Are We Seeing?	52
5.2 The Nature of the Vascular Signal	54
5.3 Morphological Operations and Cleaning	61
5.4 Moving to Three Dimensions	66
6 Skeletonization	70
6.1 Algorithms	71
6.2 Digital Topology in Three Dimensions	73
6.3 Homotopic Thinning	76
7 From Skeleton to Graph	80
7.1 Finding Your Neighbors	80
7.2 Vertex Simplification, Edges, and Lines	82
7.3 Visualization	85

8	Analysis	88
8.1	Geometrical Properties: Vessel Radius and Length	89
8.2	Topological Properties: Loops and Network Structures	92
9	Prospects in Vasculomics	99
9.1	The Paucity of Theory	99
9.2	Separation of Scales	102
9.3	Where to Look for Perturbations	105
	Bibliography	107

List of Figures

1.1	Superficial Venation of the Hand	2
2.1	Simplified View of Vascular Network Morphology	6
2.2	Corrosion Cast of Liver Vasculature	9
2.3	Two Photon Studies of Cortical Microvasculature	10
2.4	Cartoon of Cancerous Vasculature	13
2.5	Sucrose Scaffolds	15
3.1	Examples of Random Graph Models	18
3.2	Strahler Stream Ordering	20
3.3	The Scheidegger Model	21
3.4	Radial Scheidegger Networks	23
3.5	Leaves with Highlighted Vasculature	24
3.6	Optimal Distribution Networks	25
3.7	Loopy Optimal Networks	26
3.8	Loop Hierarchies in Two Dimensions	29
4.1	Two Photon Image of Liver	33
4.2	Hepatic Autofluorescence Spectrum	33
4.3	Liver Lobules	35
4.4	White Light Imaging	41
4.5	Autofluorescence Imaging	42
4.6	Capillaries in a Liver Lobule	43
4.7	Imaging with Fluorescent Beads	45
4.8	Circuit Diagram of Automation Electronics	48
4.9	The Scanning Blockface Microtome	49
5.1	Example Slice of Liver	51
5.2	Red Channel of Liver Slice Image	52
5.3	Green Channel of Liver Slice Image	53
5.4	Ratio Channel and Region of Interest	55
5.5	Mean and Median Filters	57
5.6	Median Filtering	59
5.7	Initial Mask	62
5.8	The Erosion and Dilation Operators	63
5.9	The Opening and Closing Operators	64
5.10	Morphological Closing	65
5.11	Morphological Opening	65
5.12	Series of Aligned Images	68
6.1	Geometrical Skeletonization	72
6.2	The Jordan Curve Lemma and Digital Topology	74

7.1	VertexAnomalies	81
7.2	Two Proximate Triple Junctions	83
7.3	Diagram of the Largest Vessels	86
8.1	Vessel Radius Histogram	90
8.2	Vessel Length Histogram	92
8.3	Counting Loops	93
8.4	Topological Properties of the Vasculome	95
8.5	Topological Properties Continued	97
9.1	Volumetric Analysis	101
9.2	Finding Capillaries with a Macroscope	104

Chapter 1

Introduction: The Problem of Vascular Network Morphology

The efficient distribution of resources in any system requires a carefully designed architecture that reaches every point in the system and can distribute its cargo with minimal effort. While the principles of such networks are well understood in engineering and are beginning to be uncovered in plants, they remain poorly elucidated in the case of higher animals. If one compares the networks in the backs of one's hands, or turns Figure 1.1 where the author's are displayed, one immediately notices a dramatic morphological inconsistency between right and left and from person to person.

There are many geometric differences between the networks: one can measure different radii for the vessels, different branching angles, and different lengths between branch points. These differences though can be related by a smooth transformation. Thinner vessels can be dilated to match thicker ones; two merging vessels can be rotated and brought nearer one another. No amount of stretching, bending, or shearing of a loop, however, can turn it into a tree. This inability to turn the structures on the left into the ones on the right using smooth transformations implies that these two networks are *topologically* distinct [38]. A destructive transformation that rips the loop apart is necessary. In mathematical terms, the two are not topologically equivalent in any sense: neither homeomorphism, nor homotopy equivalence, nor homology.

These topological differences present a problem. One could easily imagine that the blood vessels differ from person to person in their exact placement, in how much they stray while connecting two points, in the tightness of their curvature, or in their branching angles, for instance. Geometric

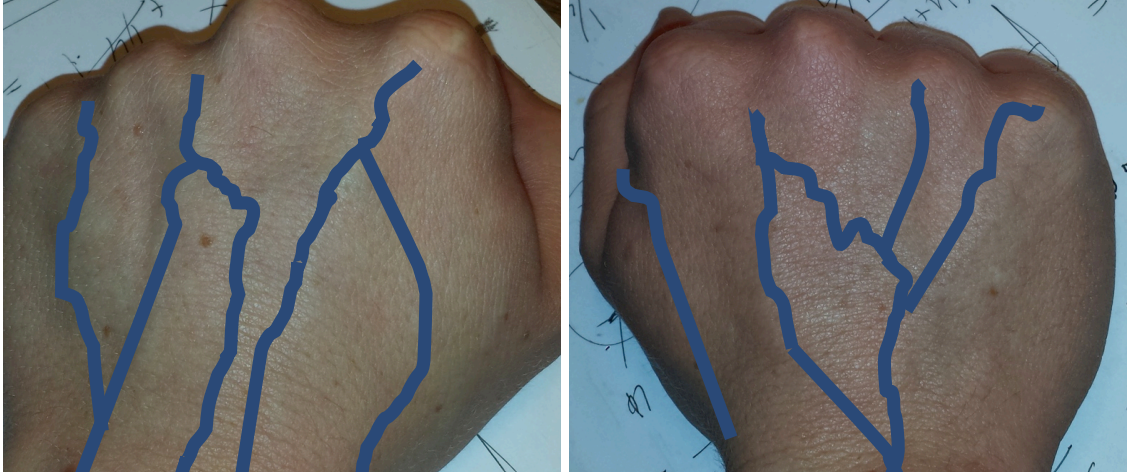


Figure 1.1. The superficial venation of the author’s hands. Veins have been highlighted in blue.

properties would not be preserved, but topological ones would be. Such topological consistency¹ might be what we would expect naïvely: a developmental plan and fluctuations that give each person a unique pattern.

1.1 Four Features of Vascular Networks

The lack of consistent vascular topology from person to person indicates that on some level these networks are random. This fact is well known in the medical community. We have been told that medical students today are given at least one cadaver to dissect with an extra femoral artery (the largest artery of the leg). This is a high-level structural abnormality affecting one of the largest vessels originating from the heart. It is also not a rare concern; 4% of individuals have an extra femoral artery, making an awareness of these abnormalities vital for surgeons [33].

A random network, unlike the choosing of random numbers, does not refer to a single ideal structure that we can study statistically. The space of random networks is the space of rules that define them and hence is infinite. Several major classes of models will be reviewed in §3.1 below; however, most of the well-known models are unsatisfactory and cannot be used as null models for vasculature. For instance, one could imagine randomly connecting pairs of points, as in bond percolation. If this probability of connection is sufficiently large, there will be a giant connected component. Unless this probability is very close to 1, however, not all of the points will be connected. Clearly, this is inappropriate for a vascular network, which must supply every “point” (or tissue) with nutrients. Even if we ensure universal connectivity, the vertices and edges

¹Vasculature in this model would still have to obey the geometric constraints of the tissue in which it is embedded: a minor venule would not cross the boundary of the liver

exist in an undefined, high-dimensional space. The vertices lack coordinates, and the edges lack radii and lengths. Mathematically speaking, the network lacks an embedding [38].

This observation leads us to a second feature of vascular networks: their geometrical and topological properties are deeply intertwined. This is a rare occurrence mathematically. Topology is the study of properties that are invariant under continuous transformations, whereas geometry is the study of the properties of space that are changed by those continuous transformations, such as position, length, and angle. Connections do exist in the form of the famous Gauss-Bonnet theorem relating curvature (a geometric property) to the genus (a topological one) and the small set of index theorems [38]. Geometric properties reflect hierarchy within networks: large vessels beget smaller vessels. The largest vessels either connect to the heart or supply entire organs, and the smallest vessels provide nutrients to tissues on the smallest scales [61]. At the same time, the instant a loop is added to a treelike network, it gains nontrivial topology² and is no longer simply connected. This loop perturbs the hierarchy as well, creating an ambiguity as to which vessel is upstream of the other.

As an example, consider optimizing the geometric properties of a network given a set topology. A set of points and connections is given. The goal is to minimize power dissipated by flow through the network while minimizing the cost of construction, a function of the conductivity of each edge. If we demand treelike topology, the most central vessels will be highly trafficked and will have high connectivity. These vessels would branch into smaller ones with appropriately smaller connectivities. In the case of a looped topology, the redundancy provided by having multiple connections between each pair of vertices would reduce the need for connections of high conductivity. Network topology would drive geometry. Although this example is contrived, the same principles are observed in more naturalistic models of leaf venation [26], where demands for redundant connections between vertices (reflected in the network’s topology) alter its geometry.

The question of optimality reflects a third principle of vascular networks: they are on some level efficient. The heart is of limited size and one’s body has limited resources. Yet they must also be space filling, as mentioned above. These constraints greatly reduce the space of possible network models. The interplay between topological randomness and efficiency with the condition of being space filling is what makes the structure of vascular networks fascinating. Ultimately, these criteria underlie the richness of the mathematical description of vascular networks and the connections between geometric and topological properties. A complete analysis requires not only biological data to inform the model and its constraints, but also pure mathematics to analyze the structure and

²It can no longer be deformation retracted to a single point

physics to solve the inverse problem of its function and development.

We have taken the first steps in this effort, devising the first method of mapping the vasculature of entire organs from images through cleaning, alignment, and skeletonization to reduction to an analyzable mathematical graph. Although the analysis is still preliminary and far from complete, we can see already tantalizing hints of an unimagined structural complexity from even the most basic statistics.

1.2 Narrative Contents

This thesis is organized as follows. This chapter is followed by an overview of the state of medical knowledge about vascular networks as well as a brief overview of vascular biology, current techniques for examining its morphology, and the potential (medical) applications of an improved understanding of vascular morphology. The next chapter reviews our knowledge of random networks and hierarchical distribution networks, uniting mathematical models with data from river networks and leaves. The fourth chapter describes our experimental apparatus, as well as a brief overview of failed techniques and potential improvements in the future.

The next three chapters (5-7) cover the image processing portion of this effort. Segmentation, alignment, cleaning, and attachment using morphological operations are in chapter five. Skeletonization and the isolation of individual vessels comprise chapter six, along with a brief overview of digital topology in three dimensions. Chapter seven covers the surprisingly rich problem of turning a skeletonized image into a mathematical graph of edges and vertices.

The last two chapters (8-9) are a tour of the analyses we have performed (and are performing) as well as an overview of next steps experimentally, computationally, and theoretically for the future.

Chapter 2

Blood Vessels and Vasculature Networks

2.1 Anatomy

In the classical model of circulation, dating from Harvey [22], blood is pumped throughout the body by the heart. It is distributed from the heart through a series of arteries that subdivide, forming the finer grades of arterioles. These again ramify to form meshed networks of capillaries or sinusoids depending on whether they are lined. The deoxygenated blood from these vessels is collected by the venules which repeatedly merge, form larger veins, and eventually feed back into the heart. Venous blood from the spleen, pancreas, stomach, intestines does not drain directly to the heart: it is not even fully deoxygenated. Instead, these vessels coalesce into the hepatic portal vein, which provides most of the blood supply to the liver, which is in turn drained by the hepatic vein (for details see §4.1) [61]. This network can be seen in Figure 2.1.

The anatomy of individual vessels varies throughout the body. The lining of a vessel varies with its size, the larger vessels having thicker and more complicated linings. Arteries are lined with smooth muscle and pump blood by peristaltic action. Arteries are surrounded by afferent nerve fibers, which in some places serve as baroreceptors, chemoreceptors, and mechanoreceptors and can specifically dilate certain vessels. Many arterioles are termed resistance vessels; they are lined with sphincters that control the flow into a capillary bed [61]. This ability of the vascular system to monitor and control flow points to a level of sophistication that we expect to see reflected in the network morphology. The lining of veins is considerably thinner than that of arteries. They rely on

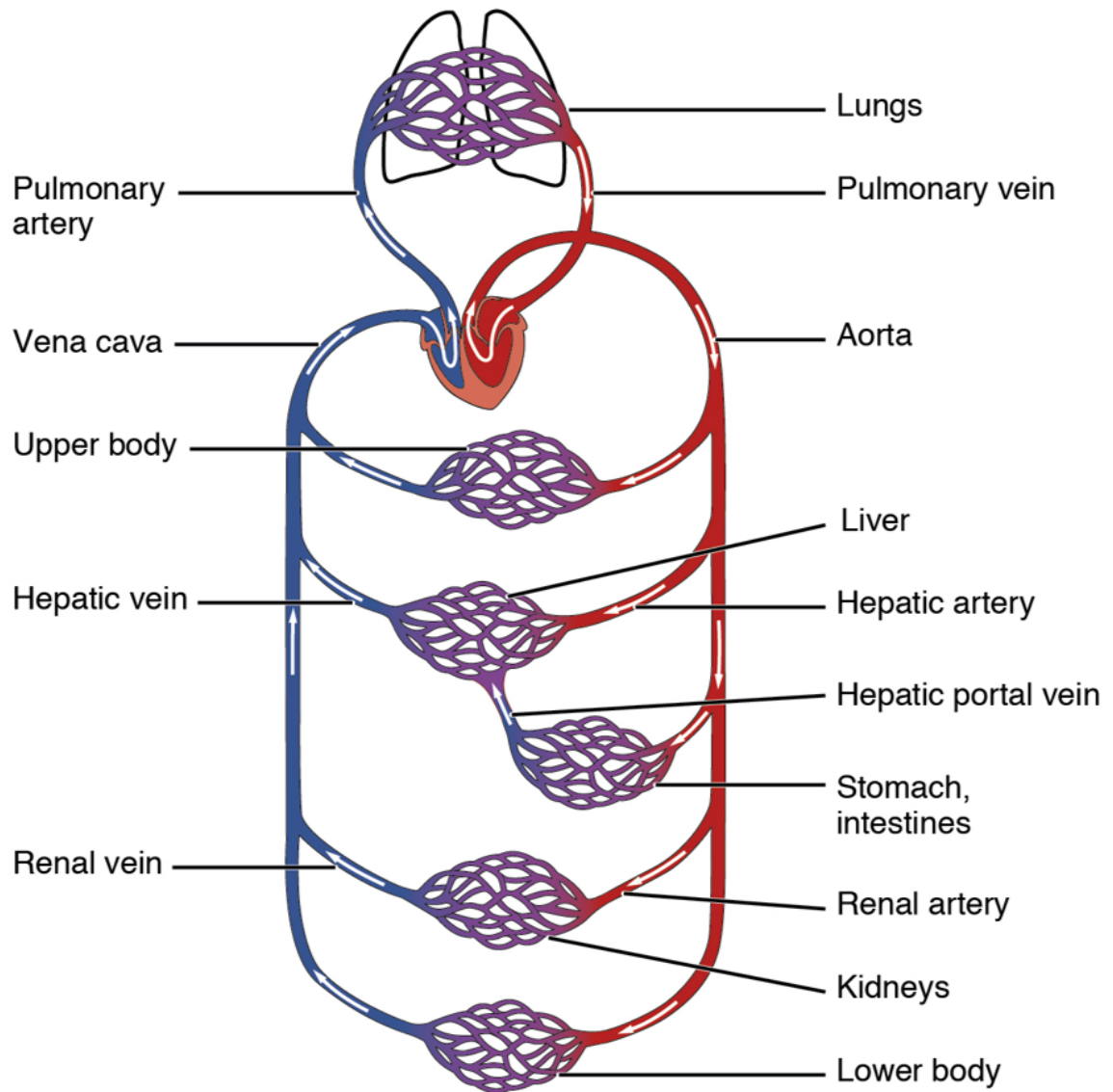


Figure 2.1. A Cartoon of Current Knowledge of Vascular Network Morphology. While this is an admittedly crude drawing, it emphasizes what we do not understand about vascular morphology. We know there are large vessels that branch somehow between each tissue or organ and the heart. Within these tissues, there is a loopy mesh of capillaries in which flow is not clearly arterial or venous (hence purple in this figure). Between the scale of the largest arteries and veins that branch from the heart and to the level of the capillaries within tissues and organs, little is systematically known. Image from [14]

passive flow, with valves, residual blood pressure, and the contractions of nearby muscles moving blood back to the heart. True capillaries are lined with a thin lumen; in many organs, such as the liver and other elements of the digestive tract, the capillaries are not lined continuously (or at all) and are termed fenestrated capillaries (or sinusoids) respectively.

This elegantly simple picture is complicated by a number of distinctively non-treelike components. The arterial network is definitively not a tree. Anastomoses, or connections between vessels, are prevalent throughout the body, especially in the joints, to ensure continuous flow whether the joint bent or flexed, the abdomen (among the vessels feeding the digestive organs), and the brain. They equalize pressures between arteries and ensure a constant supply of blood. Among smaller vessels, the treelike model fails completely, as anastomoses are common: Gray’s Anatomy describes it as a “close network.” The most important of these arterial anastomoses is the one that regulates the blood supply to the brain, the circle of Willis. There exist also shunts between the arterial and venous systems. For instance, many capillary beds have a preferred channel considerably wider than a typical capillary through which blood is directed by precapillary sphincters during times of low functional demand. Larger shunts, or arteriovenous anastomoses, are under the control of nerve fibers and allow the redirection of blood under the control of the nervous system. Classic examples of these include the shunts used for thermoregulation that move blood from your core to your periphery, turning your skin red when overheated, and from your periphery to your core, turning your skin white when cold. Similarly, blood flow to the erectile tissue in the genitals is controlled by arteriovenous anastomoses [61, Chapter 6].

Beyond this level of specificity, anatomy texts generally focus solely on the general patterns obeyed by the arteries and veins throughout the body¹ [33, 61]. While the network of the largest vessels is itself not completely stereotyped (as seen by the example of the femoral artery), it is conserved enough for maps of the largest vessels to prove useful. The network as a whole, though, lacks proper description. Mapping the vascular system should be done on all scales, from the largest vessels that branch from the heart to the smallest capillaries, 5 μm in size. We must be capable of mapping large volumes of tissue but at moderately high resolution.

2.2 Current Techniques for Mapping

The oldest technique for studying blood vessel networks is corrosion casting. It was first developed in the 17th century by Frederik Ruysch, the discoverer of valves in the venous and lymphatic systems

¹The British editions of Gray’s Anatomy have a short chapter on vascular network morphology covering the various types of anastomoses and the appearance of microcirculation. In my experience, most anatomy texts lack even this.

who filled arteries and veins with wax by mouth and a primitive bellows. Today, the scientist fills the blood vessels with a resinous compound by perfusion. The tissue is then placed in an acidic bath that eats away the tissue, leaving only the resin in the blood vessels. The resulting casts are beautiful, as in Figure 2.2, but ultimately two dimensional. As the vasculature is on some level space filling, vessels will always obscure the ones behind them. In a large and detailed-enough corrosion cast, the background has the appearance of out-of-focus resin. No amount of optical imaging would give the structure of a corrosion cast. It would have to be serially sectioned and imaged, which begs the question of why the cast was made in the first place. When such casts are used in research today, it is to study gross morphological differences in the vasculature, such as in colitis, where changes are easily apparent and act on the periphery of the region casted [27]. Alternatively, the cast is sliced open, and the exposed region is assumed to be indicative of the overall structure [23], characterizing a three-dimensional region based on the statistics of a two-dimensional slice.

Standard medical imaging techniques such as sonogram, CT, and MRI are all useful at covering large areas but unable to give sufficient resolution. For a sonogram, the resolution is measured as an RMS accuracy and is usually $\sim 250\text{ }\mu\text{m}$, two orders of magnitude too large. The resolution of CT is limited by the quality of the detector and the strength of the x-ray source used. The resolution can be determined by the size of the sample divided by the size of the grid used, or 512×512 pixels per slice normally. If we were to place a lobe of rat liver 2 cm on a side in a CT, our resolution would $20000/512 \approx 40\text{ }\mu\text{m}$ on a side at best. CT is also disadvantageous because of its lack of contrast for vasculature (see below). A similar calculation applies for MRI, though again contrast is an issue. We placed the largest lobe of a mouse liver in gadolinium, a contrast enhancer, then left it over the weekend in a 7 T MRI at Weill Cornell Medical School. We were able to recover only the largest branch of the portal tree with an effective resolution (smallest feature size) in the hundreds of microns, less than one decade of spatial resolution.

An early pioneer in the study of fractals, Heinz Otto Peitgen, used a combination of sonogram and CT to map vasculature. Much of his efforts were focused around devising clever methods based on the topology of vascular trees to segment vasculature from noisy data [54]. He was able to recover the first three generations of the portal tree in humans, implying a resolution in the millimeters or hundreds of microns. After these successes, he turned his efforts to surgical planning and the identification of large vessels in tissue from pre-surgical CT scans [40]. The weak signal-to-noise ratio in Peitgen’s imaging methods, necessitating complicated segmentation procedures, suggests we should look elsewhere for an experimental technique.

Another option is micro-CT, a special configuration of CT that can allow for micron resolution.



Figure 2.2. Corrosion Cast of Hepatic Vasculature. This close-up on a piece of a corrosion cast shows the complexity and tortuousness of many of the blood vessels inside the liver. Note the omnipresence of loops especially. At the same time, it shows why corrosion casts are useless for mapping vasculature. One simply cannot see behind the outer couple of layers; vessels obscure the ones behind them. For a large enough corrosion cast, after a certain distance, the background appears to be all vessel, as in the upper left. Image from [45]

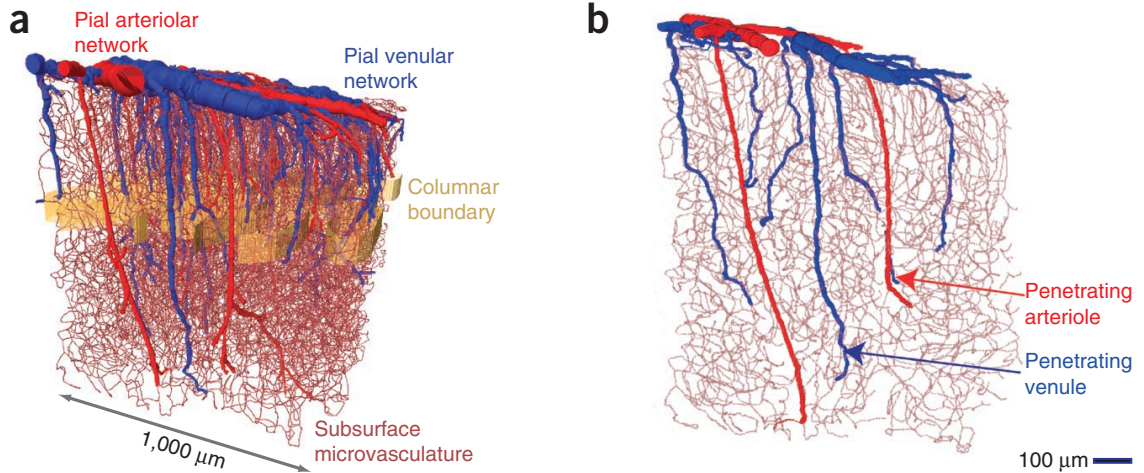


Figure 2.3. Two Photon Microscopy of a 2 mm^3 cube of mouse cortex, penetrating arteries and veins colored red and blue respectively. While the overall resolution is $1\text{ }\mu\text{m}$, the full range of vessel sizes was not captured. The highly looped structure of the capillaries may be seen in the uncolored vessels. Figure from [6]

Here again, we are limited by the resolution of the output images, which lies somewhere between 512 and 2000 pixels, due to computational issues in converting Fourier modes taken at a range of angles into a map in real space. At micron resolution, this would mean putting 1 mm^3 pieces of tissue serially into a scanner. While each individual scan would not take more than an hour, the reconstruction time scales with the number of voxels, or the resolution cubed, implying approximately a day for each cube used. In order to get the largest vessels, even in a mouse liver, we would need to subdivide our tissue sample into cubes without damaging the edges, properly preserve each one, and reassemble them in three dimensions [12]. While not impossible, this method is clearly impractical.

While limited in the total area it can capture at a time, two-photon imaging is a potentially useful technique. By leveraging the natural autofluorescence in the liver or perfusing the animal before sacrifice, beautiful, high-resolution images of the surface may be taken. The strong autofluorescence signal greatly inhibits optical sectioning, the main use of two-photon microscopy, however. An example may be seen in Figure 4.1. The Kleinfeld group at UCSD has used this method to map cortical capillary networks and to find penetrating arterioles and venules in the cortex [5]. The volume of tissue that is scanned, however, is still in the cubic millimeters, far too small to cover the full range of vascular features, as can be seen in Figure 2.3. This is despite their imaging over 2000 cubes at micron resolution, stitched together to form the image shown. Larger vessels merely pass through the cube of data studied; proper statistics cannot be calculated for them. Similarly, disconnections were found for the smallest vessels, which required tracing by hand [6].

The difficulty inherent in large-scale vascular imaging originates in the competing demands we have seen above. The system must be capable of imaging large pieces of tissue and the largest blood vessels within in order to capture the entire vascular tree. At the same time, it must have moderately good resolution: capillaries are approximately 5 μm in size, necessitating a resolution around one to two microns at least. We are looking for features whose size ranges over three orders of magnitude, in the case of the rat, or more in larger organisms. These requirements place us in a valley between the two major classes of imaging techniques: those that give extremely high resolution, up to the wavelength of light used, but over very small areas (micro-CT, two photon) and those that are capable of imaging large areas but only at resolutions in the tens to hundreds of microns (MRI, Sonogram).

2.3 Applications of Vascular Research

If you ask a doctor about blood vessels, they will quickly begin speculating about how their favorite poorly understood disease has a strong vascular component. This reaction is a reflection of our ill knowledge about the structure of vascular networks. How can one properly study the vascular component of a disease when they do not know what healthy vasculature looks like outside of the cell types present in the linings of arteries and veins? Network abnormalities may be detectable by a trained specialist who recognizes patterns in the vasculature, but they are not generally identifiable: we do not even know what forms they take. Without a baseline, we cannot even begin to look for aberrant vasculature.

One example of a disease with a clear vascular component is cirrhosis of the liver. A build-up of toxins, usually alcohol, or a disease such as hepatitis kills healthy liver tissue. When the body attempts to repair damaged hepatocytes (the main cell type of the liver see §4.1), thick bands of fibrous scar tissue form between repair sites or nodules. These fibroses impede the flow of blood throughout the liver, dramatically increasing the pressure in the portal vein. In response to this change in venous pressure, new anastomoses form between vessels in the liver as well as between veins in the stomach and esophagus that feed into the portal vein. Clearly, a better understanding of healthy vascular morphology would be useful in understanding the progression and treatment of cirrhosis. Additionally, while cirrhosis may be diagnosed from blood tests and ultrasound scans of the liver, the gold standard for diagnosis remains biopsy [9]. Typical biopsy plugs are of the order of a centimeter long and at least a millimeter in diameter (corresponding to a 16 gauge needles) [48]. Since cirrhosis causes remodeling of vascular architecture, one can imagine using these same biopsy

plugs, mapping the vasculature, and comparing the statistics of the network morphology to those of healthy liver tissue. Since the smallest vessels are on the order of $5\text{ }\mu\text{m}$ in size, only a small plug would be needed, around one millimeter on a side, to gain good statistics.

This same kind of analysis could be repeated for any number of diseases, both to test for a vascular component and, if one is found, as a method of biopsy. Similarly, understanding how disease shapes vasculature would allow us to study how diseased tissue is supplied (or not) with nutrients and how waste products are removed. This interaction between topology and disease can be seen clearly in the case of cortical vasculature in the mouse in work done by the Kleinfeld group. Capillary networks in the neocortex lie in layers parallel to the surface and are effectively two dimensional honeycomb lattices. They are connected to other layers and a central blood supply via penetrating arterioles, running perpendicularly to them and spaced on the order of $500\text{ }\mu\text{m}$ apart. While the ablation of a capillary does not harm any tissue, because of the redundancy in the lattice, ablating an arteriole kills off an entire region of tissue, as a patch of the capillary network is no longer supplied with blood. This causes a small stroke. One can easily imagine similar interactions between network structure and disease [5].

A similar question arises when considering cancer. It has long been hypothesized that cancers grow aberrant and abundant vasculature. Hence, inhibiting angiogenesis should be a good method of treatment. This line of argument was first proposed by Judah Folkman in the late 1960s [37]. A cartoon of this hypothesis from a review in *Nature Medicine* can be seen in Figure 2.4 [24]. Problematically, however, we lack a good definition of what is truly aberrant. If you consider the images in the top row of Figure 2.4, this issue becomes clear. It is assumed that normal, healthy vasculature is rigidly hierarchical with stereotyped bifurcations and branch lengths and is completely treelike with no loops whatsoever. This assumption runs clearly counter to the evidence from leaves (Figure 3.5), corrosion casts of vasculature (Figure 2.2), and our own evidence about loops on all scales within vasculature (§8.2). The “abnormal” vasculature in the upper-right-hand panel on some level looks healthier than the “normal” vasculature in the upper left panel. Similarly, the existence of real endothelial anomalies in cancerous vasculature [37] should not predispose us to belief that the network is definitively irregular. Perhaps these network abnormalities are being detected as a result of more resources being poured into the study of tumor vasculature than healthy vasculature. Lacking a proper point of reference, an overly simplistic, treelike model of vasculature is assumed. This is not to state that we in any way believe tumor vasculature to be normal. We are simply asserting agnosticism until a proper quantitative metric to compare healthy to cancerous vasculature is created.

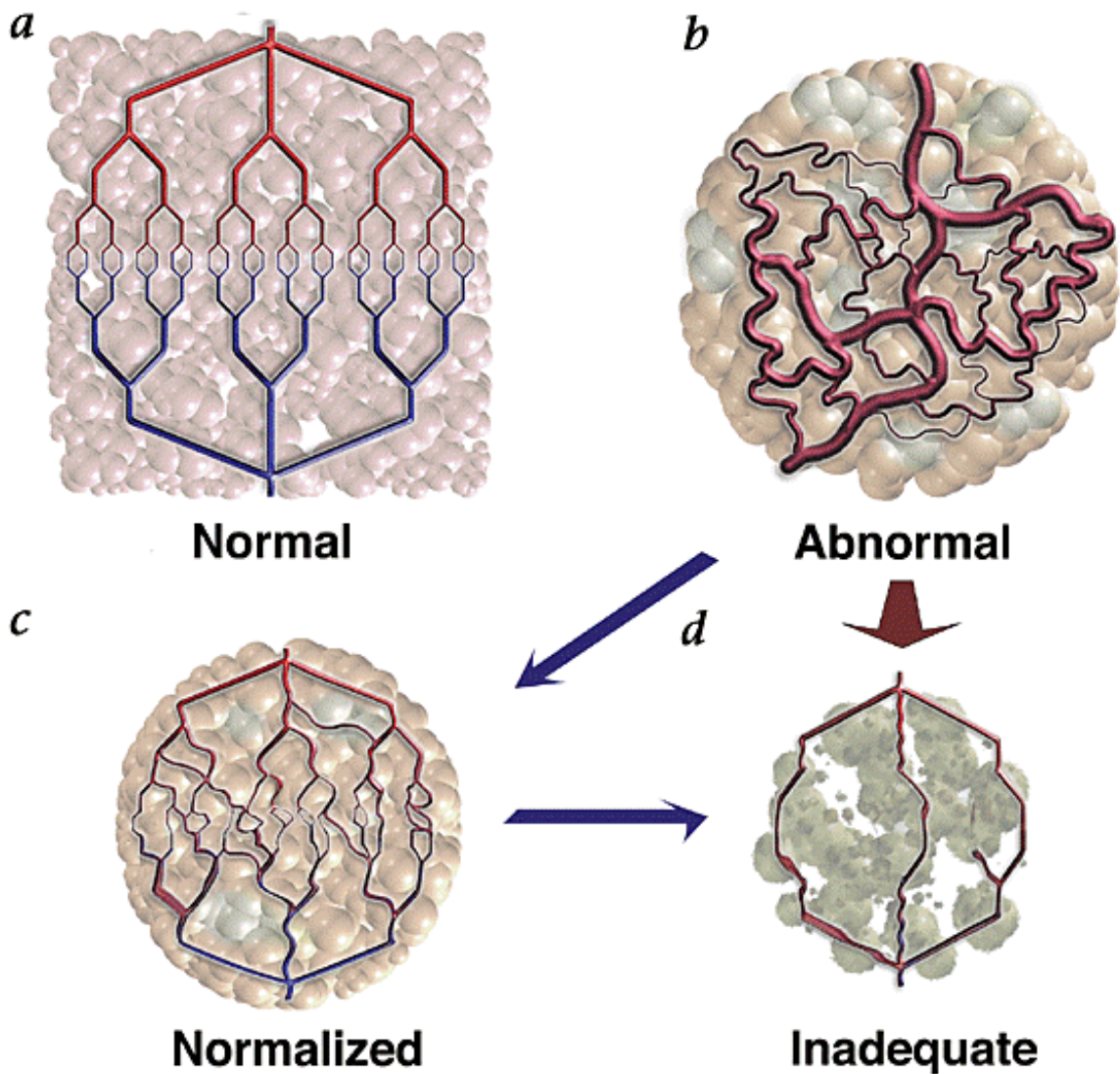


Figure 2.4. A Cartoon of Cancerous Vasculature from a recent Nature review. Note the assumption that normal vasculature is rigidly hierarchical, always bifurcating, and completely loopless. These hypotheses will be tested throughout and found wanting. If we consider looped, anastomosed, and not rigidly hierarchical (or even rigidly arterial or venous) vasculature to be the norm, the abnormal vasculature in the upper-right-hand panel seems far less “abnormal,” and perhaps even more normal than the “normal” vasculature. Figure from [24].

If systematic changes in vasculature between cancers and their host tissues do exist, we again could use analysis of the vasculature in biopsy plugs as a method of diagnosis. It is also possible that the presence of a tumor induces the growth of vasculature in nearby host tissue to increase its blood supply. Such abnormalities could also be detected and used as a method of diagnosis provided a quantitative metric.

Beyond the realm of disease, the main application of vascular research is in artificial organs. We are now able to cause cells to differentiate into various types based on the application of chemicals or growth on a specific substrate. Entire artificial tissues and organs can be grown in the lab. That is, entire tissues and organs lacking all vasculature above the level of capillaries. While we are able to generate artificial capillaries, to cause differentiated cells to leave spaces for sinusoids and for the endothelial cells necessary to line capillaries, we are still unable to generate hierarchical vasculature. Capillary networks are utterly insufficient to supply nutrients and remove waste from tissues in three dimensions. A flat sheet of cells can exist within the diffusive boundary layer of a nutrient bath, with capillaries assisting the local flow of nutrients and waste, while a three-dimensional organ cannot. Neither the experimental biologists that grow artificial organs [10, 64] nor the computational ones that model cellular growth and differentiation [1, 32] can create a program to generate hierarchical vessels: the large vascular “trees” (looped, of course) that service natural tissues [10].

Currently, there are various workarounds to this problem. Cells may be grown in mono- (or bi- or tri-) layers on a nutrient bath, replacing vascular advection with diffusion. This is what was done to create the first artificial hamburger and is a large part of why that project costs so much. In three dimensions, small organoids are grown that can be kept within the diffusive boundary layer but remain far too small to be effective transplants [64]. Artificial organs may also be grown on a scaffold built from various biological materials or even decellularized tissue, examples of which are shown in Figure 2.5. Here, biopolymeric tubes form a random network. Endothelial cells grow along them, eventually digesting the substrate, leaving gaps that become arteries and veins. This imprinting of the vasculature structure could, at the very least, be improved by a better understanding of vascular network morphology [39, 53, 64]. Fundamentally, what is lacking is a good understanding of angiogenesis. Before we tackle the growth of the vascular system, however, we must know what it looks like and how to characterize it. We will begin that effort by reviewing the state of current research about random graphs, hierarchical distribution networks, and vasculature from the theoretical and computational points of view.

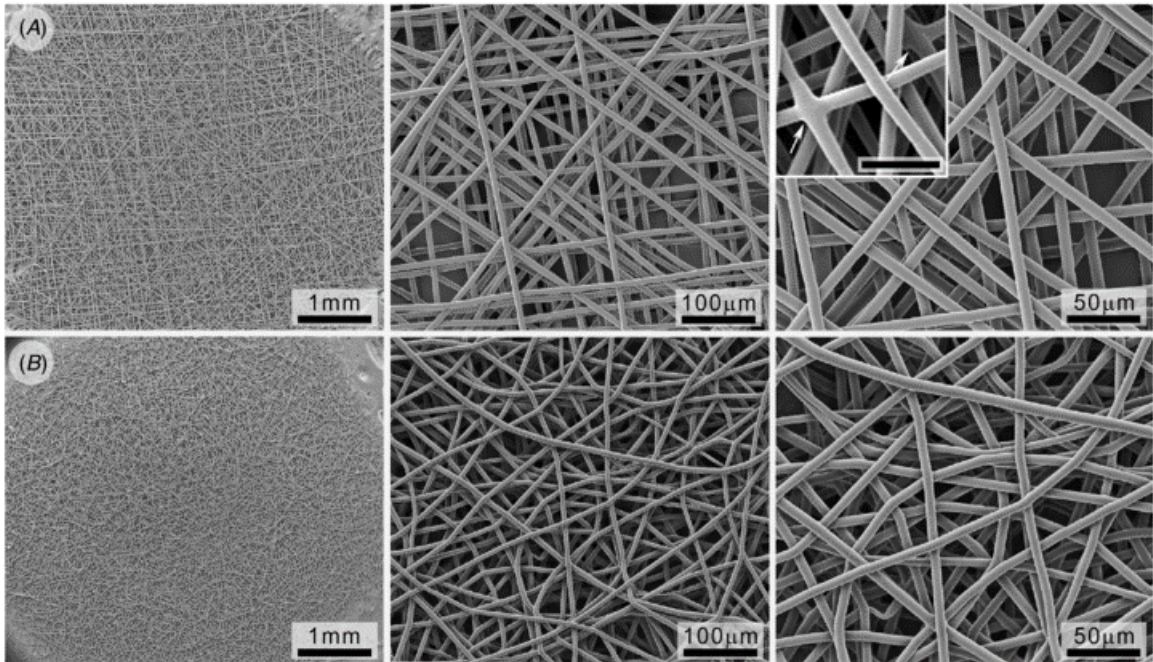


Figure 2.5. Scaffolding Used in Artificial Organs. Unlike Capillaries, artificial hierarchical vasculature cannot be grown from cell culture. The hierarchical vessels must be planned ahead of time. This is accomplished by laying out a matrix, frequently random, of sucrose (or other biopolymer) tubes and inducing the growth of endothelial cells along these tubes. When the sucrose dissolves, these tubes become hierarchical vessels, albeit with far from natural statistics, or network morphology. Figure from [39].

Chapter 3

The Theory of Hierarchical Distribution Networks

In the previous chapter, we reviewed the state of medical knowledge about vascular network morphology, its importance, and our ability to grow it *in vitro* and *in vivo*. We now turn to the state of theoretical knowledge about vascular and related networks. What unites blood vessels, leaf venation, and even river networks is that they are systems for distributing resources between a central point (the heart, the stem of a leaf, or the mouth of a river) and disparate, space-filling branches. All of these networks are *hierarchical*. Small vessels feed in to medium ones, which in turn feed into larger ones, etc. More important branches carry significantly more volume and are considerably wider. We will begin by reviewing the most important classes of random graph models and why they are inappropriate for describing hierarchical distribution networks, then proceed to look at cases from the simplest, namely river networks which are two dimensional and lack loops, to the more complicated, such as leaf venation which is heavily looped in many cases but still two dimensional, to the most complicated, the three-dimensional vasculature of higher organisms.

3.1 Random Networks

Unlike selecting random numbers, drawing a random graph admits a far greater space of possibilities. One can imagine taking a set of points, perhaps with locations that are themselves random, and connecting them with a certain probability. This is far from the only option. Graphs can be grown with new nodes attaching preferentially according to a certain probabilistic rule. They can also

be randomized, where a regular lattice is rearranged into a new, disordered structure. These three methods, which certainly do not comprise all of the space of random graphs, constitute, however, three of the most important classes of random graphs, the Erdős-Rényi, Barabási-Albert, and Watts-Strogatz models respectively.

The Erdős-Rényi model is historically the oldest and is closely related to the problem of percolation in physics. We imagine a set of points lying in some arbitrary space and connect pairs of them with a probability p . As one would expect from the percolation analogy, a giant connected component is found along with scattered smaller components and isolated nodes. The degree distribution is binomial, with mean pN . The large number of connected components in this model warns us away from a too-simple account of vascular development: simply connecting points, such as tissues in the body, is not sufficient to even ensure overall connectivity [20].

One way to ensure universal connectivity is a lattice. In a lattice, however, there are no long-range connections, so transmission across the network is very slow. This effect is what made capillary networks spectacularly unsuited for growing entire artificial organs and tissues. The Watts-Strogatz, or small world network, corrects this by introducing sparse long-range connections. It is generated by taking a lattice, where each node connects to a certain number of its nearest neighbors, and randomly permuting some fraction of the links. This process keeps the clique-y, local nature of most connections while providing enough long range connection to greatly decrease the diameter of the graph. Social networks, be they Facebook or authorship connections between researchers, are best understood as Watts-Strogatz style networks. For certain kinds of distribution systems, such as a telephone system, a Watts-Strogatz type network could be useful [62].

Both of these models, however, make no reference to demand or a preference for connectivity to certain nodes. The Barabási-Albert is characterized by preferential attachment. A small, initially completely connected core is augmented by new nodes, each of which connects to n others with probability determined by their degree. This “rich get richer” rule of network growth yields a power-law degree distribution with a few highly connected nodes and most nodes only having one or two at most. This model is a useful description of, for instance, internet hyperlinks, metabolic networks in cells, and scientific citations. It is not local, but it does ensure rapid passage between any pair of nodes through a series of hubs [3].

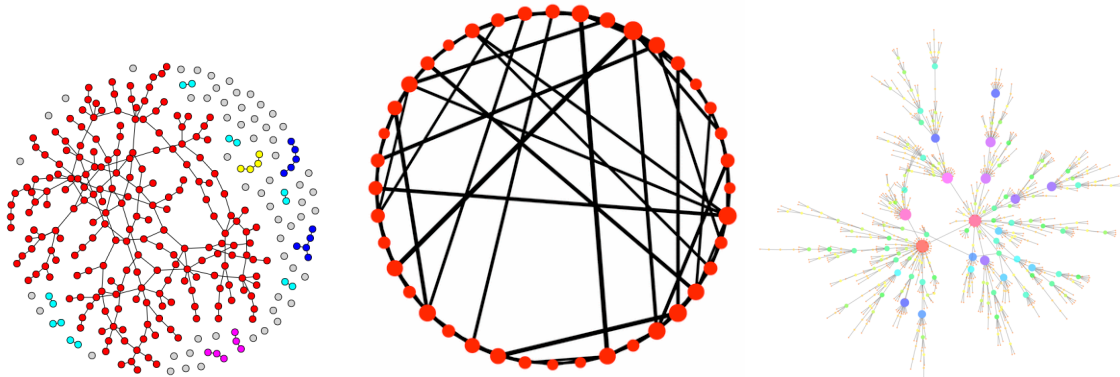


Figure 3.1. Three important classes of random graph models are pictured. At left is the Erdős-Rényi Model with connected components colored by size. In the center is the Watts-Strogatz Model, here showing the original lattice with connections between a point and its four nearest neighbors having been rewired. At right is the Barabási-Albert Model, mimicking a cellular metabolic network with the largest nodes colored by degree. From left to right, figures from [58], [62], and [41] respectively.

3.2 River Networks and Optimal Trees

All of the above models are purely topological; they are only concerned with the links between nodes in an arbitrary, high-dimensional space. There is neither a notion of weights on the links, nor is there even an embedding. This divorce from geometrical properties and indeed physical processes underlies their disutility in describing hierarchical distribution networks. A purely geometrical model, arising from the study of river networks, the Scheidegger Model¹, has been far more successful in providing a control case for understanding hierarchical distribution networks throughout nature.

It has long been noticed that networks of rivers, over a large range of length scales, observe certain statistical regularities in their morphology, relating the distances between branch points, the number of branches of a certain size, and the area drained by consecutive branches. Provided a properly defined hierarchy, known as Strahler stream ordering (see below), these relations may be parametrized either in terms of segments between any pair of branch points or only “important” ones where the stream impinges on others of equal or higher order. These formalisms, respectively Tokunaga’s and Horton’s Laws, have been shown to be equivalent [17].

One can imagine defining a hierarchy for a treelike network based on the volume of flow in each link or geometrically in terms of the number of upstream links it drains. This system is known as Horton (or Shreve) stream ordering and is not particularly useful. As one moves down a tree towards the mouth, the volume of flow, or the number of nodes upstream, increases exponentially. Arithmetically distributed order classes are thus a poor descriptor of the hierarchy (and highly

¹The Fundamental Group, π_1 is always trivial for the Scheidegger model as there are no loops

sensitive to multiplicative noise) [49]. Rather, we desire something that scales logarithmically [43]. This criterion is intimately related to the fact that the exponential growth of trees will always outstrip the slower, algebraic growth of the space they are embedded in. We may define the proper ordering, known as Strahler stream order, as follows. Give the tip of every branch a value of one. When two streams intersect, the resultant stream takes the higher of the two parent streams' orders. If they are of the same order, it is augmented by one. This system gives the desired scaling as well as confirming our intuition about which streams are “important;” an example is displayed in Figure 3.2. Expressed in term of segments of Strahler order i , Horton's Laws are:

$$l_{i+1} = r_l * l_i \quad (3.1)$$

$$a_{i+1} = r_a * a_i \quad (3.2)$$

$$n_{i+1} = r_n * n_i \quad (3.3)$$

Here l , a , and n are respectively the average length, area drained (or flow volume), and number of streams of order i , and the values r_l , r_a , and r_n are termed the length, area, and bifurcation ratios. Empirically, these values for natural river networks are tightly constrained, perhaps reflecting some optimality principle arising from the physics of their formation. Strahler stream ordering thus provides the proper metric for understanding river networks and quantifying hierarchy, a feature we would like to replicate in other classes of natural distribution networks. The example of river networks should also caution us away from expecting perfect hierarchical relationships. Work by Dodds and Rothman has shown that Horton's Laws only hold for intermediate values of the Strahler order with exponential cutoffs present at both the highest and lowest orders [18, 49].

The Scheidegger model provides a convenient framework for understanding the origins of these relations, giving in some sense “mean-field” values for the exponents that, while not exact, are close to the physical values and obey the same sum relations. We imagine growing a river network on a grid. Consider one direction to be downhill, z , as if the lattice lies on the side of a gently sloping hill in two dimensions, unvarying in the x direction. At each point, a drop of rain falls and then moves downhill, executing a random walk in the x direction, as shown in Figure 3.3 [52]. Since the network is a collection of convergent random walks, the Horton's Laws exponents may be calculated analytically from field theoretical techniques. Deviations from the Scheidegger Model values can inform us about the differences between natural systems and convergent random walks [51].

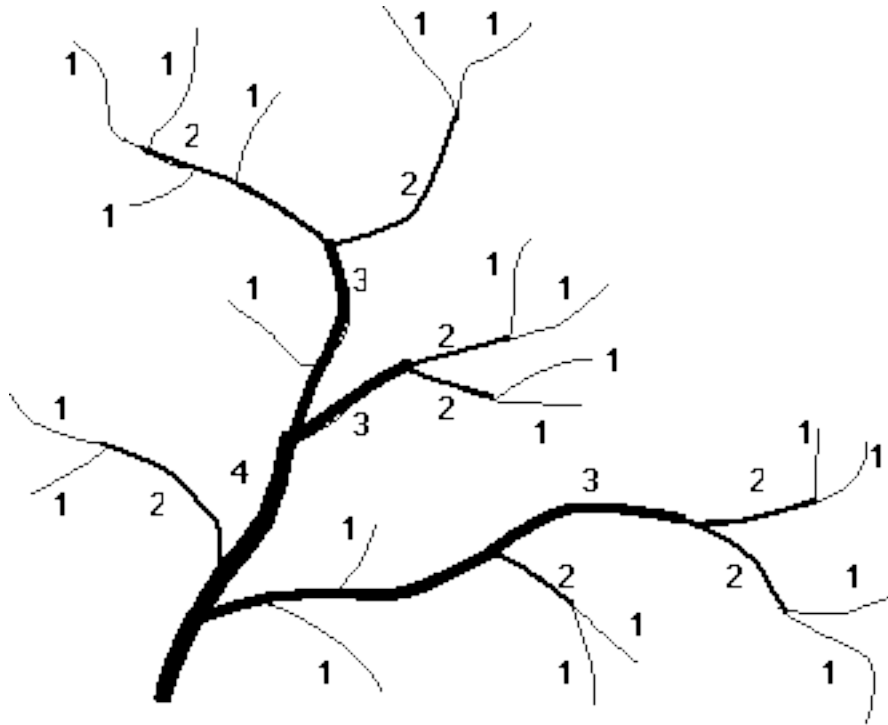


Figure 3.2. The Strahler Stream Ordering System. We label the tips of the vessels as first order. Then at every merger event, we choose the order of the daughter stream to be the maximum of the parents' orders. If they are of the same order, the daughter's order is increased by one. Figure from [13].

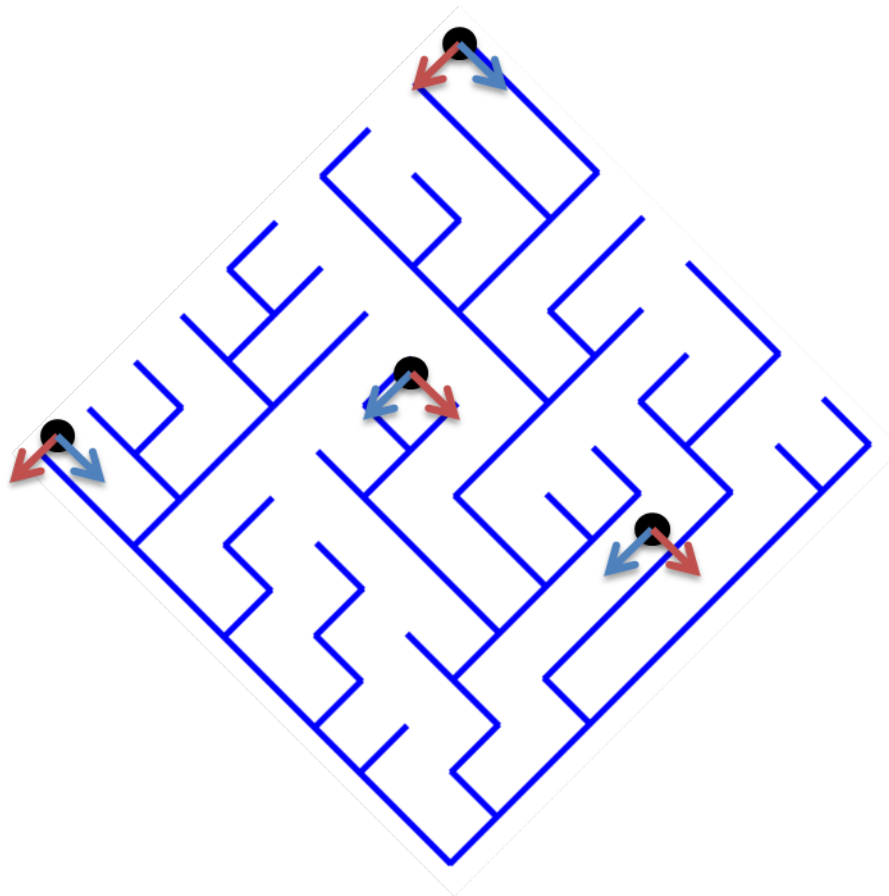


Figure 3.3. The Scheidegger Model on a square lattice. At each lattice point, consider a drop of rain falling down the page, moving either to the left or to the right in a random walk. (The blue arrow corresponds to the chosen direction, the red, the other.) One possible realization is shown with the “mouth” conditioned to be at the bottom of lattice.

3.3 The Problem of Quantifying Angiogenesis

If we imagine taking the Scheidegger model into three dimensions, we can begin to understand the difficulties inherent in describing angiogenesis mathematically. Ignoring the omnipresence of loops on all scales, a feature that the Scheidegger Model cannot explain, we will concentrate on the largest branches of the vascular tree. A first observation is that the ratio of the number of edges in the tree to the number of potential edges is smaller in three dimensions. For a square lattice in two dimensions, we have four points and four potential edges in each unit cell; the number of edges required to create a spanning tree, $E_{span} = V - 1$, is 3. Thus three of every four potential connections in two dimensions are part of the Scheidegger tree. This feature is intimately related to the self-duality property of Scheidegger trees: if we draw a new tree with edges perpendicular to the fourth unused edge in each unit cell, we will produce a second Scheidegger tree. In three dimensions, we have a cubic lattice, with 12 potential edges and eight vertices. E_{span} is only 7, and barely more than half of the potential connections are used. The convenient space-filling features of the Scheidegger tree have disappeared.

We can also consider the construction of a Scheidegger tree perpendicular to a mainstream vessel running the $+z$ direction, yielding a two-dimensional tree obeying a radial growth law, which we could imagine as a model for vascular organization around a large central vein. Depending on whether we choose the “downhill” direction to be decreasing outward (divergence) or inward (convergence), drastically different morphologies arise (Figure 3.4). To aid the eye, we have colored points that share a common outlet the same color and will refer to them as basins, in analogy to river networks. In the convergent case (Left Panel), we see few, large basins with the typical fan-like shape found in natural river basins. In the divergent case (Right Panel), there are many more basins, which share a dramatically different morphology, a leaf-like pattern that begins narrow, widens in the middle, and shrinks again near the mouth due to the spreading of the simulation manifold’s geodesics. The simulation area is filled with these basins of all sizes, in a manner reminiscent of tilings of the Poincaré disk [43].

The convergent and divergent cases resemble simple models of angiogenesis, wherein budding vessels either climb up or down a gradient of a morphogen. Alternatively, we may consider blood flow through an extant network of capillaries, choosing the shortest path possible through the capillary bed, either away from the main vessel (an artery) or towards it (a vein). Yet both of these classes of models are deeply problematic. In the morphogen case, we end up with a disconnected network (or one that is not space filling) if vessels were to branch from a main vein and move down a gradient. In

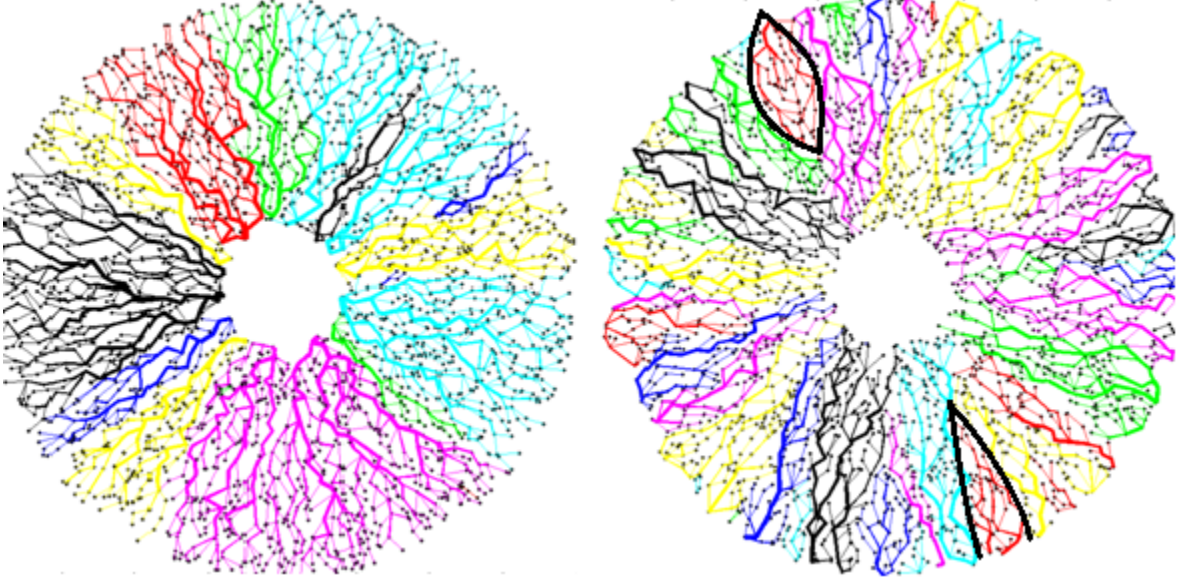


Figure 3.4. Radial Scheidegger networks for the convergent case (left) and divergent case (right). Collections of edges that share a common mouth on the boundary of the simulation manifold (the interior for the convergent case, the exterior for the divergent case) are colored the same and termed basins. Note the dramatically different basin morphology in the two cases: there are a few extremely large basins in the convergent case, and many basins on a multitude of scales in the divergent case, the characteristic shape of two of which is highlighted in black.

the convergent case, we would predict only very large vessels would touch the main vessel, a feature we definitely do not observe in real vascular networks, where small vessels continually impinge on large ones (see below). In the case of our potential mirroring a “flow” in the network, we would predict dramatically different network statistics for arteries and veins, something that has not been observed before [43].

3.4 Leaves and Loops

Moving from river networks to natural vasculature, we do not see the same treelike morphology. A brief glance at most leaf venation will reveal loops on all scales, as in Figure 3.5. The vascular system in mammals is replete with important loops, as we saw in §2.1, from the circle of Willis that provides a constant blood supply to the brain, to the anastomoses that allow the body to conserve heat in the summer and lose it in the winter.

What then is the morphology of an optimal transport network? Looped like a leaf or a branching tree, like in river networks? This question was studied by Bohn and Magnasco [7], who showed that for a network with links of conductance C and building cost C^γ , minimizing the power dissipated²,

² $P = CQ$, where P is the pressure and Q the flow velocity. This analogy to Ohm’s Law, along with Kirchoff’s

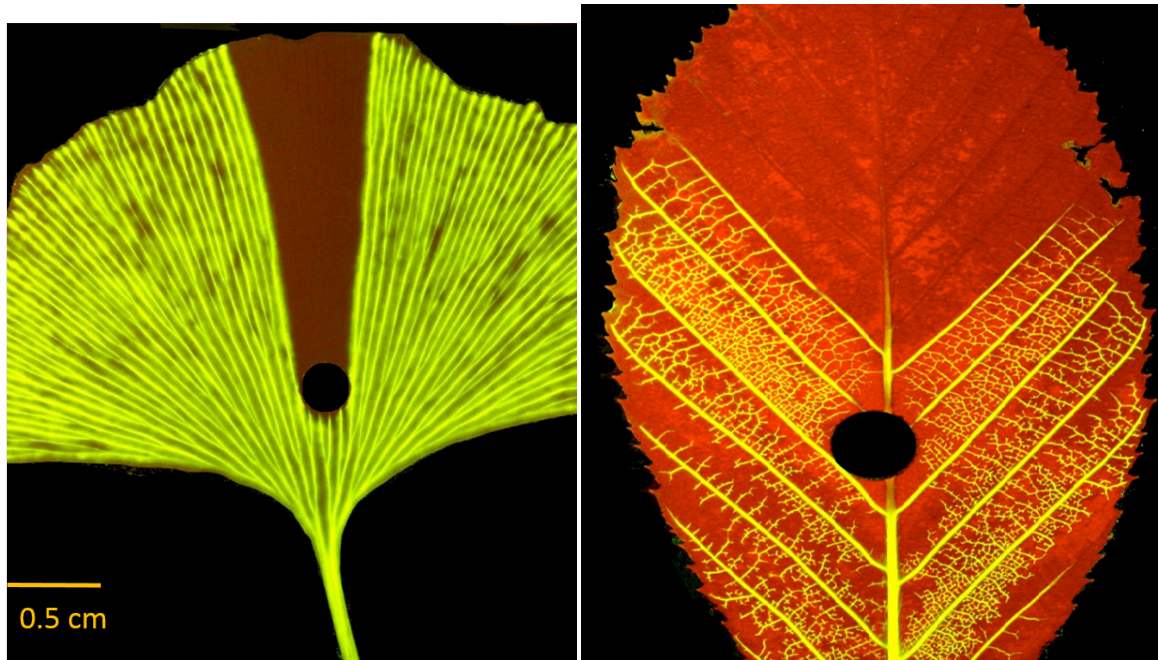


Figure 3.5. Leaves with fluorescein highlighting their venation. The leaf on the left is a Ginkgo, whose vasculature is purely treelike. The leaf on the right is a Lemon with a highly looped pattern of venation. Holes were cut into the main vein of both leaves to illustrate how the redundancy conveyed by loopy venation provides robustness in the case of damage: the veins of the Lemon leaf fill normally, while those of the Ginkgo are entirely empty behind the hole. Figures courtesy of Eleni Katifori and Marelo Magnasco

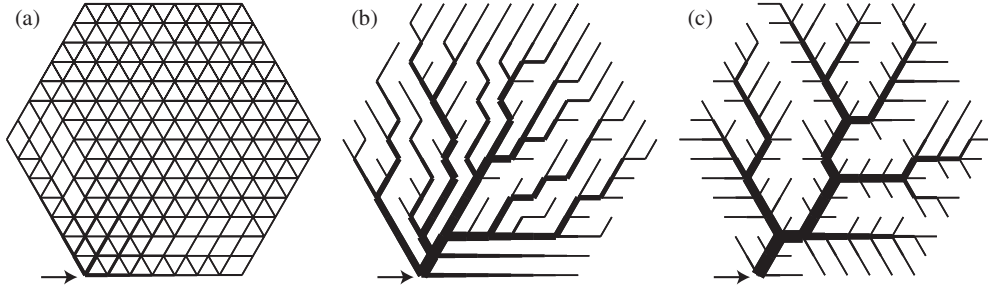


Figure 3.6. Optimal Distribution Networks provided a material constraint from the model of Bohn and Magnasco. The cost exponent, γ , is 2.0 at left, and 0.5 in the center and at right. The center panel illustrates a local optimum found via relaxation, the right panel, the global optimum, found by exploring the cost landscape. Figure from [7]

with a fixed cost will give a tree for $\gamma < 1$ and a uniform “sheet” of loops for $\gamma > 1$. Loops appear when there are no longer any returns to scale: when building a wider pipe is not worthwhile. These results are illustrated in Figure 3.6. For the case of Poiseuille Flow, the fluid velocity, $Q \sim r^4$, whereas the cost of a tube of length l scales as the radius, giving $\gamma = 1/4$, deep in the tree regime.

How then can we make sense of the loopy venation present in many leaves, especially as treelike vasculature is found in many ancient species such as Ginkgo (seen in the left-hand panel of Figure 3.5), whereas more modern plant lineages have looped vasculature suggesting the action of natural selection? Perhaps we are optimizing the wrong functional. Leaves, like many other transport networks, must be robust to varying load across the system. In the case of leaves, this is manifested as stomatal patchiness. Only certain portions of a leaf are photosynthesizing at a time. In the case of human vasculature, it is well known that blood demand varies across the vasculature in response to changing activities. Notably, this is the principle behind fMRI. Leaves especially also should be robust to damage, as the lemon leaf in the right-hand panel of Figure 3.5 is. They are continually attacked by herbivores, disease, and the elements. A similar, albeit somewhat weaker, case can be made that mammalian vasculature must be similarly robust. Optimizing under these two criteria dramatically changes the morphology of the optimal network [26].

In the case of the robustness to damage (“broken bonds”) model, this can be done by minimizing the power dissipated when a random link is broken. Since the dissipated power becomes infinite for a disconnected graph, the addition of some loops, at the least a single vein running along the perimeter of the leaf, becomes necessary. The optimal network shows more loops than strictly necessary. See the left-hand side of Figure 3.7. In the case of fluctuating load, Katifori and Magnasco minimized the power dissipated for a single source at the step and a sink located randomly in the network and continuity and conservation laws allow for easy solution of the flows through the network

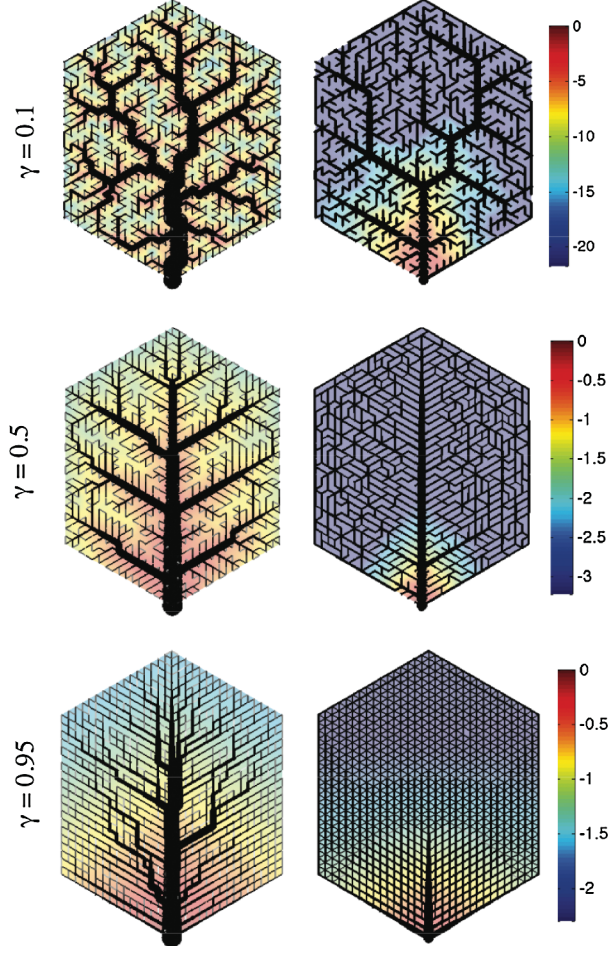


Figure 3.7. Optimal Distribution Networks in the cases of robustness to damage (“broken bonds”), left side, and fluctuating load, right side. Loops are present for $\gamma < 1$ in both cases, with increasing hierarchy as γ decreases. The pressure drop is encoded in the color scale. Note how the pressure drop varies as the distance to the stem for the fluctuating load model but as the distance to the nearest main vein for the “broken bonds” model. Figure from [26].

averaged over all instantiations. The resulting networks are also extremely loopy and are displayed on the right hand side of Figure 3.7. While both networks are loopy, they differ in their properties. For the broken bond model, the pressure drop is controlled by the distance to the nearest large vein, whereas for the moving sink model, it is controlled by the distance to the stem. The former is fractal for $\gamma < 1$, whereas in the latter, fractality only holds for $\gamma < 0.5$ [26]. The venation patterns of leaves look considerably closer to the “broken bonds” model than the fluctuating load one.

3.5 Vasculature in Three Dimensions

Vascular networks in three dimensions have generally received scant attention, with the majority of studies rather blindly adopting treelike models, looking for fractal properties [2, 63], or attempting to understand metabolic scaling laws (see below). This situation is odd given the knowledge of anastomosis dating by Harvey, Malpighi, and Ruysch, as well as Poiseuille, whose work on fluid flow in blood vessels is replete with drawings of looped vasculature [46]. These efforts have been successful in treelike structures, mostly the bronchioles of the lung [31], which can be shown to be close to the optimum in terms of the bifurcation and length ratios³. There is one prominent exception in the work of Cecil Murray in the 1920s, who used the principles of fluid dynamics to find the optimal flow conditions in vascular networks without assuming treelike morphology. This relation, known as Murray's Law, has been validated by a host of experimental studies in the decades since its publication and constitutes the strongest piece of our theoretical grounding for vascular networks in three dimensions [55].

If we consider a vessel with Poiseuille flow, $f \sim r^4 \Delta p$, with f the flow rate, Δp the pressure drop, and r the radius, the power dissipated by flow, P_f , will scale as:

$$P_f = f \Delta p = a f^2 r^{-4} \quad (3.4)$$

Here a is an arbitrary constant. The metabolic power expended, P_m , will scale as the blood volume, giving:

$$P = P_f + P_m = a f^2 r^{-4} + b r^2 \quad (3.5)$$

with b an arbitrary constant with units of length. We may find the vessel radius at which minimal power is dissipated by differentiating and equating to zero:

$$\frac{dP}{dr} = 0 = -4a f^2 r^{-5} + 2b r \quad (3.6)$$

$$4a f^2 = 2b r^6 \quad (3.7)$$

$$r^3 \sim f \quad (3.8)$$

To ensure maximal efficiency, blood should flow at a rate proportional to the cube of the radius. At a junction where vessel 1 bifurcates into vessels 2 and 3, this implies what has come to be known as

³The difference between the optimal fractal and the lung bronchioles seems to convey robustness to blockage

Murray’s Law:

$$r_1^3 = r_2^3 + r_3^3 \quad (3.9)$$

This result has been verified in a range of natural vascular systems and imposes a strong architectural constraint [35, 36].

It is also worth mentioning the flurry of attention paid to theoretical arguments about vascular structure in the attempt to provide an explanation for Kleiber’s Law. This “law” is merely a codification of the observation that over 27 orders of magnitude in organism size, from bacteria to whales, metabolic rate seemingly scales as body mass to the $3/4$ power. This observation has long been considered theoretically problematic, as a simple geometric argument would suggest an exponent of $2/3$, assuming heat loss proportional to surface area and energy production proportional to volume. West, Enquist, and Brown optimized a general hierarchical model, parametrized by length, radius, and bifurcation ratios, and found an optimum for a fractal, treelike network. Assuming blood volume scales as the metabolic rate, one may calculate from the necessary depth of the network (related to organism size) that there should be and show $3/4$ power scaling of metabolic rate [63].

This model is problematic for numerous reasons. Dodds and Rothman showed that the mathematics used in the optimization procedure do not in general produce the solution WEB claimed. It even violates Murray’s Law⁴. The assumption of fractality, used in many such models, while seductive, is not well grounded in the first place (see §2.1) and does not even hold over all scales in simpler systems (e.g. river networks). Further models by Banavar and by West et al. stepped away from vascular structure, though their mathematics have been criticized as well. Ultimately, though these models have taught us little about vasculature and about metabolic scaling (it is not even clear that the proper exponent is $3/4$ when the data are properly examined), they have served to pique interest in many in the problem of vascular morphology and of allometric scaling in general [19].

Beyond the mathematical flaws of the West Enquist Brown model, there is a deeper methodological flaw. It has been well known for decades that vascular networks are highly anastomosed, creating loops on all scales. Gray’s anatomy is full of beautiful drawings of these connections and suggests, as we saw in §2.1, that on small scales there is more a “dense network” of arteries than a tree. To suggest that this type of structure is analyzable in terms of rigid hierarchies and bifurcations seems a bridge too far. The scale of the “loopiness” in the network surpasses occasional redundant connections. A hierarchy fundamentally based on loops is better suited for this purpose [61].

⁴If we state that the number of vessels of order $i + 1$ is b times the number of vessels of order i and the vessels are smaller in length and radius by a factor a , then volume conservation implies $r_i^2 l = b r_{i+1}^2 a^2 l$ or $a^2 b = 1$ to match Murray’s Law, a condition that is not enforced by WEB

3.6 Analyzing Hierarchies

The paucity of theoretical models for vasculature is surely related to both the lack of good morphological data (Chapter 2) and the lack of theoretical tools to analyze what data we do possess. Current toy models do not include loops, despite their presence across all scales in natural vascular networks. Our basic methods of analysis are also at a loss: Strahler stream ordering cannot deal with loops as it assumes only mergers between lower order vessels while moving downstream, not bifurcations. A closer look at the lemon leaf in Figure 3.5 above reveals an apparent hierarchy of the venous loops within the leaf: smaller loops nested in larger loops. The problem is to quantify it.

The trick is to hearken back to the intimate connection between geometry and topology we observe in vascular networks. We need a rule that classifies loops, which are a purely topological feature. Our only choices of parameters to do this are geometric in nature, for instance the width and length of the segments that make up the loop. Katifori’s algorithm for loop hierarchy identification makes use of the vessel radius. At each step, the narrowest vessel along the edge of a loop is cut, eliminating that loop and merging it with a neighboring one. If we number each loop and draw a tree corresponding to the order of their mergers, we establish a representation of the hierarchy of the loops within the leaf. This process is illustrated in Figure 3.8. When applied to real leaf networks as well as random network models, this algorithm results in statistically distinct trees. Using standard methods of quantifying tree architecture, such as the bifurcation ratio and the tree asymmetry, these networks may be distinguished [25].

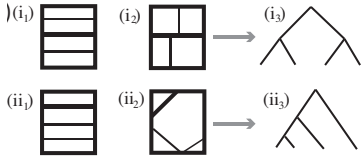


Figure 3.8. Illustration of the Katifori Algorithm for creating a hierarchy of loops in a planar graph. Both of the graphs in the top and bottom rows respectively yield the same tree shown on the right. Briefly, edges are removed in order of their width, forcing the merger of loops, resulting in a treelike structure for loops based on the weights of their edges. Figure from [25].

Critically, this procedure cannot be easily extended to three dimensions. It only works for planar networks. Removing an edge in a nonplanar network can cause the formation of a new nonplanar loop (or facet) to form, which is deeply problematic. For example, consider a wireframe cubic lattice. If we remove any link, we merge four loops that formerly defined the faces of four cubes with a common edge. The resulting loop outlines a + shape extruded into the third dimension. This is clearly structure with different topology than a loop. What is needed is to find a proper

two-dimensional embedding for the graph and then find a way of running the Katifori algorithm. We will return to this question later, when considering the loops present in the vasculature of entire organs.

Chapter 4

How to Image the Vasculature of Entire Organs: Serial Blockface Microscopy

For our initial experimental foray, we chose the rat liver. Rats present an ideal system as they are plentiful in biomedical research laboratories, allowing us to use the rats discarded by other laboratories and those used for training by the animal facility at Rockefeller. Physiologically, they are relatively close to humans: they eat a similar diet, as they have evolved for centuries alongside human settlements. Rodents are the closest order among the mammals to the primates; the two form superorder Euarchotoglires along with the lagomorphs. We could thus expect organ morphology and structure to be relatively conserved. In the case of the liver, this is true across all mammals [61].

Rat organs are also a good size for slicing and imaging (see below). A lobe of rat liver, or an entire heart or kidney, fits easily within a $22 \times 30 \times 20$ cm rectangular embedding mold and onto the surface of a 40 mm Peltier device. More importantly, the scale of the largest vessels will be around an order of magnitude less than the size of the organ, in our case in the hundreds of microns. The size of the capillaries is around $5 \mu\text{m}$ and the smallest hierarchical vessels perhaps twice as large. In a rat organ, we had vessels whose size ranged over nearly three orders of magnitude to study (and five orders of magnitude in cross-sectional area). In a mouse, we would have lost between a half and a full order of magnitude (a lobe of rat liver is the same size as an entire mouse liver of 5-6 lobes), greatly weakening our ability to probe vascular structures at all scales. Examining a mouse liver

under a dissecting microscope revealed a further complication: dramatically different morphology in the largest hepatic vessels. They appear as large fissures in the tissue rather than rounded, lined vessels.

The liver is a useful organ with which to begin. Structurally it is simple (for details see §4.1) with very little internal geometry. The main functional/structural unit, the lobule, is not regularly tiled, or packed into the liver, leading to a lack of a preferred axis and symmetries. This situation may be contrasted with the kidney, where the nephrons are highly stereotyped in structure and pack regularly to fill out the interior of the kidney, itself aligned along a central axis. A lack of preferred geometry would prove useful when cutting initially: we would not have to align our sample to hit certain features head on. This structural simplicity also manifests itself in the existence of only two major cell types: the hepatocytes and the Kupffer cells. These latter cells line the smallest capillaries and are dramatically smaller than the hepatocytes: $\sim 1\text{ }\mu\text{m}$ versus $\sim 10\text{ }\mu\text{m}$. With a paucity of cell types, our signal would be more regular and easy to interpret. The remarkable ability of the liver to regenerate after removal of up to 70% of its mass suggests an attractive structural simplicity and uniformity as well as the ability to probe vascular development [9,61].

The liver is additionally heavily vascularized. It plays host to four vascular networks in two trees. The portal triad consists of the portal vein and hepatic artery (the two sources of oxygenated blood) and the largest bile ducts, whose flow is in the opposite direction of the rest of the triad. The second tree is that of the hepatic vein, which drains the liver. As the liver “cleans” the blood, there is a large volume fraction of capillaries, around 15%, leading individual slices of liver to look like wormwood or an extremely complex swiss cheese as in Figure 4.1 [9]. The liver additionally strongly autofluoresces, notably in the blue-violet, unlike other organs. An example spectrum at 400 nm is shown in Figure 4.2. Initially we had hoped to image solely using this autofluorescence signal. While this turned out to be impractical, see §4.3, this signal was extremely useful during the image analysis stage.

The liver is also afflicted by a range of vascular diseases, from the various forms of hepatitis to cirrhosis, originating in different toxins. Nearly all of these diseases may be induced in rats, as well as cancers of the liver, which, as mentioned previously, may significantly rearrange vasculature. The ability to easily study diseased organs added to the advantages of rat liver.

While we set out to characterize the entire vasculature of whole organs, we were not able to image the capillaries in general due to the limitations of our imaging system (see §4.3). We concentrated our efforts on studying what we term the hierarchical vasculature: the arteries and veins above the scale of the capillaries. Our effective resolution was $\sim 10\text{ }\mu\text{m}$, allowing us to capture the arterial and

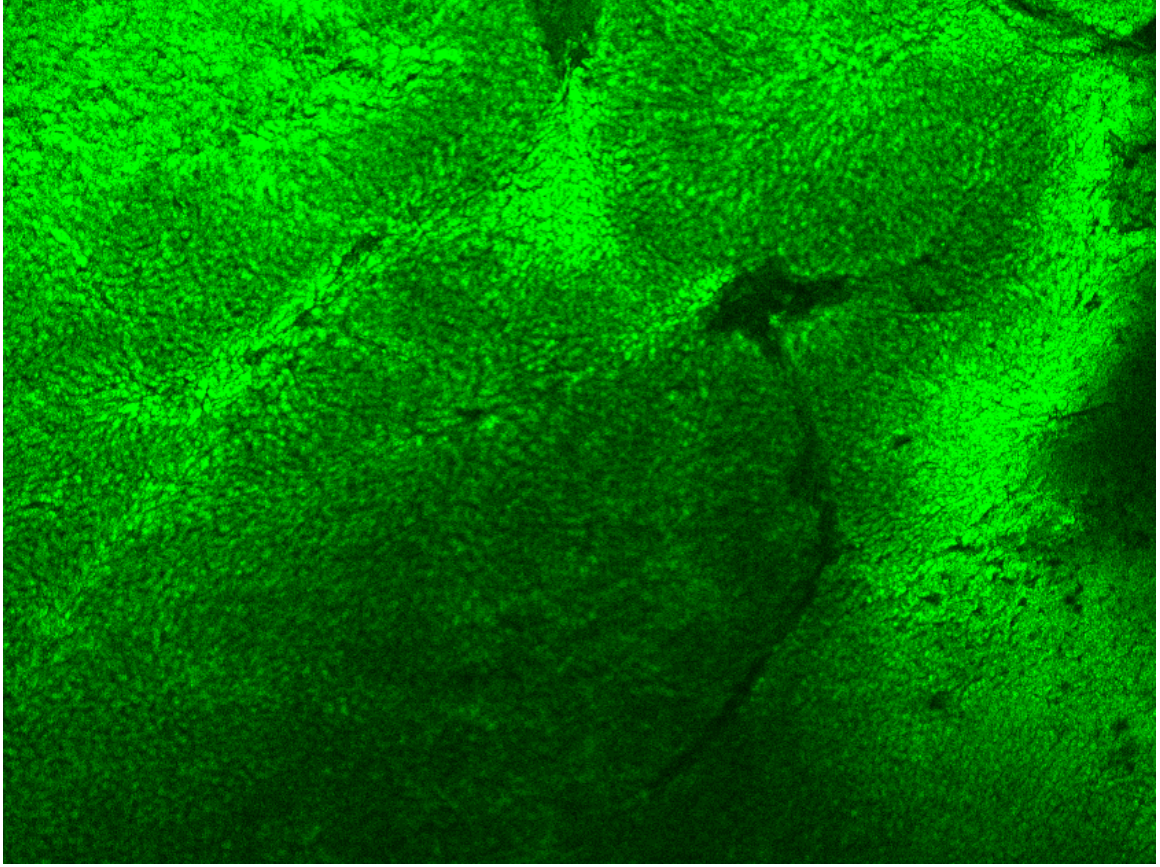


Figure 4.1. Two-photon image of a slice of rat liver. Note the large volume fraction of vascular regions, the dark spaces between the hepatocytes, which fluoresce green. A well-ordered lobule (see §4.1) can be seen in the center, ringed radially polarized cells separated by sinusoids. On the right side, a large “cavity” can be seen, corresponding to two large branches of the portal triad. One large vessel is perpendicular to the plane, and another merging with it runs parallel to the plane. Photo by the author.

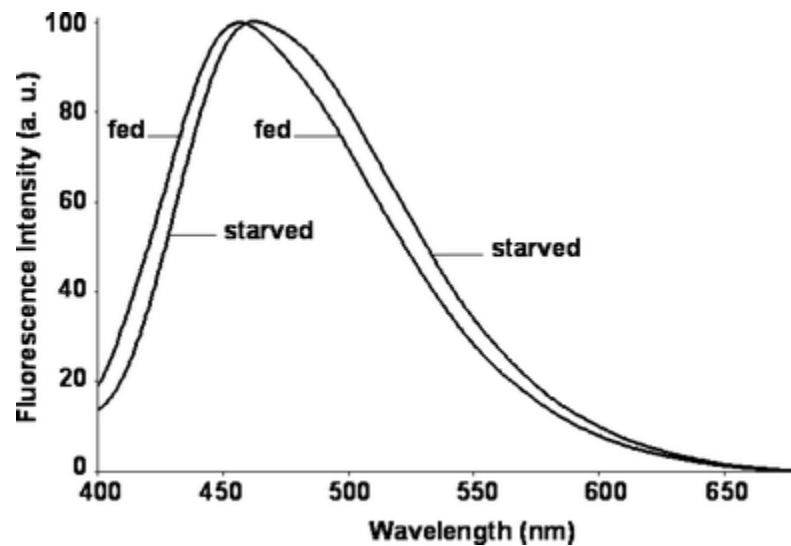


Figure 4.2. Autofluorescence Spectrum of hepatic tissue at 400 nm. Note the wideband signal and the strength of response in the blue. Figure from [15].

venous trees. This limitation was unfortunate; on the other hand, as seen in §2.1, there appears to be a large difference between the anatomy and network morphology of capillaries and of arteries and veins. Our inability to generate artificial versions of the latter suggests strongly different statistics and network structures, beyond a simple caricature of a honeycomb lattice versus a binary tree, between the two. Characterizing the hierarchical vessels then is an important first step and, on some level, fills the largest gap in our understanding of vascular network morphology. Lastly, if we had been able to capture the capillaries, even with as little as $2\times$ better resolution, we would have been encumbered by a truly enormous dataset, in the hundreds of gigabytes, unable to be held in memory by any one machine at any time.

Our apparatus was a simple and cheap implementation of conventional blockface microscopy and will be justified and detailed below. Briefly, we perfused rats with 200 nm fluorescent beads. We then fixed, embedded, and froze samples of rat liver to the head of a microtome. A precision controlled camera equipped with a makro lens performed imaging at 5 μm resolution. The system was robotized allowing us to cut hundreds of 5 μm slices. These slices could then be segmented, aligned, and reconstructed in three dimensions, giving a map of the vasculature of the liver, down to the ~ 10 μm level.

4.1 Hepatic Morphology

The liver is composed of four lobes: the large right and left lobes, which we use in our experiments, and the smaller caudate and quadrate lobes. This structure is generally conserved across vertebrates. Functionally, these lobes are essentially equivalent. Within each lobe, there is a branch of the portal triad (portal vein, hepatic artery, and bile ducts) and one of the hepatic vein. The liver is the site of the breakdown of toxins and many of the body's waste products, among them hemoglobin. The presence of large numbers of aromatics and ring structures, such as in bilirubin, cause the dramatic autofluorescence present in liver tissue. The liver is also the site of the production (and breakdown) of glycogen, many amino acids, red blood cells, and several other compounds. It may also act as a storehouse for vitamins and other nutrients [9].

The liver is commonly divided into subunits known as lobules. A hepatic lobule consists of a hexagonal prism of tissue, commonly only shown in two dimensions, surrounding a central hepatic vein. On three vertices of the hexagon lie branches of the portal triad. An example maybe seen in Figure 4.3. With the exception of a few species, such as pig, where the lobules are defined by connective tissue, this tiling of the vascular networks admits another interpretation, with a section of

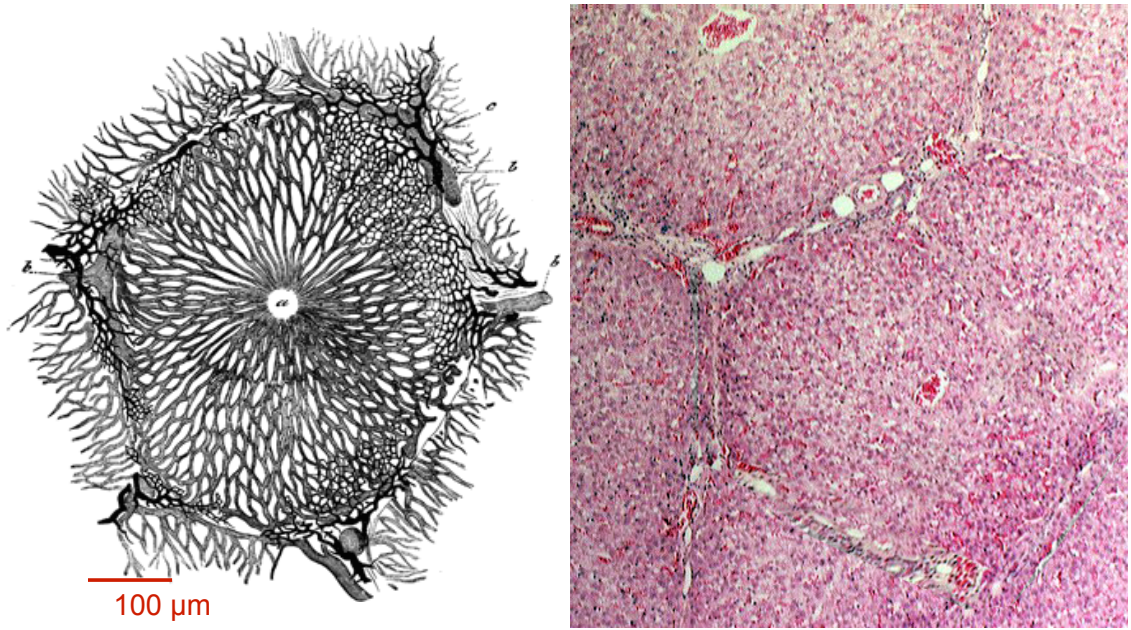


Figure 4.3. Liver Lobules in Theory, left panel, and Practice, right panel. The supposedly stereotyped structure of the liver lobule with a central element of the hepatic vein surrounded by three branches of the portal triad on alternating vertices of a hexagon. The area between these large vessels is filled with sinusoids. The extension in the third dimension is rarely extrapolated very far; a typical size would be 100 – 500 μm . On the right-hand side is an image of a cut through a liver lobule in pig, where the boundaries of the lobule are defined by connective tissue. Images from [61] (left) and [11] (right).

portal triad at its center, known as a portal lobule. Hereafter we shall refer to the hepatic lobule as solely a lobule. The packing of hexagonal prisms into a curved three-dimensional lobe is problematic. All of the central hepatic veins and the portal triad components must merge and exit the lobe as one vessel. Similarly, the vessels must merge before the stacks of lobules reach the outside of the liver, lest the portal triad empty into the abdominal cavity. This packing, then, must be heavily irregular, replete with topological defects, and the hexagonal prismatic structure must not persist too far in the third dimension. Lobules must exist at different sizes and different relative angles. We do not necessarily expect to see many hints of lobular structure looking at the vasculature of the entire liver [61].

No matter the definition, the lobules are filled with generally radial sinusoids (unlined capillaries) and the hepatocytes proper. These cells are generally polyhedral, with faces $\sim 10 \mu\text{m}$ on a side, and apical projections that form the bile canaliculi. These latter vessels are only around $1 \mu\text{m}$ in size; along with the similarly sized Kupffer cells that are located along the sinusoids, they are invisible to our imaging. It is commonly thought that the hepatocytes form radial cords from the central hepatic vein to the edges of the lobule. Other opinions suggest that the hepatocytes in an entire

lobe of liver form a single, corrugated sheet, holes in which are formed by anastomoses between the sinusoids. While intriguing, these structural details are beyond our current optical capabilities and present an interesting subject for future study [61].

4.2 Slicing

The opacity of hepatic tissue and its copious autofluorescence rule out the possibility of optical sectioning. There exist methods of optically clearing tissue; however, these procedures have not proved successful when applied to liver. One school of thought uses urea (in a solution known as *scale*) to turn tissue transparent at the cost of introducing volumetric distortions [21]. When we tried this method on mouse liver, approximately three orders of magnitude smaller in volume, we found that even extended soaking did not turn the tissue fully transparent. While the clarity method shows some promise, it is not clear to us how well it will function in the liver, whose tissue is filled with all manner of optically dense and fluorescent compounds.

We were thus led to serial sectioning. A first attempt to simply cut slices on a cryostat, mount them on slides, and then image them proved unsuitable for the task. The fundamental tradeoff in serial sectioning is between the structural integrity of the slices, which increases with thickness, and the z resolution, which requires as thin slices as possible. Technicians experienced in this type of work are able to cut slices thicker than about 12 μm without issue. We require approximately twice this resolution to be able to capture all the vessels above the scale of the capillaries. Slices of 8 – 10 μm can frequently be cut without error. However, occasional errors would be devastating for our ability to connect slices in three dimensions¹ These errors can include small tears in the tissue, blade-induced shearing, and warping of slices with large vascular features and hence large holes. Even at an error rate of 1%, we would still have of order ten unusable slices per centimeter lobe of liver. This is far too high an error rate.

Instead of keeping the slices, one can discard them and instead image what remains after a slice is taken. This procedure is known as blockface microscopy; it originates with the relatively recent work of Winfred Denk [16]. Provided one’s optics do not take in too much out of focus light, these images will not be appreciably different in resolution and quality than those of slices, but without the risks of warping and tearing. The large block of tissue is essentially immune from shear and tearing.

¹These figures come from a month’s effort in collaboration with the Nottebohm lab at Rockefeller. A technician cut slices of zebrafish liver from birds previously sacrificed and we imaged and segmented the resulting images on a standard light microscope.

The major issue with blockface microscopy is that the optics must be brought into the sectioning environment. Normally, tissue is cut on a cryostat, a microtome mounted inside a glass-walled freezer, operating around $-20\text{ }^{\circ}\text{C}$ to ensure solidity and density matching. The operator controls the machine from the outside, examining his work through a glass window. Slices may be removed via a small opening in this window. If we wish to simultaneously slice and image, either the optics must peer through this window or be placed at the opening. The former is unacceptable as the windows are not made of optical glass and are not perpendicular to the sample. Images taken through the glass are full of artifacts from the frequently scratched and dirty glass as well as from imaging at an angle through a piece (or worse, pieces) of glass. If instead of imaging through glass, we image through the window, we expose our optics to the cold of the cryostat. Thermal gradients of this magnitude, $40\text{ }^{\circ}\text{C}$ over approximately a centimeter or so, are unhealthy for precision optics. Similarly, the cold air of the cryostat will cause large amounts of condensation on the lenses, making imaging more difficult and potentially causing the dissolution of the various anti-reflective coatings on the lenses.

To solve this problem, we built our own cryostat out of a commercial microtome, a Leica RM 2250, and a Peltier-based cooling system. We reasoned that our samples were small enough that if a cold enough temperature were applied to them on one side, they could be kept within a temperature range appropriate for cutting. Low temperatures can be achieved over small areas through the use of a Peltier device, which creates a thermal gradient in response to an electric current. This effect is the precise analog of the better-known thermoelectric effect, wherein an applied thermal gradient causes the formation of an electric potential in a material; the two are connected through an Onsager Reciprocity Relation [42]. The problem is that a Peltier device consists of an cold side *and* a hot side. These devices are also only 10-30% efficient, producing a significant quantity of waste heat. A Peltier device mounted on a thermal conductor can remain cold for a short period of time, but holding a consistent low temperature for hours requires efficient cooling of the hot side.

We used 110 W Peltier devices, which produced too much heat, around 80-100 W, for air cooling to prove sufficient. Instead, a water cooling system was necessary. We adopted a GPU water cooling system made by Swiftech, the H2O-X20 series. The Peltier was mounted on a copper block, with hundreds of microchannels cut into its back, the waterblock of the Swiftech kit. Water flowed through these channels, then through a series of plastic tubes to a radiator, itself cooled with two RDMS fans. This system proved more than adequate to keep the Peltier at $-18\text{ }^{\circ}\text{C}$ for weeks at a time. The copper block was mounted to the head of the microtome with a set of screws and adapters of our own design. The Peltier was attached using thermal grease, which, provided it did not reach

high temperature, formed an extremely strong bond, resistant to being pulled directly off. Since this connection could be sheared, we designed a plexiglass “cup” to fit around the head of the microtome and the Peltier to lock it into place. This piece could be easily cut out on a milling machine or a laser cutter and assembled by chemical welding.

Modified in this manner, we were able to keep samples of up to 1cm thick well below the freezing point. The main cause of sample melting was not the ambient temperature, which we attempted to keep below 20 °C, but rather the humidity in the room. Any water in the air would condense and eventually freeze onto the sample, releasing a significant amount of latent heat. In the New York City spring and summer, we had significant problems with humidity, oftentimes limiting the length of time we could keep a sample frozen. In the winter, the air was dry enough to allow us to leave samples up for a month or more at a time without any problems. To combat the effects of humidity, we built a chamber around the sample from ThorLabs metal poles and plexiglass sheets. A hole was left in the front for imaging. Nitrogen, either gaseous or liquid, could be leaked into this chamber from the back to expel humid air and prolong the sample lifetime. Liquid nitrogen could also be sprayed directly onto the sample to cool it in case it was melted during the attachment process.

The use of blockface microscopy allowed us to cut thinner sections; we were limited only by the precision of the microtome. Following the advice of a microtome engineer, we limited our slices to 5 μm , a length that could be improved upon with a newer microtome. Temporary blades, profile C, were mounted at 5°. Initially, we cut with a perfectly vertical blade. However, when cutting thin slices, there was a tendency for melted embedding medium and tissue to accumulate on the back side of the blade. This could be corrected by tilting the blade slightly. Every 100 slices or so, the blade was cleaned with acetone to remove any accumulated tissue. If left unchecked, occasional pieces of tissue or embedding medium would stick to the blade, causing streaky artifacts on the blockface itself and impairing our images. These artifacts could be removed in post processing, but would limit our resolution if they were not cleaned.

4.3 Imaging

As we saw in Section 2.2 above, the combination of a large area to be imaged and a demand for near micron resolution make designing an imaging apparatus nontrivial. Our solution was to use makrophotography. A akro lens is one that allows a camera to take images of the same size as its sensor, 35 \times 24 mm, for most commercial cameras. If the camera has a 21 megapixel (5616 \times 3744) sensor, then our effective resolution is 35/5616 mm \approx 6 μm . We used a Canon Mark II 5D camera

with a Canon MPe 5x Makro lens.

While the Makro lens was able to magnify up to 5 fold in theory, any resolution beyond 2x was useless. This is due to the peculiar scaling of the Numerical Aperture of Makro lenses with magnification. Typically in photography, one measures light-gathering ability and resolution by the f-number, or the ratio of the focal length to the aperture diameter. As the objects we photograph are not very far from the lens, we need a more accurate calculation. We may calculate the working f-number as follows [8]:

$$N_w = \frac{1}{2N_a} \approx (1 + |m|)N \quad (4.1)$$

where N is the uncorrected f-number, m is the magnification, and N_a the numerical aperture. The size of the diffraction limited spot is given as [8]:

$$d = \lambda / (2 * N_a) = \lambda(1 + |m|)N \quad (4.2)$$

Theoretically, we can achieve maximum resolution with a small f-number. If we let N get too small, however, we will let too much out of plane (and thus out of focus) light into the camera. As a compromise, we settled on a value of $N = 4$, or three clicks above the minimum. The primary wavelength we image at is set by our fluorophore and filters (see below) and is approximately 550 nm. This gives a diffraction limited spot of:

$$d = 550 * 4 * (1 + |m|) \text{ nm} = 2.2(1 + |m|) \text{ } \mu\text{m} \quad (4.3)$$

This calculation rules out the magnification on the lens as useful above approximately 2x. Any effective resolution gain is washed out by the large diffraction-limited spot. We set the magnification of the Makro lens to give us 5 μm pixels, ensuring nearly equal resolution in all directions. This was accomplished by adjusting the magnification until a feature of set size, the length the embedding mold (2 cm) subtended the short side of the camera sensor, or 3744 pixels, giving a resolution of $\approx 5.3 \text{ } \mu\text{m}$ in x and y .

The camera was mounted on a set of precision XYZ axes. We attached three ThorLabs Long Travel Stages, each capable of moving up to 300 mm in 4 μm increments, to one another. These axes were controlled by a GUI on the computer or alternatively could be programmed in C. The X and Y axes were used to control the area of the sample the camera is imaging. The Z axis focused the camera by adjusting its distance to the sample. We focused the camera under white light with the emission filter for fluorescence (see below) attached. By opening the live view mode in the Canon

camera software with maximum exposure (1/40 s), we were able to see the degree of focus in real time. By panning back and forth, the proper focus was easily found. The entire system was mounted on a vibration insulated optical table, ensuring stable imaging.

4.4 Fluorescence and the Search for Signal

It is tempting to believe that there is no need for enhanced contrast to detect vasculature in pieces of tissue. Blood vessels are, after all, holes in a piece of tissue² and in the limit of thin slices, they can be easily detected: a slice of tissue of single-micron thickness will look like a piece of swiss cheese under a microscope, full of vascular “holes.” When imaging the blockface, the vascular regions would appear darker, as less light would reach into them, especially if the illumination were tangential. Similarly, any activated autofluorescence signal would be weaker in the vessels, providing further contrast. While practicable in theory, this form of illumination was not sufficient, as can be seen in Figure 4.4.

While in portions of the sample, such as the lower left, there is good contrast, especially for the largest vascular features (the honeycomb array of dark dots), it is inconsistent across the sample. There are an abundance of freezing artifacts in other regions of the sample, from parallel lines of ice crystals that obscure the vasculature behind them to deposits of embedding medium left by the blade that appear as irregular white lines across the tissue. Clearly a stronger signal was needed. However, with the passage from white light to fluorescence, the exposure time needed for an image increased dramatically, from $\frac{1}{40}$ s to around 1 s. The search for a strong, high-contrast, and uniform signal was not simple.

We turned next to autofluorescence, making use of the liver’s propensity to glow even when illuminated deep in the violet. Imaging with a 405 nm LED and a 425 nm filter, we could be assured of only getting an autofluorescence signal (and one that could be easily separated from the excitation source at that). An example image is seen in Figure 4.5. The biggest problem with the autofluorescence images is the lack of contrast. While larger blood vessels can be detected as dark spots, the strength of the signal varies substantially across the sample. As the signal-to-noise ratio is not great in the brightest regions, these contrast gradients are deeply problematic. While the exposure of images can be changed, it becomes impractical at some point to take four or ten-second exposure images for hundreds of slices of liver, not to mention that the longer the integration time, the higher the risk of blurring due to slight motion of the microtome head.

²Lined, of course

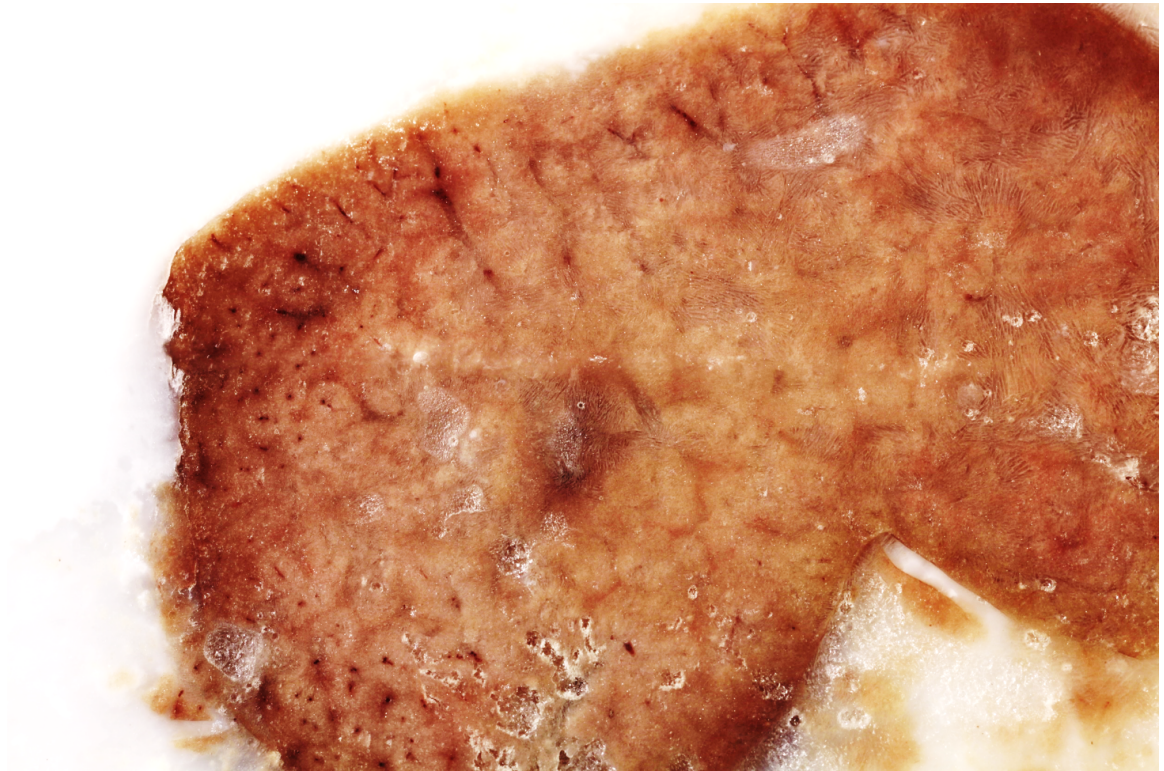


Figure 4.4. Image of rat liver taken only with tangential white light. Note the good contrast in the lower-left-hand region of the tissue, allowing easy separation of larger vascular features (the dark pixels) and smaller, in plane vessels, from the surrounding tissue. In the right-hand side of the figure, note the artifacts due to freezing (the parallel ice crystals) and the obscuring of tissue by cutting artifacts, as well as poorer contrast.

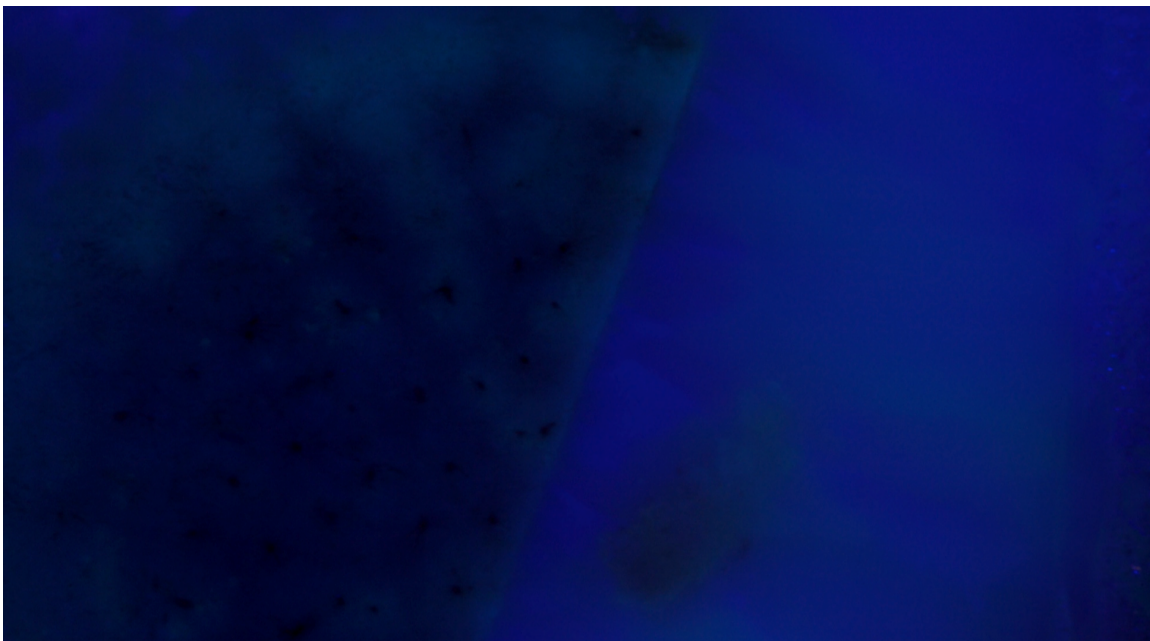


Figure 4.5. Autofluorescence Image of rat liver. Note that large vascular features can be easily distinguished, but that the overall signal to noise ratio is quite poor and the strength of the signal varies across the tissue. Compare the extractable features with those in the white light image, Figure 4.4

Since the tissue itself did not provide sufficient contrast, we turned to perfusion. Rather than making the tissue glow, we would fill the vessels with a fluorophore and make them glow. Our lack of experience in highly technical perfusions led to us ruling out filling the vessels with a resin or plastic compound combined, as is done in corrosion casting³. It is far simpler to perfuse with a pure fluorophore or a suspension of fluorescent beads. We began by perfusing with molecular fluorescein, which provides an extremely strong signal. Unfortunately, it is a small molecule and was readily absorbed by the tissue and would leak out of the sample during fixation, leaving a mostly dark sample with haloes around the vessels. One rapidly fixed and frozen sample did yield images of capillaries in a small region, when cut. These may be seen in Figure 4.6.

One way to correct for the “running” of the fluorescein is to weight it with a significantly heavier protein, such as albumin, or a sugar, such as dextran. We experimented with fluorescein conjugated to albumins and dextrans (FITC) with molecular weights up to 70000. While the heavier FITCs stayed within the sample, we were not able to prevent them from being uptaken by the tissue. Instead of glowing vessels surrounded by dark tissue, we saw mostly dark vessels ringed by glowing haloes of FITC, much like images of the Solar corona during an eclipse. This signal slowly away

³We believe this would be the correct way to proceed in the future, provided access to someone with the proper technical expertise.

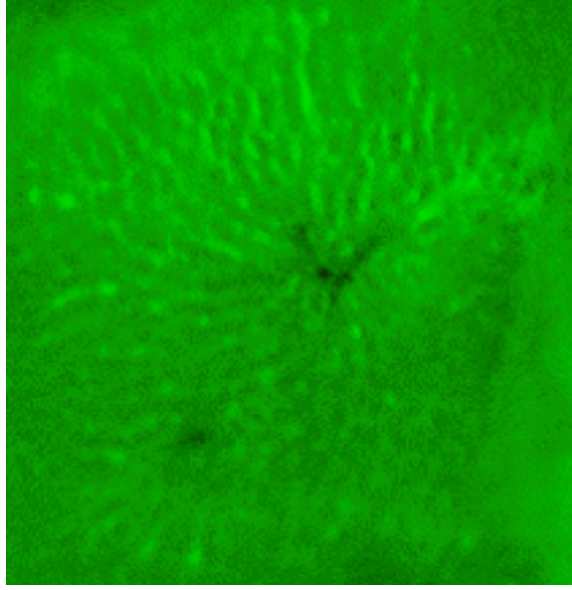


Figure 4.6. Capillaries in a lobule of liver, seen at $5\times$ magnification on the Makro lens. Perfusion with fluorescein, followed by rapid freezing, led to a rare image of capillaries through our makrophotographic optics. As we are imaging features at the scale of the diffraction limited spot, the image is necessarily rough. Note the neat lobular structure around the merger of two hierarchical vessels.

from the vessel into the tissue. Provided a good model of the diffusion of the FITC into the tissue, we believe these images could be used successfully to determine the locations of the blood vessels. Absent one, however, it would be hopeless to segment either based on overall brightness, which would pull out both tissue and blood vessels, or edge detection, which would find both the vessels and the edges of their “haloes.” Two options that we did not try are carboxyfluorescein, a form of fluorescein that cannot be uptaken by cells, and FITC-Dextran, with a molecular weight of 2 million. We suspect they both would be ideal for imaging capillaries. The latter is about 30 times heavier than the heaviest FITC-Albumin preparation we used, suggesting it will diffuse $\sqrt{30} \approx 5.5\times$ less. Both of these compounds have their drawbacks: carboxyfluorescein will run during fixation, and the heavy FITC dextran is eventually uptaken by tissue, especially if it is not immediately fixed and frozen.

Following a lead in the literature [56], we chose a different tack: perfusion with fluorescent beads (microspheres). Normally used for flow cytometry and labeling, they are made of polystyrene bonded to fluorescein (or another fluorophore) and will readily attach to extracellular proteins. A vial of them is substantially cheaper than FITC and contains 10 mL, exactly enough to replace the blood volume of a rat. We can directly inject at their standard concentration of 1% w/v. They can be purchased in sizes ranging from the tens of nanometers to about ten microns. Initially, we thought

that micron-sized beads would be ideal. They would get stuck in the large vessels, making them glow. Unfortunately, beads above a micron or so in size are large enough to appear as punctate sources surrounded by diffraction rings, rather than producing a smooth glow. Extremely small beads get uptaken into cells, again causing the haloing effect. The ideal size turned out to be 200-400 nm. At that size, the beads no longer got stuck in the large, hierarchical vessels but in the capillaries, which we confirmed using a dissecting microscope. This causes the tissue to glow and the vessels to be dark, essentially enhancing the contrast we see in the autofluorescence images. An example image can be seen in Figure 4.7.

After perfusion, rats were left until their heart stopped beating. At that point, the liver and any other organs of interest were removed, washed with paraformaldehyde (formalin), and then placed into a 10% formalin solution for 48 hours to fix. After fixation, samples were placed directly into a 30% w/v sucrose solution in phosphate buffered saline (PBS) for density matching. While common preparations suggest first placing the sample in 5% and 15% w/v sucrose solutions until they sink, we found that our tissue would sink instantly upon being placed in both. Once the sample sunk, after approximately 24 hours, it was placed in an embedding mold ($22 \times 30 \times 20$ mm), and the mold was filled with embedding medium (Neg-50 from Richard Allen Scientific)⁴. We let the samples sit in the embedding medium for a day to fill any large pores and to attain an equilibrium position in the mold before placing them in a -20°C freezer. Samples were left covered with aluminum foil in the freezer until ready to be sliced. When the time came for use, the Peltier device and water cooling systems were switched on, the sample was uncovered, and additional Neg-50 was added to replace any that had sublimated off and to give a flat surface. The mold was then inverted onto the cold Peltier device, instantly forming a strong bond. Once the sample had frozen onto the Peltier, the embedding mold could be pulled or cut off.

4.5 Automation

Slicing a lobe of liver into $5\text{ }\mu\text{m}$ slices requires 2000 cuts per centimeter, each of which must be followed by a photograph. Automation of our experimental setup was necessary in order to make it high throughput and to avoid unnecessary experimentalist error. We had three systems that needed to communicate with one another: the microtome itself, the camera, and the precision xyz controllers. One of these systems, the microtome, was not electronically accessible; while it had a remote control, Leica was unwilling to share the communication protocol that it used. This

⁴This cryotomy preparation technique was taught to us by the Nottebohm lab and is standard in the literature

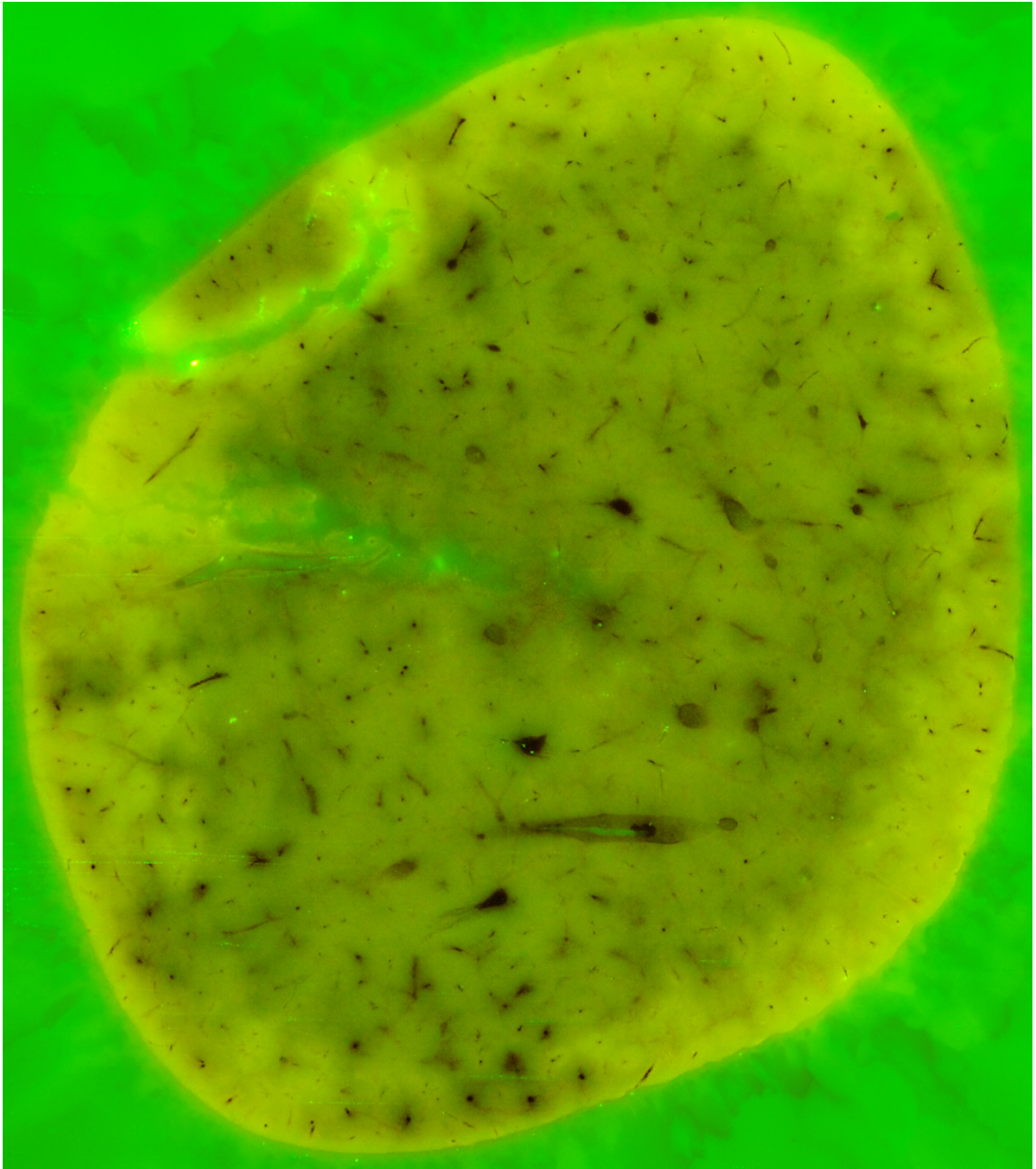


Figure 4.7. A slice of liver illuminated with fluorescent beads. Note the good overall contrast for vascular features, the dark regions, and their sharply defined boundaries. The preparation is the same as in Figure 5.1

necessitated the addition of two more systems: one to press the cut button on the microtome and another to tell if and when a slice had been taken. These two tasks could be accomplished through the use of Phidget microcontrollers. Unfortunately, we were still left with three uncommunicative APIs.

This number could be reduced by one if we were satisfied with only controlling the camera's shutter remotely and not any of its other electronic features. A camera trigger consists of three wires: a ground wrapped around a focus wire and a shoot wire, each of which is held at a different potential. When the trigger is depressed partway, focus connects to ground, a circuit is completed, and the camera runs its focus sequence. If depressed fully, it takes a picture and continues taking pictures as long as the circuit is connected. This system could be hacked by attaching a transistor between the ground and shoot wires. The base pin of the transistor was connected across a $2200\ \Omega$ resistor to one of the digital outputs of the Phidget Interface Kit (see below). The camera's exposure length, F-stop, and output properties were set manually ahead of time. Our electronics setup is shown in the schematic (Figure 4.8) below.

Phidgets are a system of electronic microcontrollers and sensors that can be driven by software from a computer. Generally, one has an "Interface Kit" with a set of digital inputs and outputs as well as analog inputs (for sensors), a 5 V power supply, and a ground. This hub is connected via USB to a computer, which can read the inputs and control the outputs. Software for Phidgets can be written in any number of languages, which proved useful when working with hardware APIs that only run in C. The digital outputs each give a 5 V signal when turned on and need to be connected across a resistor in the $k\Omega$ range when attached to transistors. Phidgets made the task of controlling the microtome easy. A Phidget shortrange IR distance sensor was attached to the bottom of the microtome head and its values for the up (resting) and down (at the bottom of a cut) positions were measured. Whenever the microtome head dropped into the down position, we knew a cut was occurring. When it returned to the up position, we took a photograph.

When using extremely bright LEDs, we needed a way to limit the amount of time that they were on to prevent overheating. A transistor was inserted between the LED and ground and only activated during the time that a picture was being taken. This transistor was connected over a resistor to a digital out on the Interface Kit.

The microtome cutting procedure was driven by an actuator that simultaneously pressed the "Run" and "Enable" buttons on the remote control. The microtome had previously been set to take single $5\ \mu\text{m}$ slices when instructed to cut. The actuator required a positive voltage to extend and a negative voltage to retract. We attached two circuits to a relay switch, one from +5 V to ground

and one from ground to +5 V, both of which connected to the actuator, and switched between them using a transistor connected across a 2200 Ω resistor to one of the digital outs of the Phidget. By flipping the relay, we changed the polarity of the current in the actuator, causing it to extend or contract. The actuator itself was augmented with a handful of Lego bricks to enable it to press two buttons on the microtome panel simultaneously.

Provided we did not need to move the camera in x and y , that is, we did not have to tile a set of images between cuts, we did not need to control the xyz axes during cutting, unless the experimenter decided there would be some utility to doing so. Our software did allow for tiling in a rather unelegant manner. A separate C program controlled the xyz axes, which continually checked a file. If a digit, or a sequence of digits, were written in the file, it would move in a specified fashion and then change the digit in the file. This file was simultaneously checked and written to by the program that controlled the Phidgets. If instructed to, it would take a picture, move the axes (by writing to the file), wait until the move was done (by checking the file), and then take another picture. The z axis, which determined the focus on the camera, was set ahead of time. The entire apparatus is shown in Figure 4.9.

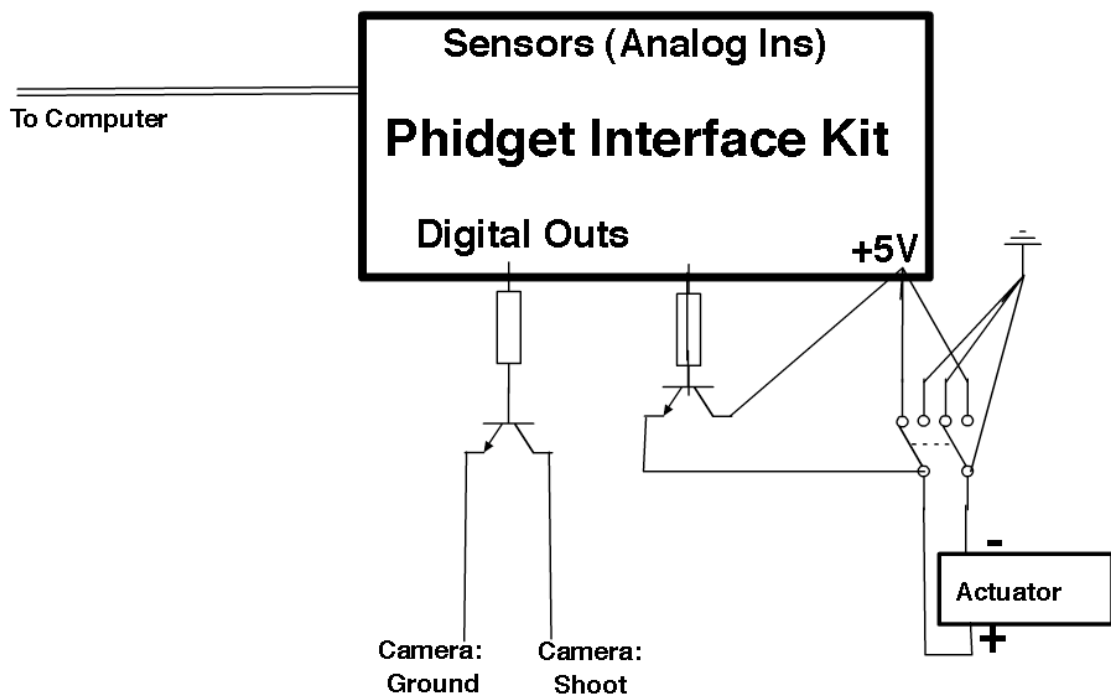


Figure 4.8. Diagram of the major circuits controlling the setup. The phidget interface kit reads in information from sensors (analog in) and controls electronics through the use of 5V digital outputs. One of these controls the firing of the camera, another the movement of an actuator, which extends when given +5 V and retracts when given −5 V. A third circuit (not pictured) could be used to turn on and off an LED.

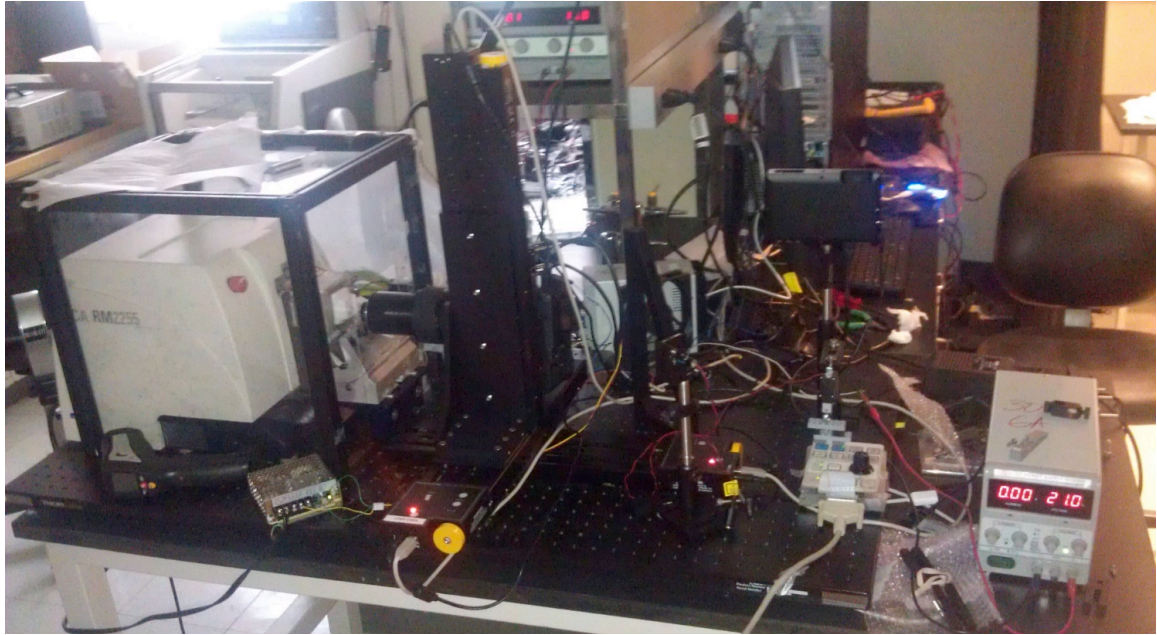


Figure 4.9. Our apparatus: the Scanning Blockface Microtome. On the left, the white box is the body of the Leica microtome, surrounded by a chamber formed of ThorLabs supports and lexan sheets. The microtome head is surrounded by a layer of metal, to which the water cooling apparatus is attached (the green tubes) and the Peltier device (the white square). Mounted on the Peltier is a frozen sample (the white cube). The blade sits below, mounted in the large, silver knifeholder, which is attached to the base of the microtome (the blue metal piece on the optical table). The ThorLabs axes sit just to the right. The camera is behind the z axis, but its back can be seen to the right, with attached wires running to the control electronics and the computer (for image viewing and downloading). To the left of the axes, the makro lens is sticking out. The whitish control panel to the right runs the microtome, note the actuator above the two blue keys, which robotically instructs the microtome to cut a slice. An imaging led, mounted on a silver post is to the left of the control panel. The Phidget control panel and other electronics are behind the axes. The distance sensor that judges when a slice has been cut can be seen just below the microtome head: it appears as a small black rectangle.

Chapter 5

Image Analysis

Given a set of images, we must turn them into a set of binary masks, where the “on” pixels represent vasculature and the “off” pixels represent everything else. A representative slice is shown in Figure 5.1 below. There is a yellow-green blob of tissue, full of dark regions of all shapes and sizes. These are slices through vasculature, from the smallest venules to the largest sections of the portal vein. We see dots and circles where we have cut into a vessel perpendicularly and long cylindrical shapes where the vessel runs parallel to the plane. We even occasionally see two vessels merging, such as in the upper-right-hand corner of the tissue. There are large vessels that appear more like cracks in the tissue, filled with the embedding medium. The tissue is uneven in color and brightness, varying from a bright yellow along the left side in the middle to a darker, greener color in the center. Occasional bright yellow-green splotches are signatures of clumps of fluorescent beads.

There is a multicolored background, illuminated by the scattered fluorescence from the sample. Cracks and imperfections in the embedding medium, arising during the freezing process, lend a complexity to the region around the sample. Outside the frozen block, we see a darker region of scattered light illuminating pieces of the Peltier device and the microtome head.

There are several levels of image processing necessary. First, we must separate the tissue from the background, which includes not only frozen embedding medium but also pieces of the microtome head and peltier. Second, we must isolate vascular features (generally the dark blotches in the sample) from the tissue, despite varying degrees of brightness and contrast in the tissue itself. We are not helped by the occurrence of vascular features on all scales, from small single-pixel scale regions to large areas comparable in size to the entire sample, such as where the portal triad enters the liver.

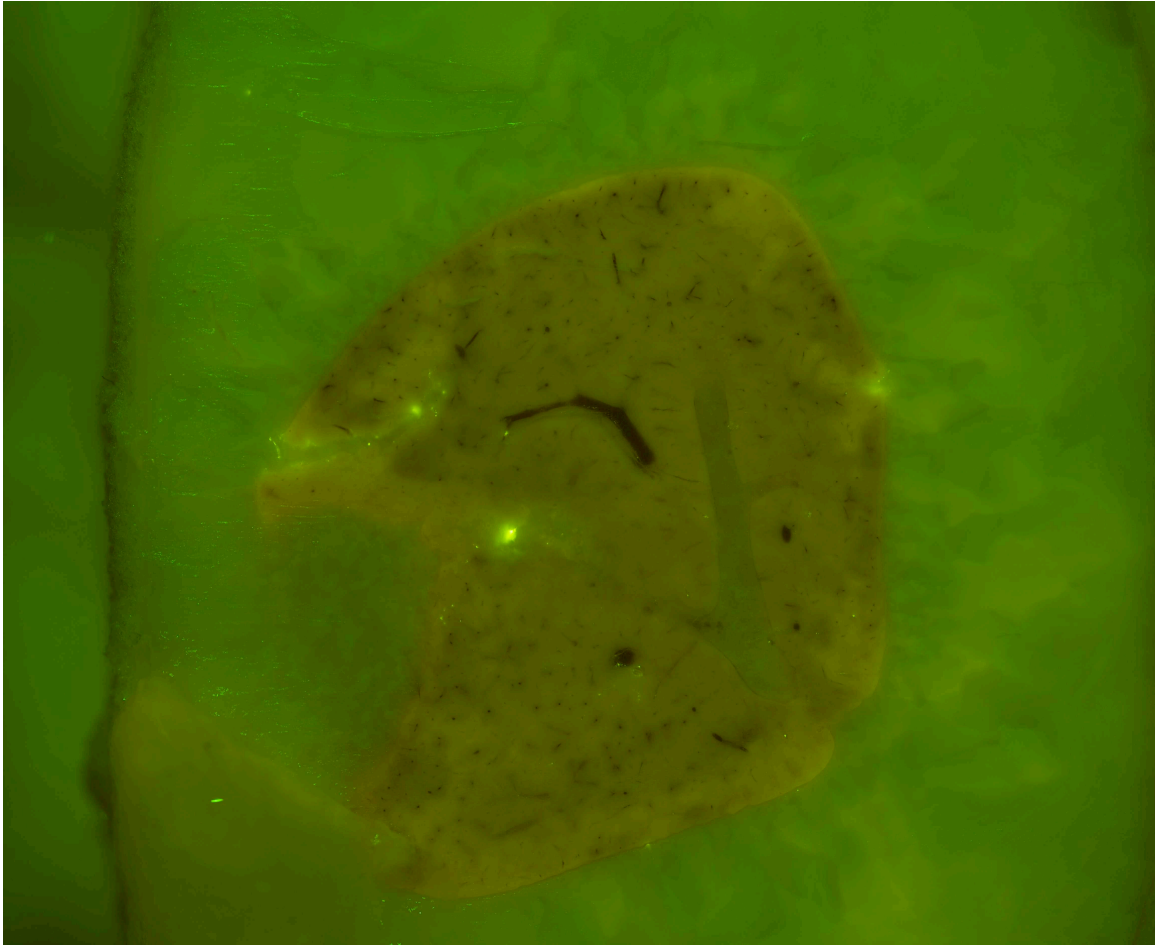


Figure 5.1. A slice of liver from one of our datasets. Note that we must first extract a region of interest (the tissue including vasculature) from the surrounding embedding medium and background before progressing to separating vasculature from tissue. The preparation is the same as in Figure 4.7

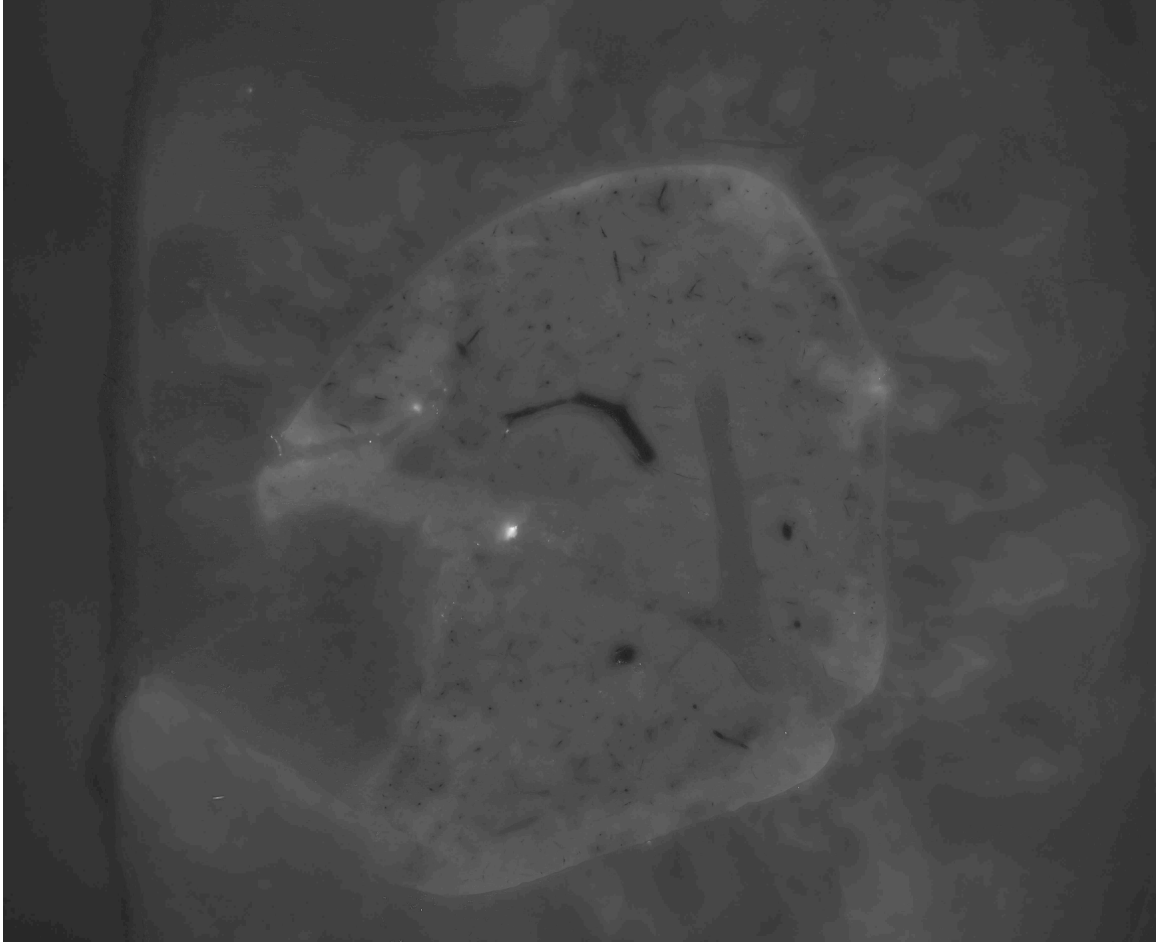


Figure 5.2. Red Channel of the liver slice image. Note the darkness of the background and the relatively low contrast for vasculature versus tissue. We are mostly seeing autofluorescence here.

5.1 What Exactly Are We Seeing?

Given the complexity of our image processing problem, it is best to start by examining the image from as many perspectives as possible. One place to start is the individual color channels that make up the photograph image. In Figures 5.2 and 5.3 below, we display the red and green channels respectively.

The red channel is dominated by the autofluorescence signal, as fluorescein glows in the yellow-green. We are picking up the autofluorescence of various compounds in the liver, activated both by our LED and the fluorescein fluorescence. While this signal is somewhat weak, it clearly distinguishes tissue from the background, which presents only a weak, scattering signal. Vascular features are the (relatively) darker spots but can be hard to isolate on this image, as many of them are not extremely deep in the z direction (into the plane). The autofluorescence from behind brightens them, leaving less contrast. The absolute largest vessels, which appear more as cracks in the sample, are filled

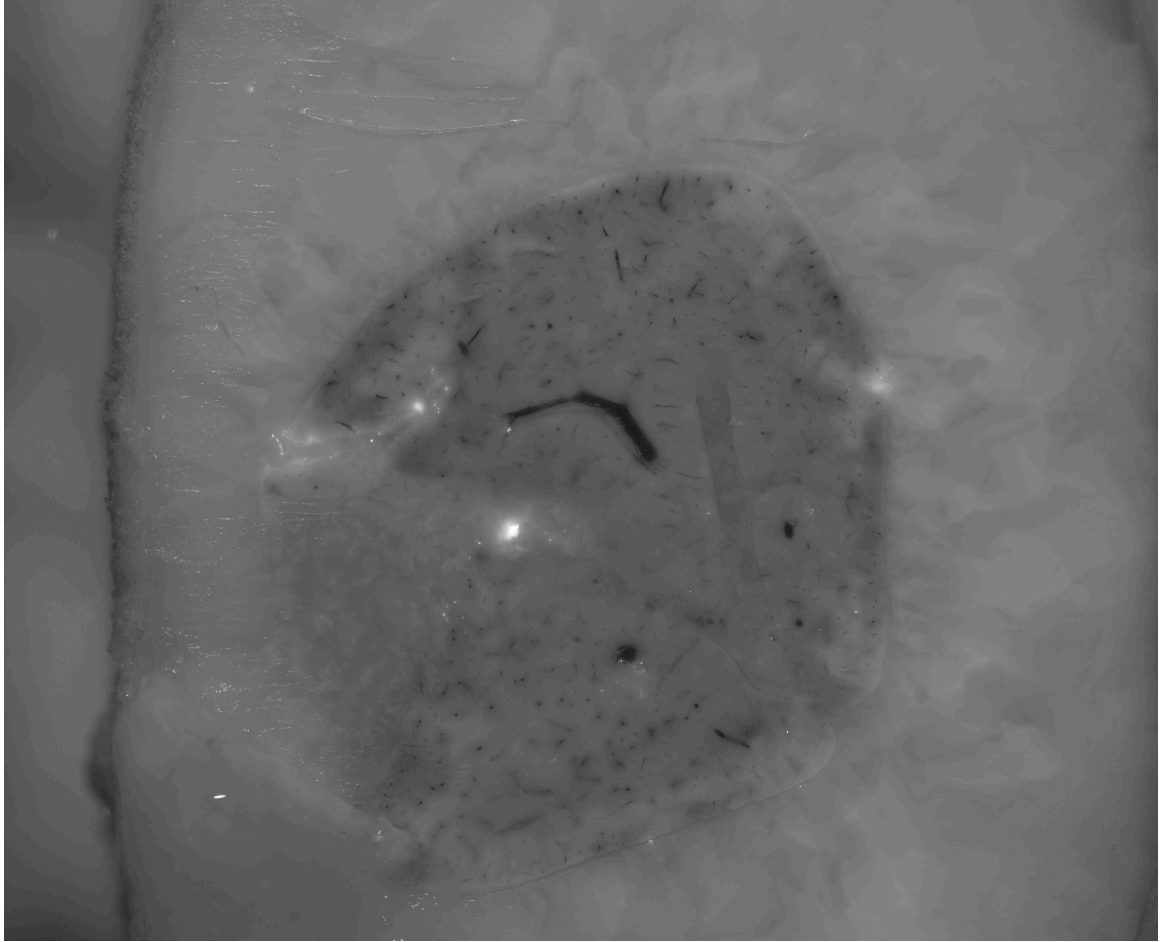


Figure 5.3. Green Channel of the liver slice image. Note the relative brightness of the background as compared to the tissue and the strong contrast between vasculature and tissue. This image is dominated by the light from tissue fluorescence, both direct and scattered.

with embedding medium. As such, they are clearly distinguished in the red channel, whereas in the green channel, they appear as little more than an exceptionally smooth piece of tissue.

In the green channel, the situation is reversed. The vasculature-tissue contrast is extremely good. The fluorescent beads have accumulated in the capillaries, illuminating the tissue as a whole. The vessels are quite dark. On the other hand, the distinction between embedding medium and tissue is considerably more difficult to make. While we can make out the boundary between the two of them, the embedding medium scatters enough of the fluorescence from the sample to appear bright. There is an additional confounding present on the lower-left quadrant of the image. We can see out-of-focus light from tissue behind a layer of embedding medium and even begin to make out the general pattern of vascular features. This layer is invisible in the red channel image due to the weakness of the autofluorescence signal as compared to the beads and the specific attenuation of the embedding medium.

In the blue channel, there is only darkness. This is a good sanity check: if we saw anything, it would be evidence that our filter was not blocking out all of the light of our illumination LED, which, at 475 nm, is filtered into the blue by the camera.

We are still left with the problem of how to remove the background, embedding medium and microtome head, from the images. In the green channel, we have poor contrast between in-plane and out-of-plane tissue, and bright regions of tissue blend smoothly into the background. In the red channel, neither the tissue nor the background is particularly bright, though there is decent contrast between them. What we need is to integrate the two signals: the tissue changes less in brightness than the embedding medium between the red and green channels. This suggests that if we look at the image resulting from dividing one channel by the other, we would get a strong signal. This “ratio channel” is seen in Figure 5.4.

Due to the complexities of the vascular channel, anything that will separate tissue from background will necessarily make vascular regions look different from tissue. We see that effect in the ratio channel, where some vascular regions are extremely bright (reddish colors), due to a strong autofluorescence signal, in the red, perhaps due to residual blood, and none in the green. Natural heterogeneity in the tissue and large vessels filled with embedding medium produce areas where there is little autofluorescence, so the red:green channel ratio is more background-like. There is, however, a strong contrast at the border between tissue and background.

To extract our region of interest, we use a strict segmentation (approximately 1.2, the yellow color in Figure 5.4) and look for the largest connected component of “on” pixels, using the **bwconncomp** function in MATLAB.. This will correspond to the tissue. It will also be full of holes due to the aforementioned areas where bead fluorescence dominates autofluorescence. To correct this issue, we calculate the Euler Characteristic of the draft region of interest, a measure of the genus, or number of holes in an object, using the **bweuler** function. We then perform morphological closing (see §5.3 for details) with structuring elements gradually increasing in size until the Euler Characteristic equals 1, the value for a two-dimensional object without holes. Armed with a region of interest, we may isolate the regions we will search for vascular features by simply multiplying the original images by it.

5.2 The Nature of the Vascular Signal

While the vascular features can be easily segmented by eye, they are not easily computationally distinguished. The regions we instantly pick out as blood vessels are subjectively dark but not

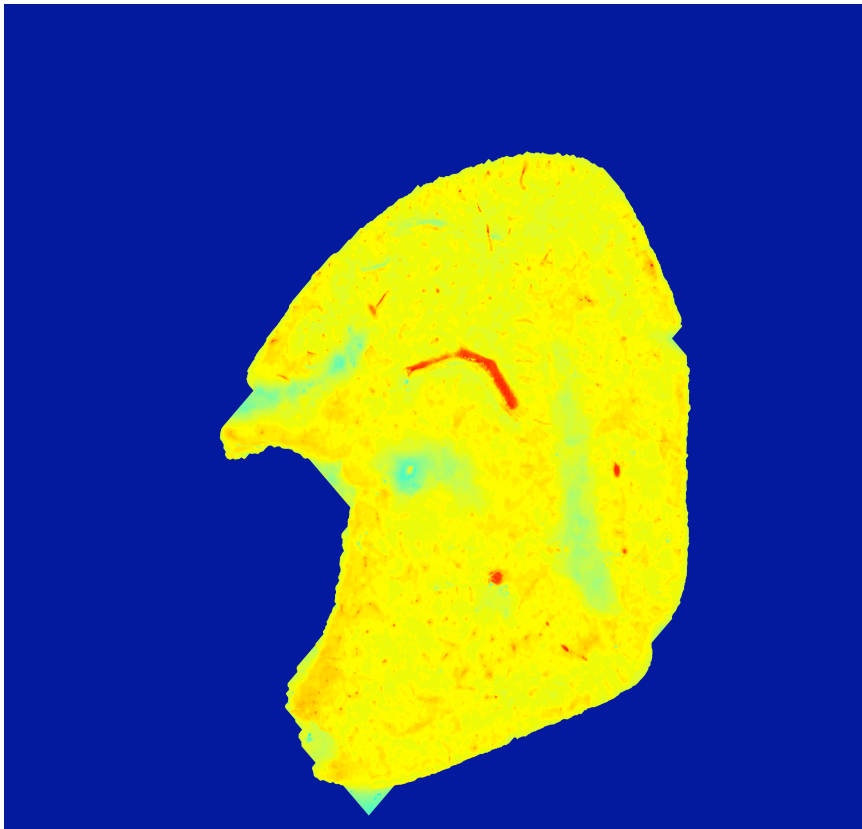
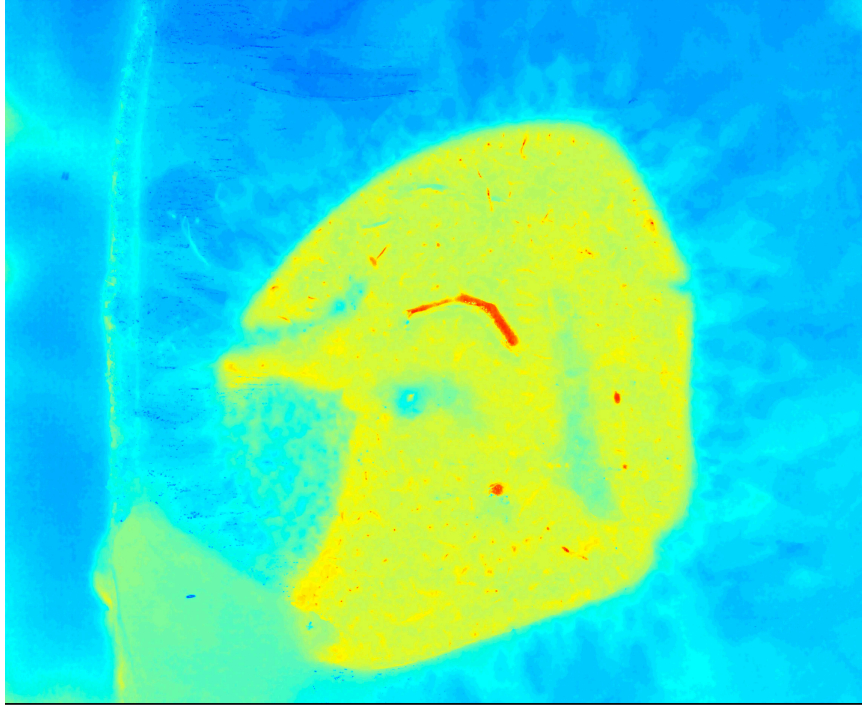


Figure 5.4. Top: Ratio of the Red Channel to the Green Channel. Bottom: Region of Interest extracted from this ratio channel. Note that the tissue is clearly identified. Certain vascular features appear very brightly, as they contain an autofluorescence signal only in the red channel, possibly due to residual blood in the vessels. While the background retains its complexity, it is easily segmentable from the foreground.

objectively so. If we were to segment with a constant threshold, we would either not pick out all of the vasculature, or it would label some regions of tissue as vasculature. For example, consider the top region of Figure 5.3. The outer edge of the tissue is a thin, brighter region bounded on the inside by substantially darker tissue. The interior is a mixture. Many of the regions directly adjacent to the vascular features are dark – they are “anti-haloed.” In the upper right, sections of blood vessel in lighter regions of tissue are no darker than the halos around the vessels in the dark regions. Fainter features would be lost in any overall segmentation operation. To maximize signal-to-noise ratio, we will use the green channel, as it shows the strongest contrast between vasculature and tissue.

What we notice by eye is that vascular regions are darker than the areas that immediately surround them. The vascular regions can be easily separated from their “anti-haloes” by this criterion. This suggests that a relative segmentation procedure is the correct way to proceed. We would subtract the image from an averaged (or smoothed) version itself and the vascular features would stick out as particularly bright. A related procedure would be to take a gradient feature and connect maxima of the brightness gradient. This is the general manner in which edge-detection filters work¹. There are a few problems with this approach. Most importantly, the gradient is a notably noisy operation. When we require precise edges, this poses a severe issue. Our features are also frequently small and have irregular edges. Correcting for small defects where no edge is found would not be trivial. Similarly, false edges would connect separate vascular regions, complicating segmentation. Lastly, an edge-detection filter would find the borders between lighter and darker regions of tissue. Such a result is unacceptable.

Having decided upon the need for a relative filter, we must choose a method of averaging the signal over a region. Two standard methods of doing this are to apply a median or a mean filter. The effect of both on an image of the Duomo in Florence, taken by the author, are displayed in figure 5.5 below. Note that the mean filter merely appears like an out-of-focus image, whereas the median filter accentuates the blocks of color and other features that naturally draw the eye. It is better at preserving boundaries as well, as can be seen by examining the edges of the Duomo itself or the buildings in the foreground. One might say the median filter is more “artistic.” In our work, the preservation of sharp boundaries and the accentuation of large features is an attractive feature in an averaging method.

Statistically, a median filter is likely optimal for work on a noisy image with somewhat rare, darker vascular pixels. The median is the value that minimizes the L_1 norm for every point in a

¹As an example, the famous Canny edge-detection filter uses a derivative of a gaussian: a gaussian smoothing and a gradient to detect edges.



Figure 5.5. At the top is an image of the Duomo in Florence. On the lower left is a median filter. The lower right is a mean filter. Note the more naturalistic, perhaps artistic feel of the median filter, as opposed to the mean filter, which appears fuzzy. Photos by the author.

set, whereas the mean minimizes the L_2 norm, or the mean square distance. A mean filter, thus, will drag down the overall brightness of a region due to the vascular pixels present in it, as it more strongly weights exceptionally dark or exceptionally bright points. Similarly, if the background of a region is slowly changing in color in an uneven fashion, the median will give a more representative value than the mean, as it does not assume linearity [50]. We implemented a median filter using the **medfilt2** function in MATLAB.

Once we choose a method of averaging, we must decide how much area to average over. Since there are many small vascular features comprising only a handful of pixels, we likely wish this region to be small to preserve context. It seems reasonable to begin with an area 20 pixels to the side, or 100 μm . The result of this operation is shown in Figure 5.6 in the top row with the filtered image at left and with the original subtracted at right. The median filter preserves many (if not most) of the vascular structures we saw by eye; they are simply too large to be smoothed out by a 20 pixel filter. At right, we can see that the extracted signal is weak, seemingly consisting of punctate dust. We are extracting only the smallest vessels without a hint of the larger ones. Clearly another size filter is necessary.

Moving to a 100-pixel median filter (500 μm), we see considerably more. The median filtered image shows mostly splotches of color, corresponding the overall brightness of the image within a region. After subtracting the original, we see vascular features of a range of sizes, larger ones in the center, smaller ones nearer the top and bottom of the image. If we look more closely at the top of the image, though, we can see that the smallest vascular features, the punctate dust picked out by the small median filter, are not reproduced by this larger one. Additionally, the largest blood vessels in our image, the branch of the portal vein at lower right and the dark arc in the center, are not well extracted by a filter of this size. It is clear though that we need a set of filters in order to properly extract all the vascular features. In this case, it appears a small, a medium, and a large one will do.

Setting up a larger median filter is somewhat tricky. As the size of the filter increases, so does the time necessary to run it. We also need to be clear what large features we are looking for; not incidental variations of brightness across the sample but large vessels filled with embedding medium. Returning to Figures 5.2 and 5.3, we see that these features are considerably stronger in the red channel than the green. For this largest filter, we should use the red or the ratio channel. We also must choose its size such that the largest vessels are picked out but not the incidental variations in brightness across the sample. We settled on 300 pixels, or 1.5 mm. The results are shown in the bottom row of Figure 5.6.

Applying filters to an irregularly shaped region surrounded by a background one desires to ignore

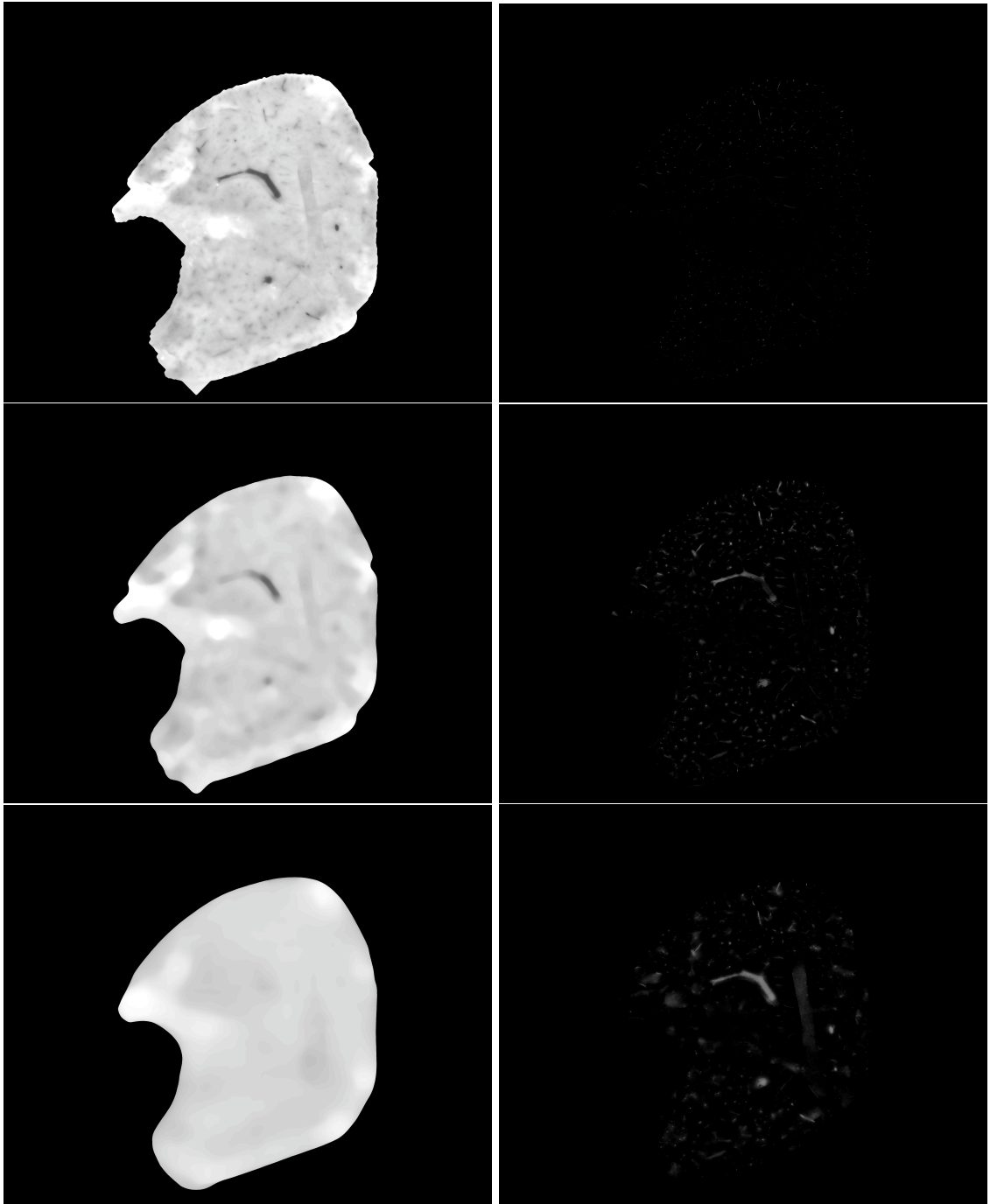


Figure 5.6. Median Filters at varying radii and the features extracted when the original image is subtracted. In the left-hand column, a median filtered version of the green channel of our image is displayed. In the right column, we display the median filter with the original image subtracted, highlighting the vasculature. The top row has a median filter of size 20 pixels, the middle of 100 pixels, and the bottom of 300 pixels.

is inherently problematic. If we apply the filter to an image multiplied by the region of interest, rendering the background black, we will create darker-than-normal regions for the inside edge of our sample and brighter-than-expected regions just outside of it. Since our region of interest isn't perfectly coterminal with the tissue, this leads to numerous false positives around the edges. Our solution is to only look at points a distance of one pixel or greater from the edge. While this deprives us, theoretically, of some vascular features, it helps ensure that we do not mark the boundary of the tissue as vasculature.

The last step in the relative filtering is to decide what level of brightness difference between the filtered and the original images constitutes evidence for vasculature. To properly normalize our data, we perform a round of histogram equalization using MATLAB's `IMADJUST` function on the original image before filtering. Empirically, we noticed that smaller vascular features gave a weaker signal, perhaps because they skewed the median filter in their region more strongly, perhaps due to secular brightness fluctuations. We marked everything in the 11th brightness bin (out of 256) or higher vasculature for the small filter, the 16th and higher for the medium filter, and the 21st or higher for the large filter. These thresholds were chosen by examining the image histogram and choosing the point that best separated the generally normal distribution of brightness of the tissue pixels versus the long tail of vascular pixels. This effort was complicated by the existence of a "hard wall" of brightness at the 0 bin, yielding only half of a gaussian to work with. If both sides had been in evidence, it would have been easier to estimate where the normal fluctuations in brightness ended and the vascular features began by comparing both halves of the distribution about its center.

The issue of brightness abutting zero suggests a new version of the feature extraction algorithm less reliant on thresholds extracted by eye. This scoring algorithm would repeat the three-filter process above, but instead of definitively marking a pixel as vasculature, it would assign it a score, based on its distance from the edges of the normal distribution of brightness fluctuations, akin to a z-score in statistics. If we convert our images to double-precision numbers, as opposed to the unsigned 16-bit integers that the camera assigns, we can allow for negative brightness values, giving us the full distribution. Setting thresholds is then greatly simplified, and we have the advantage of being able to look at the tail of pixels that are much darker than average. In a properly perfused animal, these would not be particularly useful. However, if there are large vessels full of beads, they will appear brighter than the tissue on average, and lie in the darker-than-average tail. This tail also contains border regions from just inside the sample, where the median filter averaged over pieces of purely black background. This process can be done both on the red and the green channels, as well as the ratio channel if so desired, giving us nine potential sources of vascular detection ($\times 2$ if

the dark tail is included). We may then assign a score, either binary or based on log differential brightness² and then taking all the pixels whose score is greater than some amount. In the dataset described in this thesis, that minimum score was one. In other datasets, this has not been the case.

No matter the method chosen to determine which pixels constitute vasculature, be it a union of the brightest elements in three separate filterings or a scoring algorithm, we are left with a binary mask that provides an estimate of which pixels constitute vasculature. Those we take to be vasculature are “on” with a value of unity. Those that are background are “off” with a value of zero. We have greatly compressed our images, in taking them from 3 channel, 16 bit tiffs to binary masks. This initial mask is shown in the lefthand panel of Figure 5.7.

5.3 Morphological Operations and Cleaning

While we have done a fair job of capturing most of the vasculature, there is still an abundance of false positives, or noise that we have marked as vasculature, and false negatives, vascular pixels that have gone unmarked, leaving holes in the regions we have determined to be blood vessels. For the false positives, we need a procedure that will eliminate features that are below a certain size and/or are not extended in any direction; to pull out punctate shot noise, but preserve vasculature. For the false negatives, we need a way of connecting isolated pixels that have been marked as vasculature but are separated by gulfs of background pixels. If we have missed a vessel altogether, we cannot rescue it. While this statement is somewhat tautological, it suggests the proper order of operations for fixing defects in our mask. First, we should try to connect disparate pieces of vessel and only afterwards should we attempt to denoise our data by removing isolated components.

False positives and false negatives in our image are in some sense the dual of one another. False negatives can be thought of as false positives for the background, while false positives can be viewed as false negatives for the background. Viewed from this angle, a denoising procedure and a connecting components procedure are not so different. One is applied to the original image and to its inverse with all the “on” pixels turned to “off” and vice versa. Because the statistics of the foreground and background differ, this duality relation does not hold exactly. We expect vessels to look like sections of cylindrical tubes and the background to look like swiss cheese (to first order). An operation that perfectly removes false positives for the foreground is clearly not the ideal one to remove false positives for the background. Mathematical morphology provides the proper set of

²Most vascular pixels are not too different in brightness from the original sample, and we desire maximum control in the low score region. Additionally, we naturally judge brightness logarithmically (the Weber-Fechner Law). Hence, compressing the scale with a logarithm is reasonable.



Figure 5.7. Initial binary mask created by taking the union of all the pixels marked as vasculature in the three relative median filters. Note the abundance of false positives and false negatives.

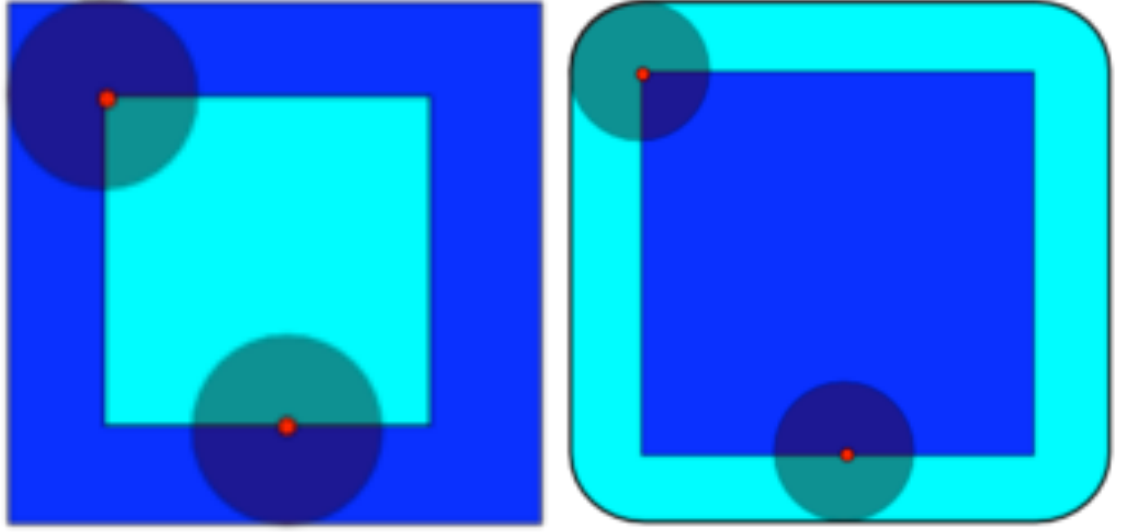


Figure 5.8. The Erosion (left) and Dilation (right) operators. The original image, A is the dark blue square, the structuring element, B is the gray circle, centered at the red dot. The resulting image is the light blue square. Images from [47].

tools for both of these procedures: any operation that we specify for the “on” pixels has its dual that performs the equivalent for the “off” pixels [50].

The two fundamental operations of mathematical morphology are the erosion and dilation operators. We consider an image, A , and a structuring element (or filter), B defined on a grid, E , with B_z denoting B centered at a point z . We define the erosion operator as:

$$A \ominus B = \{z \in E \mid B_z \subseteq A\} \quad (5.1)$$

Hence, the erosion of A by the element B is equal to those points in A , where if we center B , B only contains points in A . An example can be seen in the left-hand panel of Figure 5.8. The dilation operator is precisely the dual of the erosion operator:

$$A \oplus B = \bigcup_{z \in A} B_z \quad (5.2)$$

Dilation represents the union of all points within B when B is centered at every point in A . It is shown in the right-hand panel of Figure 5.8 [50].

To put these operations to good use, we may define two second-order operations, also duals of one another, opening and closing. Respectively, these are an erosion followed by a dilation and a

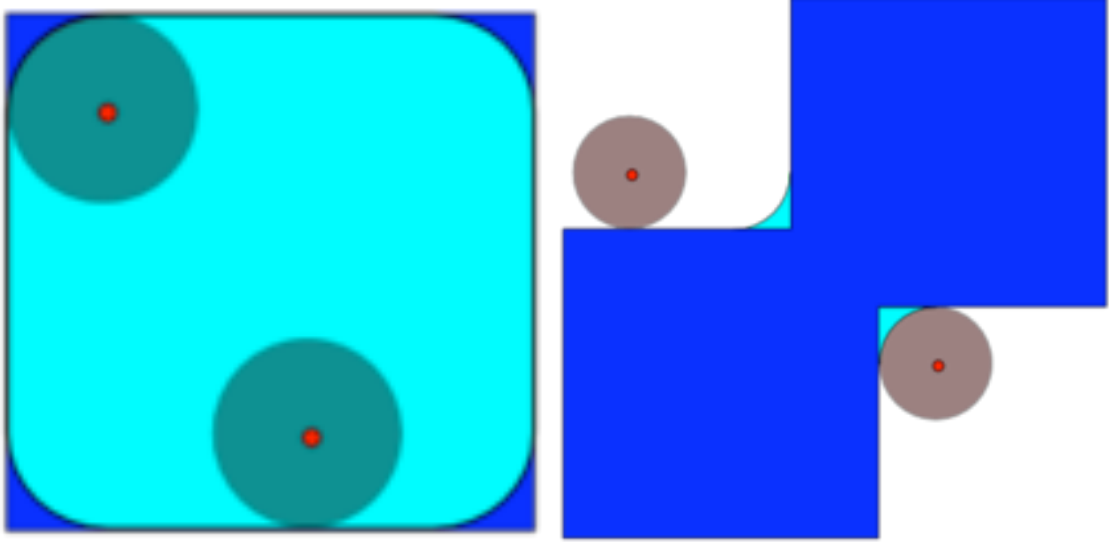


Figure 5.9. The Opening (left) and Closing (right) operators. The original image and structuring element are the same as before. In the case of opening, note how the initial erosion leaves a new shape with rounded corners, so the subsequent dilation does not return the original shape, but a smoother version. In the case of closing, the opposite occurs. The initial erosion leads to regions that cannot be removed by a dilation. Images from [47].

dilation followed by an erosion [50]. We write them:

$$A \circ B = (A \ominus B) \oplus B \quad (5.3)$$

$$A \bullet B = (A \oplus B) \ominus B \quad (5.4)$$

Examples may be seen in the left and right panels, respectively, of Figure 5.9. Morphological opening “opens” gaps between separate objects and closing “closes” them. A dilation that fills a hole will not be undone by a subsequent erosion, hence closing. An erosion that opens a distinct gap, or in the case of Figure 5.9, sands the corners off of a shape, will not be undone by a subsequent dilation. Opening will also erase regions smaller than B surrounded on all sides by points not in A . In the case of stable shapes, both closing and opening do nothing, making them ideal for the removal of false positives and negatives. Our program is then a round of morphological closing to fill in holes of “off” pixels surrounded by “on” pixels and to bridge gaps between areas that should connect, followed by a round of morphological opening to remove noise.

We have yet to specify the structuring element, B , however. During morphological opening, it will specify our minimum feature size and shape. For simplicity and maximal resolution, we chose a 2×2 pixel square. This meant the smallest vascular features we accepted would be $10 \mu\text{m}$ on a side, small enough to still capture all of the hierarchical vessels but large enough to get a real

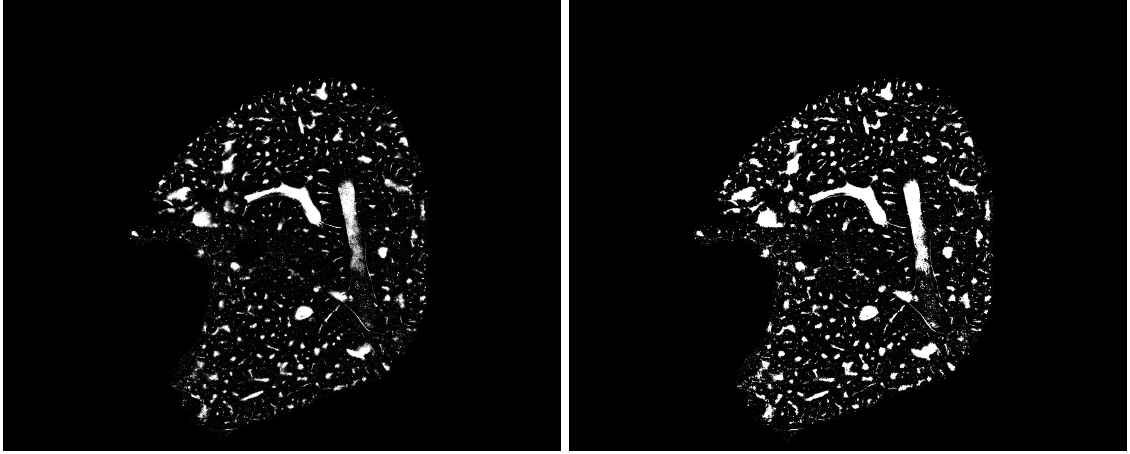


Figure 5.10. Morphological Closing on the draft binary mask of our example slice.

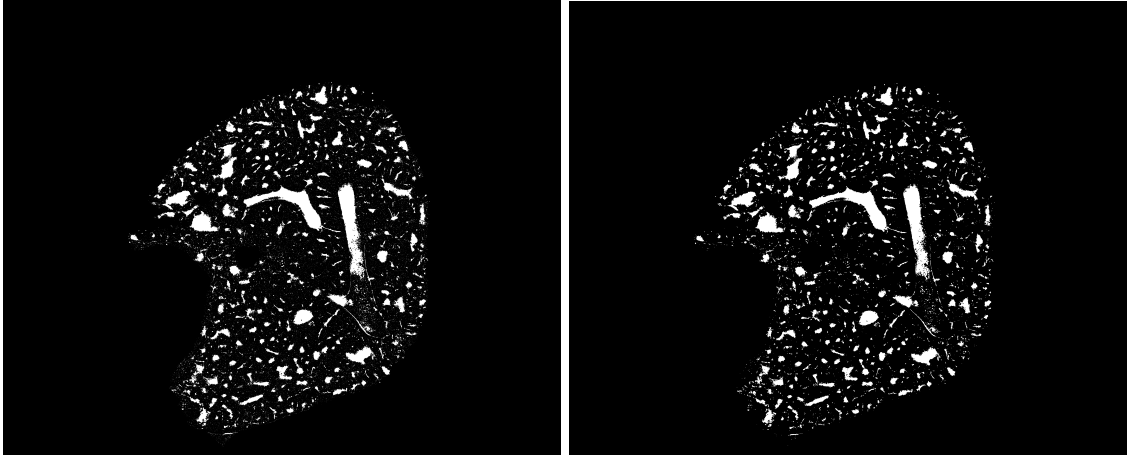


Figure 5.11. Morphological Opening on the morphologically closed mask of our example slice.

improvement in signal to noise ($\approx \sqrt{4} = 2\times$ improvement). For the closing, we desired a structuring element large enough to fill in gaps of moderate size without generating new, false connections. We chose a rhombus of radius two pixels as a useful and fast approximation of a circle. The results of our morphological operations are shown in Figures 5.10 and 5.11. We see a substantial improvement in the quality and quantity of vascular features extracted from the images.

There still remain issues in this image, mostly related to the large vessel in the lower-right quadrant of the image, which is still not filled in entirely. Additionally, some features in the upper-left quadrant appear to be overly large. This is no reason for despair, however, as we have 1760 images in our dataset. A false positive in one image is not likely to be a false positive in the images before and after. As such, it will only slightly contaminate the appearance of our dataset without affecting its mathematical properties. The distance transform will not be affected by a slight projection in one z slice. Neither should the skeleton (see §6 below) be disturbed by a slight

protrusion in one direction.

Similarly, a piece of vessel left unfound in one image is likely to be found in a neighbor. A round of morphological closing in the z direction, implemented either in the xz and yz planes or truly three dimensionally (see §5.4 below), will suffice to close these gaps. If we carefully examine the original image (Figure 5.1 above), we will see that the area left uncaptured is significantly shallower in the z direction than the captured region. If we imagine looking down into the sample, we are near the “bottom” of that piece of vessel. Hence, leaving it uncaptured should not trouble us too much.

Ultimately, however, these issues are a reminder that, provided proper computing resources, all of the morphological operations should be done in three dimensions. We would take the initial masks, perform a denoising step via morphological opening, align these modestly modified masks using the procedure in §5.4, and assemble a z -stack of the unaltered images using the alignments from the denoised images. The morphological closing and opening steps would then take place fully in three dimensions. We could connect features fully in three dimensions with an approximation of a sphere of radius two or three pixels as structuring element using morphological operations. Similarly, we could do a real denoising step, where we made sure that punctate features in one image did not exist in the following image, using a $2 \times 2 \times 2$ cube as structuring element. The signal-to-noise ratio would improve by a factor of $\sqrt{2}$ as we went from averaging over four pixels to averaging over eight.

5.4 Moving to Three Dimensions

Once we have a set of binary masks, they need to be connected in the third, z , dimension. As the microtome head moves during the slicing procedure, there will always be a bit of noise in its position: it returns to its original position $\pm 10 \mu\text{m}$. Additionally, the varying shape of the tissue and how it is embedded in the mold can lead to a need to move the camera during slices. Consider an oblate ellipsoid of tissue, mounted at an angle in the mold, either due to stability reasons or by an accident of freezing. The initial slices will have tissue to one side, say the right, but as one continues cutting the tissue, the tissue will move through the center of the mold area to the left. An occasional move of the camera to center the tissue within the frame is easily accomplished but must be corrected for in post processing. Alignment is vital to the entire enterprise.

As our slices are about the length scale of a single cell, we do not predict there to be much change in the features of the tissue between consecutive slices. This makes a correlation-based approach both easy and relatively practical. If we were not in this regime, for example if we were cutting at 10 or $20 \mu\text{m}$, we would need to align based on the edges of the sample, a considerably more complicated

prospect. While the boundaries of each slice are clear to the naked eye, extracting them perfectly, as opposed to a general region of interest, is difficult; additionally, there are fewer pixels on the perimeter to inform our correlations than there are vascular pixels in the interior.

A naïve implementation of a correlation function is not efficient. Multiplying millions of pixels by each other, summing over all of them, and repeating the procedure for tens of thousands of potential shifts (one hundred pixels in each direction) between hundreds of images is not practical even if we use binary masks. A slight speed-up can be gained by using hardcoded functions, such as **corr2** in MATLAB. The need to search up to 200 pixels in each direction (for 40000 possible shifts total) makes any direct implementation of correlation impractical. Our solution has been to exploit the Wiener-Khinchin theorem and use the two dimensional Fourier Transform³. Alternatively, one can think of the Fourier Transform in the physical terms of quantum mechanics, where it is nothing other than the generator of translations.

Practically speaking, if we consider an image, $I(\vec{x})$, where \vec{x} is a discrete vector of coördinates, then $I_{shift} = I(\vec{x} + \vec{r})$ represents I with a shift corresponding to the vector \vec{r} . To extract \vec{r} , we need only to take the ratio of the Fourier transforms of the two images.

$$\tilde{I}(\vec{k}) = \int I(\vec{x}) e^{i\vec{k} \cdot \vec{x}} d\vec{x} \quad (5.5)$$

$$\widetilde{I_{shift}}(\vec{k}) = \int I(\vec{x} + \vec{r}) e^{i\vec{k} \cdot \vec{x}} d\vec{x} \quad (5.6)$$

$$= \int I(\vec{x}) e^{i\vec{k} \cdot (\vec{x} - \vec{r})} d(\vec{x} + \vec{r}) \quad (5.7)$$

$$= \tilde{I} e^{-i\vec{k} \cdot \vec{r}} \quad (5.8)$$

The ratio of \tilde{I} to \tilde{I}_{shift} gives us a planewave with wavevector \vec{r} , in Fourier space. The imaginary part of the logarithm of this ratio will be linearly increasing along the direction of \vec{r} , modulo 2π . We have found that the best way to extract this value is to Fourier transform back to real space and then look for the peak of the power spectrum. This will be the dominant mode of the triangle wave, corresponding to $\vec{k} \cdot \vec{r} \bmod 2\pi$, which is precisely our shift. The success of the alignment procedure can be seen in Figure 5.12 below. Note the successful connectivity in the third dimension as well as the lack of shot noise issues.

Once we are connected in three dimensions, we can simply run a round of morphological closing in three dimensions either directly or between collections of slices in both the xz and yz planes.

³The Wiener-Khinchin, or correlation, theorem states that the correlation between f and g is simply the inverse Fourier transform of the product of the Fourier transforms, \tilde{f} and \tilde{g} .

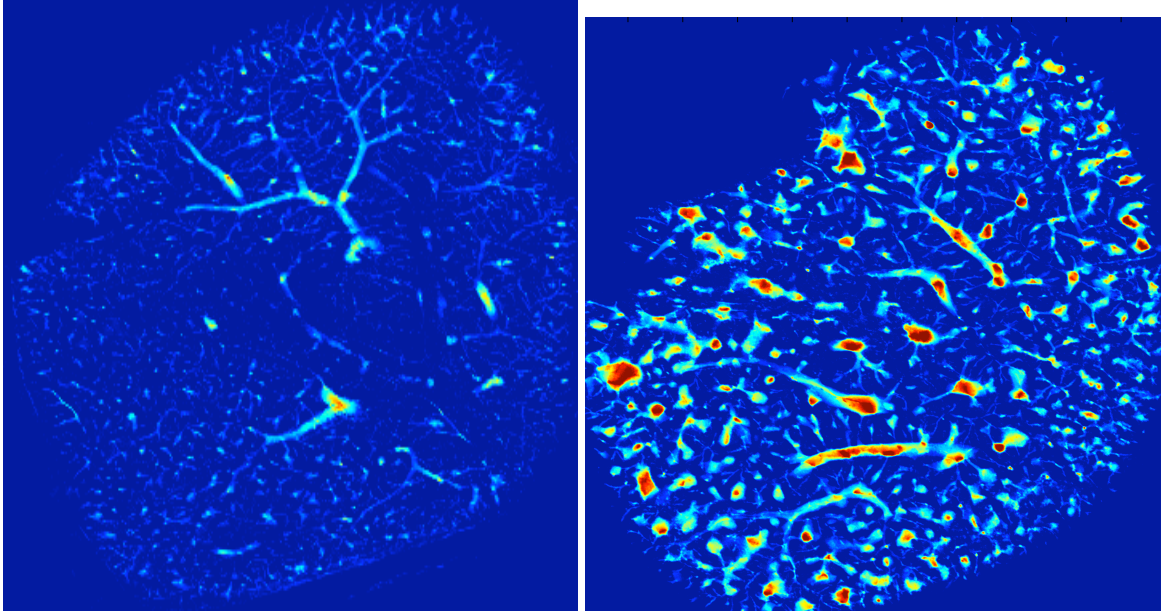


Figure 5.12. Series of aligned images showing three-dimensional features of our dataset. These figures are heatmaps summed over several slices: brighter colors correspond to more vascular pixels in the z -direction. On the left, 100 slices (500 μm) without the largest vessels (those isolated from the two largest of the relative median filters) are displayed. On the right, are 50 slices (half the thickness of the left) with all the vessels displayed. Note the connectivity in the third dimension.

Again, we use a rhombus (or rhomboid) structuring element of radius 2 pixels (10 μm). We can use an iterative implementation of a FLOODFILL (see below) to see what fraction of the vascular pixels belong to the largest connected component. Before the closing, this value is $\approx 85\%$. After, it is $\approx 95\%$, indicating successful connectivity in three dimensions.

As FLOODFILL will keep recurring as a useful tool in this thesis, now is an opportune time to define it. The basic idea is to choose a starting point, color it, then repeat the process with its neighbors. The process then repeats until there is no pixel bordering a colored one left uncolored. If we have a series of disconnected components, we can choose a random point, run FLOODFILL, then jump to a new, uncolored random point, and color it another color. Once there are no uncolored points remaining, we can tell from the number of colors used how many connected components there are. Ideally, this algorithm is run recursively, in which case it is extremely fast. In the case of our images and the skeleton, however, it needs to be run with a queue, as there are too many pixels to recurse without running out of memory. This iterative FLOODFILL marks the neighbors of a colored point as “to visit” and places them at the end of a queue. It then moves to the next point in the queue, colors it, and adds the neighbors. The use of a “to visit” color prevents the multiple addition of points to the queue.

Lastly, all cavities in the dataset are filled: we look for regions of “off” pixels that do not connect with the background. Physically, these would correspond to tissue surrounded on all sides by blood vessel – a biologically dubious situation at best. We correct these anomalies by turning all of these pixels “on.” While these regions can theoretically be found with a simple FLOODFILL on the “off” pixels, to speed the process of finding them, we iteratively color the background a third color from the outside. This greatly reduces the number of pixels that need to be examined. With the passage from two dimensions into three, we move from the problems of image analysis to those of skeletonization.

Chapter 6

Skeletonization

Ideally, we would like to visualize this data directly. Unfortunately, the size of our dataset makes this task impossible. After alignment, we have approximately 4000×6000 pixels in xy and 1750 images in z . Even as binary pixels, this still yields approximately 43 GB of data, which runs up against the limits of commercially available machines. We can achieve some improvements by trimming our dataset: many of the xz planes (constant y values) especially are all 0s. The same is true for some of the yz planes. By removing all the planes containing less than 10 or so on pixels, which we assume to be due to shot noise creeping in from loosely defined regions of interest in individual images, we can reduce the size to $3770 \times 3021 \times 1750$ voxels, or about 19 GB of memory. Of these voxels, ≈ 973 million are “on,” or vasculature, representing just under 5% of the dataset.

While it is possible to coarse-grain this data to a more manageable size, then display it in any number of three-dimensional viewing formats, the act of setting a threshold for an “on” value in the new, larger pixels is problematic. If set too low, or even to one, the image becomes a solid mass. The vascular tree, even without the capillaries, is close enough to being space filling. If set at a higher level, around 50%, large sections of the tree will be apparent. However, the boundaries will also appear like thick solid blocks. This issue originates in the high density of small, thin vessels along the edges of our sample. When coarse-grained, these “treelets” are at high enough density to form thick blobs. With some tweaking of parameters, we were able to print a passable 3d model, whose defects, however, would become dramatically more visible as a rotating image.

The fruits of our work in image processing thus remain beyond our sight. They are also beyond the reach of mathematics: thick bands of pixels cannot be analyzed in any useful manner as a network of branching and intersecting tubes. We can get neither a qualitative or a quantitative

handle on the data in its current form. It is this dilemma that leads us to skeletonization.

The need to reduce our dataset to a mathematical graph, or a set of nodes and edges, suggests a new tack: to reduce our thick and bumpy vessels to single pixel thick lines. This process is known as skeletonization. Skeletonization can be an effective way to compress complicated three-dimensional shapes. If one can reduce a region to a sparse set of points and their distance from the background, there is an efficient way of storing it. There are two constraints to this procedure: that the skeleton shares the same topology as the original image and that it contains only points that are equidistant from two or more boundary points. This second, geometrical constraint codifies the intuition that no compression is going on if you are simply taking points a distance n from each boundary and marking them with a radius n .

6.1 Algorithms

The construction described above is an ideal image skeleton. Mathematically, it would be defined as the Voronoi diagram of the boundary of the image and would satisfy both the topological and geometrical constraints. As we have millions of points in three dimensions, this calculation is not practical to implement. The remaining algorithms satisfy only one of the two constraints exactly. We may implement a geometric algorithm that finds the points equidistant from the boundaries or a topological algorithm that “thins” the image without changing its topology until it is reduced to a single-pixel width.

Finding the set of points equidistant from at least two boundary points is easy to visualize. We are looking for the centers of the circles (in two dimensions) or the spheres (in three dimensions) that are tangent to the boundary in at least two places. The locus of all these points is the geometrical skeleton of the object. One approximate way to do this is to take the distance transform of the object, defined to be the distance of each pixel (or voxel) from the nearest boundary, and look for ridges: places where the gradient is either stationary or changes sign. While easy to implement, this method has issues with places where a small feature impinges on a much larger one, such as the T intersection, where the vertical is considerably narrower than the horizontal. With modest resolution, there will be places where ridges simply end and need reconnection [28, 44]. In practice, what is used is a grassfire-type algorithm where points are sequentially removed from the boundaries. When two removal fronts (or fires) meet, their location is marked as part of the skeleton. A common implementation in two dimensions uses morphological erosion. This algorithm was used to generate the skeletons in Figure 6.1.

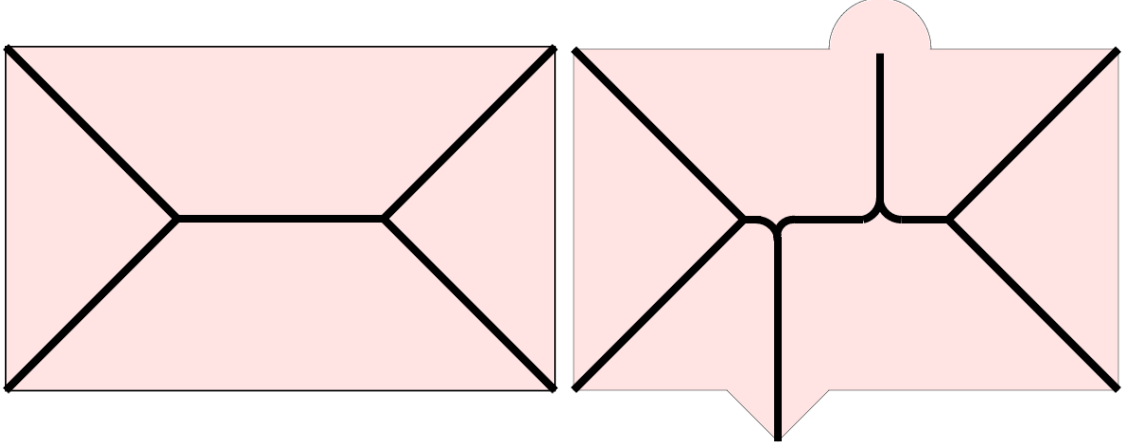


Figure 6.1. Geometric skeletons of a rectangle in two dimensions. Note the strong effect on the skeleton exerted by small defects in its boundary: inducing two additional lines that do not conform to the rest of the shape, as seen on the left. Note also that the corners of the rectangle induce the forked protrusions at either end of the skeleton, neither of which has much resemblance to the shape as a whole. Figures from [44].

Looking closely at Figure 6.1, we see a variety of issues. For even a simple rectangle, the geometric skeleton is in the shape of a double-tailed arrow, due to the corners, rather than the extended line we might have imagined. If noise is added, in the form of surface defects, new skeleton components are generated, greatly changing its graph structure, if not its topology¹. The introduction of new skeleton components is completely unacceptable for our vascular data. Since we desire our skeleton to contain the vessels and only the vessels, we need a topological algorithm.

A topological algorithm moves through the image, considering each voxel in turn and removing it if and only if its removal does not affect the topology of the image. Since the connectivity is purely local, we only need consider the $3 \times 3 \times 3$ cube of voxels, centered on the one being considered. How to decide which voxels can be removed (“simple points” in the literature), however, is considerably more fraught. There are 27 voxels in a $3 \times 3 \times 3$ cube. Since we are considering turning the central voxel from “on” to “off,” there are 26 voxels whose identity could differ. This leaves us with $2^{26} \approx 67,000,000$ cases, far too many to calculate by hand or even to easily visualize. This differs from the two-dimensional case where there are only $2^{3^2-1} = 256$ cases, many of which are related by simple rotations. That is a small enough number of cases for each to be examined individually.

The three-dimensional skeletonization literature is riddled with improper analogies to two dimensions, algorithms that work only in some subset of cases, and sloppy mathematics. To our knowledge, ours is the first nontrivial dataset to which three dimensional skeletonization has been applied. Lee

¹Technically, no topological invariant, such as the Euler Characteristic Changes here, as we are just adding pairs of edges and vertices, which cancel out: $\chi = F - E + V$. That said, the structure is still quite different.

et al. attribute this to a paucity of three-dimensional data worth skeletonizing until recently, the underdevelopment of digital topology, and the greater difficulty of visualization in three dimensions. The original algorithm by Morgenthaler, while technically correct, is impractical to implement, as it involves checking for changes in the number of two-dimensional holes among both the “on” and “off” pixels [34]. In the attempt to avoid this calculation, many other research groups went astray, believing that a lack of change in genus [30, 59], or number of foreground and background objects [57], was sufficient. A connectivity approach by Bertrand and Malandrin [4] could not be verified to work by us. The literature is riddled with citations to these earlier, incorrect papers, likely due to the lack of application of these algorithms currently. The paper by Lee, Kashyap, and Chu gives an exhaustive discussion of these issues as well as a correct algorithm for topological skeletonization [29].

Rather than present a walkthrough of the Lee et al. algorithm [29], we will begin with a discussion of basic considerations in digital topology in three dimensions, focussing on the choice of a grid. We will then derive their algorithm from basic desiderata and computational feasibility, presenting our changes and implementation along the way. In this manner, any differences of opinion and/or potential mathematical errors can be easily identified, removing an obstacle to understanding from the literature.

6.2 Digital Topology in Three Dimensions

Having decided on the use of a topological algorithm, we now must define digital topology in three dimensions. Specifically, we must choose a grid. In two dimensions, one can consider the pixels that share an edge with a central one to be its neighbors, yielding the “4-neighborhood,” or all the pixels that abut it, and the “8-neighborhood,” which additionally includes the four corners. In three dimensions, we have the choice of those pixels that share a face, the “6-neighborhood;” those that share at least an edge, the “18-neighborhood;” or those that touch at all, the “26-neighborhood.” For the sake of simplicity and to avoid breaking connectivity, we would like to consider a maximalist definition and hence the 26-neighborhood [28].

We run into an issue, however, when we attempt to apply our basic mathematical intuition to bear on these structures. For the purposes of illustration, we will use two-dimensional examples. The same considerations apply in three dimensions as well. Assuming the use of an “8-neighborhood,” consider, as in Figure 6.2, a closed curve that separates an outside from an inside. We desire that a string of connected “on” pixels would divide the “off” pixels into an interior and an exterior. However, if the curve consists of pixels connected along a diagonal, both the “on” pixels are connected along

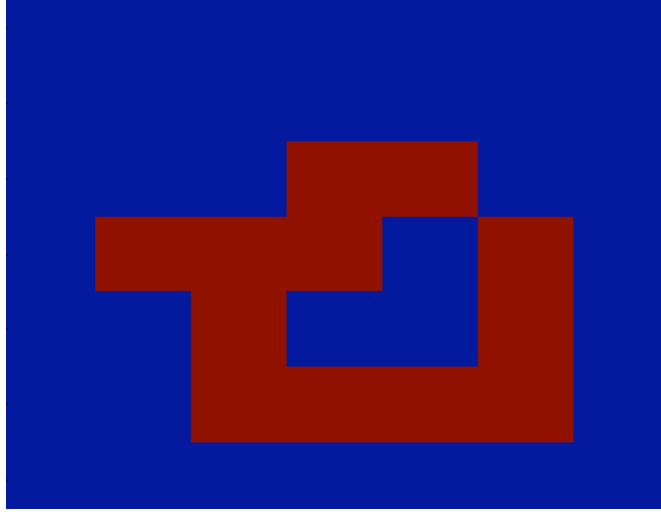


Figure 6.2. Illustration of the Jordan Curve Lemma in two-dimensional digital topology. Red pixels are considered “on” and blue pixels are considered “off.” Depending on the choice of connectivity (4 or 8), both the blue and the red pixels can either connect diagonally on the right side of the figure. The associated topological problems with choosing the same connectivity for both “on” and “off” pixels compel one to choose a different connectivity for foreground and background.

the curve, and the “off” pixels are connected perpendicular to it. This violates the Jordan Curve lemma and suggests that universal 8-connectivity is not a proper topology to use. Similarly, if we use the 4-neighborhood, we would have a set of “on” islands that somehow manage to divide two regions of “off” pixels. That is, an unconnected curve would divide inside from out, again yielding a contradiction to the Jordan Curve lemma [28].

The inherent issue is that in two dimensions, 4- and 8- connectivity are dual. If we choose the “on” pixels to be 8-connected, then we must choose 4-connectivity for the background and vice versa. Then and only then are we able to satisfy the basic constraints of topology. In the example, if “on” is 8-connected, the curve is a connected loop and divides inside from out. If it is “4-connected,” the curve is a U-shape, not a loop, and does not divide the background. In three dimensions, this duality relation becomes one between 6- and 26-connectivity. This can be seen by projecting a three-dimensional loop into two dimensions. 18-connectivity is not self dual (as can also be seen by projection) and is effectively a mathematical curiosity [28]. We chose our “on” pixels to be 26-connected and our “off” ones to be 6-connected.

Having defined a grid, we now have to perform topology on it. In general, we would like to isolate a skeleton homeomorphic to the original image. Homeomorphism corresponds to the cartoon view of topology held by many: it considers those properties of shapes that are invariant under continuous transformations e.g. shrinking, expanding, stretching, and bending of objects, that is,

anything but tearing and gluing. A pure, single voxel thick skeleton would be homeomorphic to the original image. Unfortunately, there is no general method for calculating homeomorphism. We need to consider other, less exclusive forms of topological equivalence [38].

A more general property is homotopy equivalence, which can be thought of as homeomorphism plus deformation retraction. That is, we allow extended objects to be retracted down to a single point if the map and its inverse are continuous. Trees can be shrunk to (nearly) nothingness, but loops cannot. Modulo homotopy equivalence, we can characterize structures algebraically through what are known as the homotopy groups, π_i . These groups π_i represent the mappings of the sphere of dimension i , S^i , to the object in question. The zeroth homology group, π_0 represents the mappings of points, measuring the number of connected components. The most important homotopy group is π_1 , the fundamental group, which describes how loops “fit” into the object. Unfortunately, calculation of the fundamental group is not trivial, leading us to look for a new strategy [38].

The abelianization² of the fundamental group gives us the first homology group, H_1 . The higher homology groups in our case correspond to the homotopy groups (up to and including H_3). In general, the homology groups represent the interaction of boundary operator with a properly defined scaffold of the object in i dimensions. These groups can be calculated algebraically and form the basis of our algorithm [38].

The coincidence of nearly all of our homology groups with the homotopy groups, i.e. $H_i = \pi_i | i \neq 1$, suggests that we should attempt to corral the fundamental group into this paradigm. We know that the rank, or the number of generators, of H_1 and π_1 is the same. Hence, if the rank of H_1 doesn’t change when a voxel is turned “off”, all we need to worry about is whether the way these generators combine changes. The key here is that the removal of a voxel changes the structure of the overall object locally. There is simply no way that if the number of generators does not, the relations between them will from the removal of one pixel³. It is the number of generators that matters, not the internal structure of the group, due to the local nature of the pixel removal. Given this knowledge, we can create an algorithm to perform homotopic thinning [38].

²Making commutative. For instance, the fundamental group of a figure eight is the free product of the generators of the two loops (or lobes) of the figure eight. The first Homology group is the direct product of these generators.

³Returning to the example of the figure eight, if the number of generators does not change that is we preserve the two lobes, removing a pixel (if the edges of it are “thick”) won’t change how these two generators interact. It will still be a free product.

6.3 Homotopic Thinning

The Betti numbers, $\beta_0, \beta_1, \dots, \beta_d$ are the ranks of the homology groups. They are topological invariants. If they do not change during a voxel removal, neither does the topology of the image. Our image is three dimensional, cavity free, and embedded in Euclidean space. Hence, β_3 is trivially zero: we can have no three-dimensional holes. The zeroth and second homology groups are nearly as easy to calculate. H_0 represents the number of connected components in the object. As long as we do not disconnect any two regions of our image, when removing a voxel, β_0 is guaranteed not to change. We may easily test this criterion with a FLOODFILL before and after removal. Moving up one dimension, β_1 is not simple to calculate, as it counts the two-dimensional loops in the object, which is three dimensional. These loops may be pointed every which way and at any angle. Calculating it directly is extremely difficult. H_2 represents the number of two-dimensional holes, or cativites, in the image [38]. This too is easily calculable. We started with no cavities (see §5.4 above) and desire to drill no new ones. Hence, we only remove border points, that is, points that have a 6-neighbor that is “off.” Any pixel turned “off” is then already adjacent to the background, and no cavity is formed.

We are still left with determining whether or not H_1 changes. We are aided here by the Euler Characteristic, χ , which is defined as $\chi = \sum_{i=0}^d (-1)^i \beta_i$, the alternating sum of the Betti numbers. This is not the only way to calculate the Euler characteristic, however. On graphs, it is the number of faces (F), minus the number of edges (E), plus the number of vertices (V). In three dimensions, we need only to subtract an additional term for the number of complete cubes, which we will denote O [30]. Collecting terms:

$$\Delta\chi = \Delta\beta_0 + \Delta\beta_1 + \Delta\beta_2 \tag{6.1}$$

$$= -\Delta O + \Delta F - \Delta E + \Delta V \tag{6.2}$$

Exploiting that $\Delta\beta_0 = 0$ and $\Delta\beta_2 = 0$:

$$\Delta\beta_1 = -\Delta O + \Delta F - \Delta E + \Delta V \tag{6.3}$$

We now have a relation for β_1 that may be exploited, enabling us to return to the $3 \times 3 \times 3$ cubes of §6.1. One might worry that by looking only locally, we ignore the global nature of topological properties. This, however, is not an issue. We can consider properties in dimensional order as before.

Clearly, the number of connected components cannot change globally if it does not change locally: a narrow bridge between two regions will appear to be a narrow bridge, admittedly connecting “thinner” regions, on the local scale. There are two ways in which loops may appear: they can be local and seen by the algorithm within a $3 \times 3 \times 3$ cube, or they may be substantially larger: imagine an extended three-dimensional loop of inner diameter 25 voxels and outer diameter 30 voxels. Our algorithm has no way of “seeing” this loop. However, as it thins the outside of the loop, it will approach a point where all it sees is a narrow bridge, that is, the loop will have shrunk to an outer diameter of 26 voxels. At that point, removing a voxel and breaking the loop will be prohibited, because it would generate two disconnected components. As for cavities, a similar argument applies. Local cavities are easily prevented. Global cavities will be seen as something resembling a flat plane inside one of our $3 \times 3 \times 3$ cubes, comprising a section of its wall. If we were to remove the center pixel of this wall, we would create a loop, which is clearly prohibited. Local topological invariance thus implies global topological invariance in our case.

If we were forced to calculate the Euler Characteristic for all 2^{26} cases according to the above formula, we would not have saved ourselves much trouble. Instead, we can make use of one final property: the Euler Characteristic is additive. If we properly weight faces, edges, vertices, and cubes by the number of pieces shared between them, we may calculate the Euler Characteristic by summing over these pieces instead of all at once. Our task is now simple: we calculate the change in χ for each $2 \times 2 \times 2$ octant, whence O in the formula, in our cube and sum over all of them. We may even go one step further and look at the change in χ in each octant so that only one summation is necessary. This reduces the number of cases in our octant look-up table to $2^7 = 128$, since one cube is always the one to be removed, enabling us to calculate $\Delta\chi$ analytically and hardcode the values into our software. The paper by Lee et al. [29] also includes a table of these values, further simplifying the task.

Since our algorithm only considers homotopy, our skeleton will be topologically equivalent to our original image modulo deformation retraction. Any branch or treelike set of branches will not be preserved, as they are homotopy equivalent to a point. As our dataset consists of a series of branched tubes, we can correct for this. We manually mark the 26 cases where the center pixel is on along with one other pixel as nonremovable. This procedure will preserve branching tubes once they are reduced to one voxel in thickness, which we term “strings.” These tubes will inevitably be shortened as their width is reduced. As long as the most peripheral vessels are at least one voxel longer than their radius, they will be preserved with the proper radius⁴ but with an underestimate of its length.

⁴defined as a maximum over the vessel

All vessels downstream of these after the first merger will be properly preserved. We have only to worry about the case of vessels whose length is equal to or less than their radius. For these, it is not clear whether they constitute proper vessels in the first place or are simply irregularities on the surface of another larger vessel. The vast majority of our vessels are also substantially longer than they are wide and are less than 10 voxels in radius (see §8.1 for details).

With the above algorithm, we can generate a look-up table for each of the 2^{26} cases. We are not done, however. If we naïvely iterate over all points, hash their region, and decide whether or not the center voxel can be removed, we end up with disconnected, meaningless fuzz. A simple example will suffice: consider a region consisting of a $2 \times N \times 1$ set of pixels, perhaps connecting two broader regions. When approached from the $+x$ direction, we see we may remove the entire row. The algorithm sees the full width, two pixels, of the region, so removing any one of them is no problem. The mirror image situation is seen from the $-x$ direction. Hence, when we raster through the image and remove all the voxels, we will have deleted the entire region. Clearly, this is unacceptable. Removing one pixel changes the context of its neighbors.

An obvious solution is to go through and remove points immediately if they are simple. While correcting for the prior issue, this method will not give us the skeleton we expect. Rather, we will see artifacts from the removal process. Imagine moving through the image iteratively, first down rows in x , then columns in y , then planes in z . If we encounter a thick tube, extended, say, in the y direction, we will remove planes of constant z until it is only one voxel thick in z . We will continue removing pixels in the x direction. Our skeleton of this vessel will consist of a line of voxels on the edge of the tube, perpendicular to its circumference. While this is topologically correct, it renders our distance transform meaningless, as we will get a value of 1 no matter the width of the tube. While topologically incorrect, the skeleton would not even be approximately geometrically correct. Any program for iterating through the image will yield artifacts, some of which can be dramatically more dangerous. If we remove points in a Monte Carlo fashion, we will almost definitely create unphysical branching structures on our skeleton. Statistically, we will drill holes into thick tubes. If the hole were to turn, or to reach until the vessel were one voxel thick, we would create a new treelike feature during skeletonization, which would pose a problem if we were preserving “strings.” Even if we were not, the skeleton of a tube would follow a random walk, complicating all measures of its length and radius.

The solution is to only remove one layer of points at a time, akin to peeling an onion. We keep two copies of the partial skeleton in memory (\mathcal{I} and \mathcal{J}). During each pass, we examine points to make sure that they are border points on one copy (\mathcal{I}). If they are, we move to the second copy

where we hash the $3 \times 3 \times 3$ cube of the point and its neighbors and remove them if removable (\mathcal{J}). After examining every “on” point, we copy \mathcal{J} to \mathcal{I} and restart the process. The first copy ensures that we are removing only a single layer at a time. The second has updated context so that we do not remove features of an even-numbered width. The process is complete once no points are removed during a pass.

This algorithm is slow, as only one layer of points can be removed at once and every “on” point must be iterated over. It may be parallelized; the alteration of local context of one point by the removal of its neighbors limits its effectiveness, however. To divide the image up into sectors, where no $3 \times 3 \times 3$ cubes overlap such that the removal of the central points does not affect the next cube requires that we have eight separate subpasses. We may consider a point simultaneously with a point two units away in any direction. While their $3 \times 3 \times 3$ cubes will share a plane, the central point of one will not appear in its neighbors’ and vice versa. Since the structure is three dimensional, we have $2^3 = 8$ separate cases. The image is hence divided into subregions, depending on whether its x , y , and z coordinates are odd or even. Within any subregion, we may parallelize, considering points independently. At the end of each pass, the partial skeleton is reassembled, and the next octant is considered.

Skeletonization must be performed on the largest connected component of the image, otherwise the result will be disconnected subskeletons. These artifacts may be removed afterwards, via a FLOODFILL, but will slow skeletonization. It is worth considering what would have happened had we used the dual, 6-connectivity, for our “on” pixels. We chose 26-connectivity to adjust for the limited resolution of the optics; we expected there to be connected features that only linked up diagonally, due to the limited, $5 \mu\text{m}$ optical resolution. With better optics, we could see how a “6-skeleton” differed from its 26 counterpart (hopefully not at all).

Chapter 7

From Skeleton to Graph

Confronted with a skeleton of the original dataset, it is still not obvious how to proceed. While the skeleton has dramatically fewer points, 4.5 million or 14.5 million depending on whether we chose to preserve “strings” instead of 973 million, we are still faced with the task of intuiting the structure and ordering of millions of cubes in space, each of which has a characteristic distance from the edge, given by the distance transform. What must be done is to extract a mathematical graph, that is a set of nodes and edges joining them, from the smaller collection of cubes. This structure will readily lend itself to analysis and visualization, allowing us, for the first time, to see the data extracted. We analyzed the data in two forms: with and without string preservation. In the former, there are no strings, only loops and the treelike components that connect these loops, what we might term the “topological core” of the network.

7.1 Finding Your Neighbors

The first step is to take the dual of the structure of cubes: to turn shared faces into connections and full cubes into points, or, in short, to find one’s neighbors. Just as in the skeletonization routine, we may hardcode vectors giving the relative coördinates of the 26-neighborhood and iterate over all pixels. This time, however, we capture the location of all neighboring points and formulate an adjacency list, storing the neighbors of each point in the skeleton. It is convenient to arbitrarily label all the points in the skeleton and store their coördinates in a hash table for reasons of speed and memory.

Looking at the spectrum of node degree, we find that 93% of nodes have two neighbors, indicating they are part of lines in the skeleton or vessels (not junctions) in the original dataset. The remaining

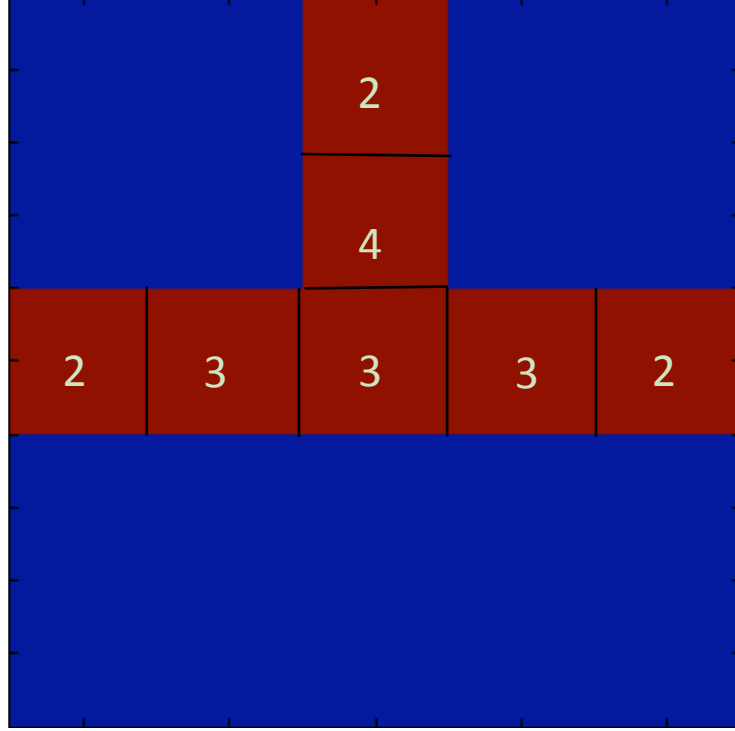


Figure 7.1. Anomalies in the definition of vertices within the graph extracted from the skeleton of the dataset. The skeleton is shown in red with the degree of each node written inside in yellow. At a triple junction in two dimensions, four separate points can lay claim to being a vertex, three of which have the expected connectivity of three, but one of which has degree four!

nodes would then correspond to vertices. Nearly all of them are three-connected, as one would expect for vertices in natural vasculature. There are a nontrivial number, however, of nodes of higher degree: nearly 11000 of degree four and handful of degree five and six. Similarly, many of these supposed “vertices” were adjacent to another “vertex.” Intuitively, these situations should not exist and made us question the procedure for turning the skeleton into a graph.

We began to investigate these anomalous situations, examining the direct connections between vertices and the points of suspiciously large degree. These vertex agglomerations occur at essentially every intersection. A simple example of why can be seen in Figure 7.1. At a flat (two-dimensional) triple junction, there are three three-connected nodes and one four-connected one. If even the simplest triple junctions have anomalous connectivity, the problem is a general one. It is complicated further by the presence of a third dimension. If one images moving the vertical line in 7.1 up and out of the page and then rotating it towards the viewer, a situation can be generated in which a triple junction has only one three-connected “vertex.”

The third dimension may hinder as well as help. If we imagine two nearby triple junctions, separated by a unit in the horizontal, x , and out of the page, z directions, there will be points

between them that have connectivity as high as five or six, despite there being two distinct vessel intersections. On some level, these issues are due to the limits of the resolution of our optical system. The smallest vessels we capture, themselves only two pixels in diameter, may only be two pixels from the nearest vessel. On another level, these problems are purely statistical. With 253,000 lines, we are bound to have some number of arbitrarily close triple junctions.

7.2 Vertex Simplification, Edges, and Lines

It is tempting to believe that these cliques of “vertices” can be found in a purely topological manner. We can construct an adjacency matrix of “vertices” that impinge upon one another and look for cycles between them. If we remove one connection from every cycle, then repeat the process, ideally we would be able to reduce these cliques to one multiply connected node, chosen at random, to be the true vertex.

In the simplest case, cycles of length three, this procedure works well. We take our adjacency matrix of impinging “vertices”, \mathcal{A} , and raise it to the third power. The elements of the trace, $\text{Tr}[\mathcal{A}^3]$, are cycles of length three. Since each of three nodes in the cycle will be represented in the trace, we must not consider every such element. Rather, we go in order and once a node is considered, every other node it borders is not considered. This procedure is overly conservative, as a single node may be part of multiple triangles, such as the four-connected node in Figure 7.1 above. It may be run multiple times in a row, however, until no more triangles are found. In practice, nearly all the triangles ($> \frac{3}{4}$) are removed in the first pass. Altogether, slightly over 75000 triangles are removed, contributing 52% of the removal of the vertex candidates.

Extending this method to cycles of length four yields a problem. Cycles of length four do not have to be quadrangles in the graph, unlike those of length three that are always triangles. A cycle of length four may simply be the sum of two different cycles of length two, or even the same cycle with itself. Mathematically speaking, we are taking direct sums over the graph, \mathcal{G} , with itself and looking for identity elements:

$$\mathcal{G} \oplus \mathcal{G} \oplus \mathcal{G} \oplus \mathcal{G} = \mathbb{1} \quad (7.1)$$

If we only have three copies of \mathcal{G} , there is no subdivision of the sum that will give use two elements that each equal the identity. In the case above with four elements, however, we can have $\mathcal{G} \oplus \mathcal{G} = \mathbb{1}$. If so, $\mathbb{1} \oplus \mathbb{1} = \mathbb{1}$, giving us trivial solutions and meaningless cycles of length four. If we

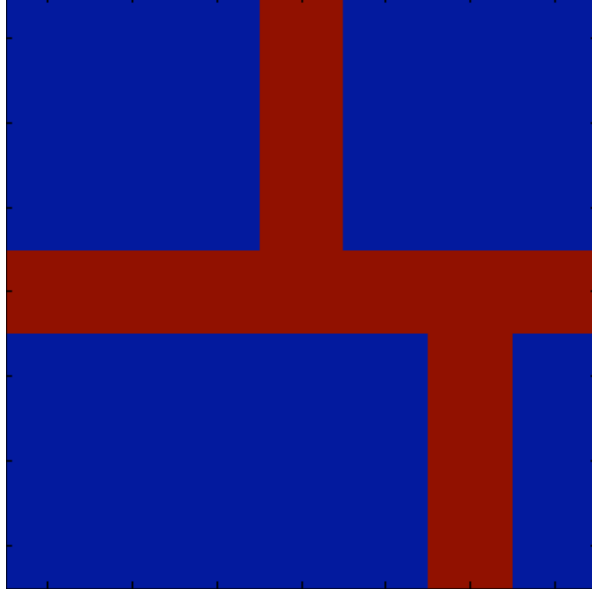


Figure 7.2. Two nearby triple junctions can create a situation wherein two properly construed vertices cannot be extracted. Instead, using our vertex clique reduction algorithm (see text), all nearby multiply connected nodes are combined into one, new vertex point, with coördinates equal to their mean.

were working with a regular lattice, this problem would disappear, as we could precisely calculate the number of cycles of each length and then extract them from the trace. Then again, in that regime, there is no need to solve the problem, as the underlying graph structure is known.

After removing the triangles, we must simply rely on an ad-hoc method to turn clumps of vertices into a single, unphysical vertex. For instance, if we have the situation displayed in Figure 7.2, two nearby intersections cannot be properly separated. We cannot topologically isolate the two intersections from the adjacency matrix of the the candidate “vertices.” To rectify this situation, we take the clump of impinging “vertices,” isolated by a simple FLOODFILL on the adjacency matrix, and create a new vertex out of it. Its coördinates are taken to be the mean of those of its component members. It is connected to the same points as its members. It is given a “radius” to represent the distance to the edges of its component members, to ensure that the proper lengths will be collected. While this solution is somewhat inelegant and creates new vertices of high degree, they are rarer than before (there are 16 of degree 5 and 2520 of degree 4): 1.4% of total vertices versus 3.5% before clique removal.

Once we have isolated the vertices, we may go through and combine two-connected points into the edges of the graph. Computationally, this is a simple procedure: extract the two connected points, choose one at random, move in both directions until one hits a vertex, label those vertices the end

points, and store the collection of two-connected points as a line with a specific hash key. When repeated over all of the remaining two-connected points, we should be able to form an adjacency matrix with entries corresponding to each edge of the graph. In the case of a string-preserving network, we also label the one-connected points as vertices (there is no ambiguity in defining them). Edges that lead nowhere and end will then be accounted for.

While simple in theory, this algorithm fails to account for the structure of our network. When we isolated the “topological core” of the skeleton, we left only components belonging to loops or connecting them. Hence a small loop, with “strings” hanging off of it is reduced to a loop at the end of the vessel(s) that connected it to the rest of the network e.g. in the shape of a noose. If only one vessel did so, we would form an edge that is looped but only has one endpoint. If there are two, we would find multigraph edges, multiple edges that connect the same pair of vertices. These features may appear even without string removal. There is no reason to presume that small loops do not exist within the hierarchical vasculature whose purpose we cannot ascertain because we have not yet mapped the capillaries. Our knowledge of the vasculature of leaves should give a strong prior to expect loopy features on all scales (see §8.2). Rather than dealing with multigraph edges and loops at the ends of vessels as an anomaly, we should expect them to be omnipresent. Their existence is a strong argument for attempting preserve strings, which we expect to turn multigraph edge pairs into loops spanning several vertices.

For each edge we identify in the network, we store the original voxels that comprise it, its endpoints, and its radius. From the voxels, we can extract the path that it follows as well as the distance transform value for each point in it. To assign a radius to the vessel, we take the maximum value of the distance transform along the segment. The maximum could potentially be somewhat corrupted by artificially high values near the junction of a small vessel at a larger one if the skeleton of the smaller vessel includes some points physically insides the larger ones. However, if at any point the skeleton is not precisely in the center of the vessel, the distance transform will be unphysically small, dragging the mean down. Similarly, if we desire to select lines only of a certain radius or larger, we are, on some level, creating a surrogate dataset mimicking the effect of imaging with optics of a set, worse resolution. These optics would be able to detect vessels that hovered around the resolution limit if sections of them were wide enough to be clearly detected, due to our use of morphological closing. The use of a maximum over the distance transform hence mimics our approach during segmentation.

When computing network statistics, we may select edges only of a certain radius (or radii) or certain length(s). With the lines that obey that criterion selected, we determine which vertices are

in the network by including only those that are endpoints of the selected lines. The number of connected components may be determined from a FLOODFILL on the graph. In this manner, we extract all the relevant graph properties for a set criterion, allowing us to see what our structures look like when only vessels of a certain radius or larger are included.

7.3 Visualization

Visualization still provides the largest technological difficulties in this effort. As mentioned previously, the original image, with 973 million “on” voxels and 19 billion voxels total, there is simply no way for the data to be displayed. After skeletonization, while the volume of data has been reduced by 50 to 200 times, depending on string preservation, there are still too many individual voxels to be easily displayed, not to mention that with single voxel thick lines, the resulting image would be nearly meaningless. Coarse-graining the skeleton would be even more counterproductive than coarse-graining the original dataset (see §6). With the reduction to a graph, we finally have a compressed form of the data, consisting of connections and their respective radii, that can be more easily displayed.

This, too, is easier said than done. We have over 250000 edges in the topological core and about eight times that number in the string-preserved skeleton. Each edge must be rendered as a separate cylinder. The total number of object handles necessary proves to be too much for nearly all general-purpose imaging software. We have had some success coding our dataset directly into a three-dimensional viewing language, such as VRML or its successor X3D, and viewing the results with more specialized software. Since both languages are written in ASCII, a MATLAB function can be written that, after defining object types in the header, goes through the list of edges and adds a new object to the image file for each. By defining all of the vessels as transformed instances of one original cylinder, we greatly save on memory and can display the entire dataset. Each cylinder must be scaled to the proper length and radius, translated to the mean of its endpoints, and rotated to align with the vector of its endpoints. This last step is the trickiest: finding the principle axis of rotation and the angle rotated around it from the endpoints. We must first take the vector between the endpoints and find its direction. This is interpreted as the combination of a rotation about the x axis (setting θ), followed by one about the z axis (setting ϕ). Only two rotations are needed because of the radial symmetry of the cylinder. These two rotations $R_x(\theta)$ and $R_z(\phi)$ are multiplied to give a total rotation matrix, R . This matrix must be diagonalized to find the rotation axis, given by the principle eigenvector, and the angle about that axis, given by $\arccos \frac{1}{2}(\text{Tr } R - 1)$. An image of our

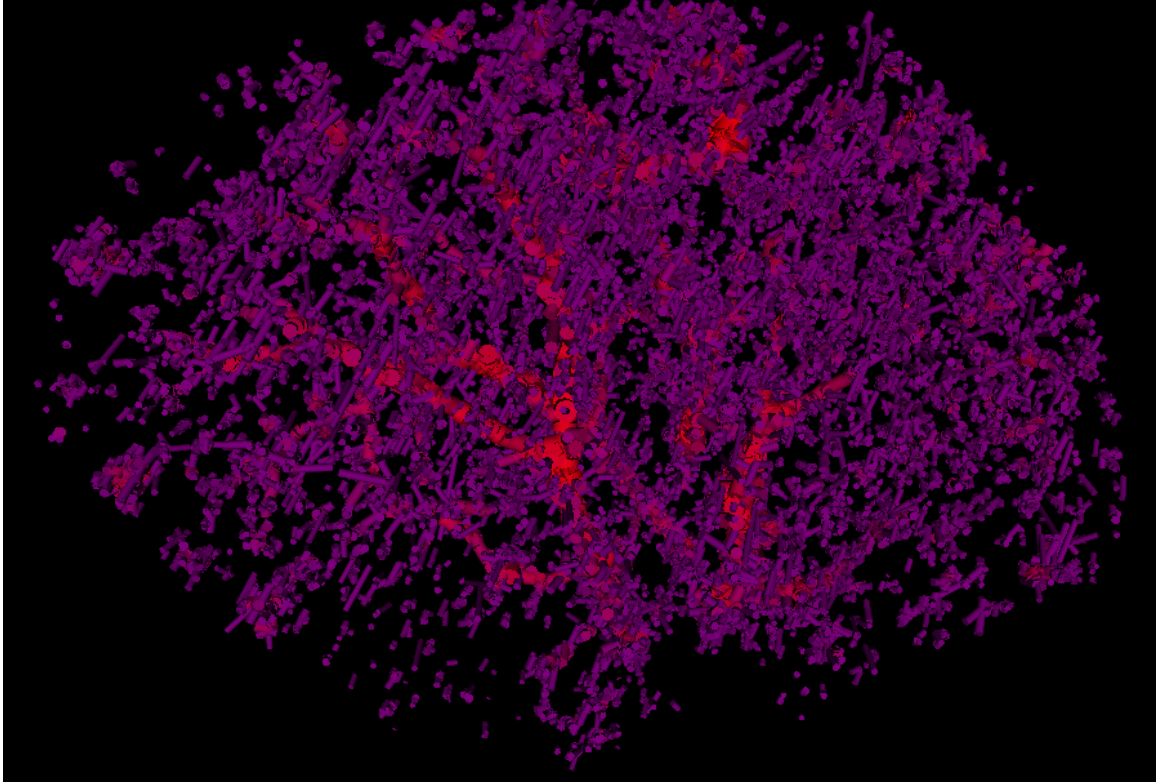


Figure 7.3. The Largest Vessels in the Our Dataset. Shown here is a screenshot from the VRML 3d image of our dataset (see text). Displayed are only those vessels of radius 10 pixels (50 μm) or greater (around 1% of the data). Vessels are color coded according to their width, with the largest ones in red and progressively thinner ones darkening to purple. Note the large tree corresponding to the portal triad and the way that its branches fill the space of the tissue. While scattered disconnections are seen, these should not be troubling: 10 pixels is an arbitrary cutoff: any noise in vessel radii or slight thinnings of anastomoses will lead to disconnections when sectioning the data in this manner.

dataset containing only the largest 1% of vessels is shown in Figure 7.3.

There are a few caveats to this approach. Only certain properties may be transformed in VRML: position, direction, and scale. While we can place, orient, and size each vessel correctly, we cannot easily change its color to correspond to its radius. Every vessel colored differently requires an instance of either a new object type or a one-off object. Either way, the computational load increases. In the diagrams, we have tended to color the smallest vessels all the same (blue), the medium size vessels a different color (purple), and the largest vessels a shade of red corresponding to their radius, as there are not many of them. Since we define every vessel to be some form of stretched cylinder, we are unable to use the actual paths of the vessels, which are considerably more tortuous. This problem is especially apparent with the multigraph edges, which define a loop, but in our visualization procedure, they are concentric.

Ultimately, the sheer number and density of vessels makes looking into the three-dimensional

image nearly impossible. We have come full circle and returned to our inability to image corrosion casts, as we cannot see inside of them. Imaging software allows us to rotate the object in three dimensions and to fly into it. Comprehending it is another problem entirely. Our best successes have come from only looking at small fractions of the dataset: plotting the data for vessels larger than a certain radius. With a minimum radius of 10 voxels ($50\text{ }\mu\text{m}$), we have only a couple thousand vessels and can see how an initially treelike structure branches into a heavily looped, space-filling one, as in Figure 7.3.

Chapter 8

Analysis

Faced with comprehending a graph composed of over two million edges and nearly as many vertices, we are forced into the realm of statistics. There exists no good way to comprehend this structure, even when only a small subset of the vessels, such as those of radius $50\text{ }\mu\text{m}$, are included. What statistical properties are meaningful, however, and what can they tell us about the structure of the network? How can we understand the hierarchy of the vessels? These are the questions we are just beginning to answer. The analysis of loopy, hierarchical distribution networks is young; in the case of nonplanar networks, it is even younger. We are just beginning to peer into these structures: in many cases we simply do not know the right questions to ask. With that caveat, however, we have examined several basic geometrical properties, such as vessel radius and length, and topological ones, the numbers of graph theoretical components. Taken together, we can examine the scale on which the loops occur: a first estimate of the kind of unified geometrical and topological analysis we hope someday to perform.

While it is seductive to believe that we can separate arteries from veins, given our imaging procedure, we are able only to identify vessels, not their lining. We suspect that the portal triad is frequently identified as one vessel, with morphological closing connecting the large portal vein to the substantially smaller hepatic artery next to it. On smaller scales within the liver, schematics frequently indicate the mixing of blood between these two vessels, once they feed into the sinusoids. Given the frequency of arteriovenous anastomoses throughout the body (see §2.1), this crossover should be expected. Similarly, we do not identify separate portal triad and hepatic venous networks. There is only one large connected component in the skeleton. We expect arteriovenous anastomoses to be frequent enough to prevent any easy identification of separate vascular networks.

8.1 Geometrical Properties: Vessel Radius and Length

While simple models of distribution networks do not include loops, they do make predictions about what the distribution of segment radii should look like. Since our data lack a natural method for defining a hierarchy of segments, we will invert and equate the relations based around hierarchical order to extract predictions for the distribution of vessel radii and length. In the simplest case, imagine a binary tree, where vessels travel a distance l and then bifurcate into two vessels, each of which has radius $d_{i+1}/d_i = \frac{1}{\sqrt{2}}$ smaller than its mother vessel to conserve volume. Continuing this process, the number of vessels of order i increases exponentially, and the radius of the vessels decreases exponentially. Hence, the number of vessels of a certain radius, $n(r)$ obeys a power-law relation. This a reflection of volume conservation: if we only demand that the total volume in each order is constant, $v_i = v_{i+1} = c$, then $v_i = l d_i^2 n_i = c$ and $n_i \propto 1/d_i^2$, giving a power-law distribution.

More generally, we can consider a system parametrized by Strahler stream ordering and obeying Horton's Laws, such as the Scheidegger Model. Here, we allow irregularities in the branching pattern and do not demand volume conservation at each junction. The number of vessels of order i scales geometrically: $n_{i+1}/n_i = r_n$ and the radius of each vessel scales similarly $d_i/d_{i+1} = r_d$. This second relation is not strictly one of Horton's Laws, rather the area drained scales with the order [49]. If we assume constant flow per area drained, we get a scaling relation for the radius:

$$v_{i+1}/v_i = a_{i+1}/a_i = 1/r_a \quad (8.1)$$

$$= \frac{l_{i+1} d_{i+1}^2}{l_i d_i^2} \quad (8.2)$$

$$d_{i+1}/d_i = \sqrt{\frac{r_l}{r_a}} = 1/r_d \quad (8.3)$$

In the last step, the length ratio $l_{i+1}/l_i = r_l$ was substituted. To find $n(d)$ we must invert the relationship for the number of vessels of diameter i . Since the geometrical scaling implies an exponential functional form, i.e. $d_i = a r_d^{-i}$ where a is an arbitrary constant, inverting this gives $i = -\log \frac{d}{a} / \log r_d$. Substituting into the the functional form for the number distribution we get:

$$n_i = b r_n^i = b e^{\log r_n i} \quad (8.4)$$

$$= b e^{\log r_n \log \frac{d}{a} / \log r_d} \quad (8.5)$$

$$= c d^{\frac{\log r_n}{\log r_d}} | \log r_d = \frac{1}{2} (\log r_a - \log r_l) \quad (8.6)$$

where c is a new constant dependent on a and b to various powers. This relationship is clearly a

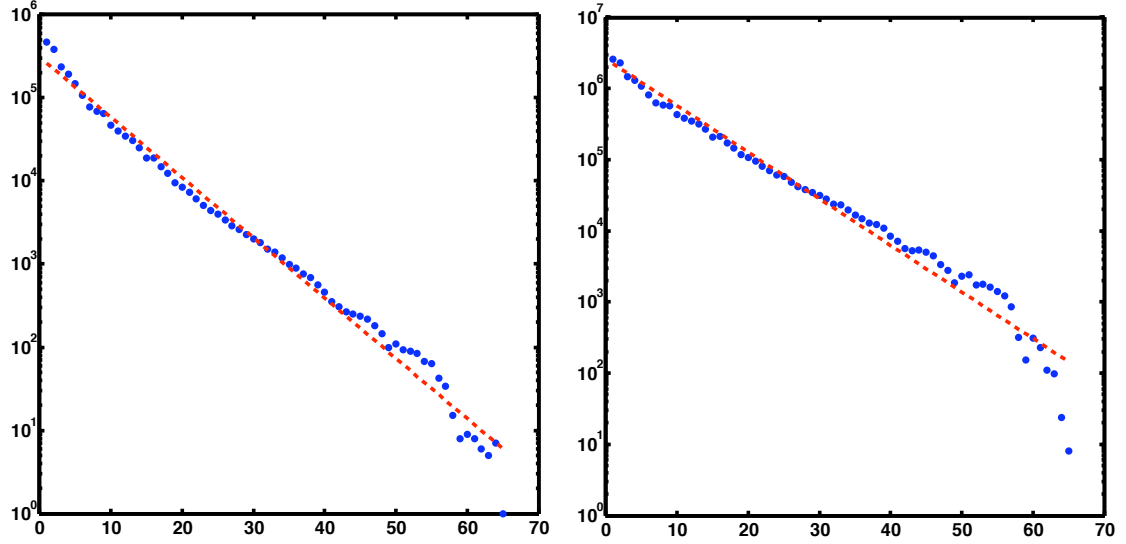


Figure 8.1. Histograms of the vessel radii. Left: number of vessels versus radius with each vessel counted once. Right: number of vessels versus radius with each individual pixel in a vessel counted once (length weighted). In both, radii are in pixels, and the y-axis is logarithmic. Data are the blue dots, and log-linear fit is shown by the red dashed line. On the left, the decay constant is 6 pixels, or $30\text{ }\mu\text{m}$, $r^2 = 0.98$. On the right, the decay constant is 6.6 pixels, or $33\text{ }\mu\text{m}$, $r^2 = 0.96$, artificially brought down by the cutoff on the right.

power law with exponent determined by the how the volume is distributed between the number and length of vessels and of the area drained by each vessel. A similar but simpler relation holds for the histogram of vessel lengths. If $l_i = r_i^{-i}$, $n(l) = l^{\frac{\log r_n}{\log r_l}}$, another power-law relation.

A power-law relation, however, is not what we see when we plot the empirical radius histograms, as shown in Figure 8.1. We provide two different ways of calculating the radius histogram, counting each vessel once (left) and weighting by vessel length (right). In each case, the plot is nearly perfectly linear on semilogarithmic axes, indicating an exponential relationship. While the decay constant varies slightly, from $30 \pm 1\text{ }\mu\text{m}$ to $33 \pm 1.5\text{ }\mu\text{m}$, this could be entirely due to the length weighting inducing a slight shift in the data.

The lack of difference in functional form between these two figures suggests the robustness of our findings. Segments are typically defined between points where their Strahler order changes. Lacking a hierarchy, we subdivide large vessels into many smaller segments, counting intersections with less

important vessels. To correct for this bias, if we weight by length, we find:

$$l(d)n(d) = l(i(d))d^{-r_d} \quad (8.7)$$

$$= l(-\log(d)/\log(r_d))d^{-r_d} \quad (8.8)$$

$$= r_l^{-\log(d)/\log(r_d)}d^{-r_d} \quad (8.9)$$

$$= d^{\frac{\log r_l}{\log r_d} - r_d} \quad (8.10)$$

This relation, too, is power law. While the exponents may be simplified, by substituting in equation 8.6 above, this is unnecessary.

Examining the histogram of vessel lengths, Figure 8.2, we see a more complicated, but still non-power-law relation (right panel). It appears there exist two regimes in the vessel length data: one for the shortest vessels, with a high decay constant, and one for the longer vessels, with a somewhat smaller decay constant. The fit, shown in red, seems to pick up more of the latter, slower decay than the former. As skeletonization will shorten the most peripheral vessels while thinning them, we expect an overabundance of short vessels. The second regime may be nothing more than an artifact, giving a purely exponential distribution. Similarly, the deviation from the fit at high length may be due to our inability to calculate a proper hierarchy for the network. Traditionally, segments have length defined by the distance between points where their Strahler order changes. We are counting the distance between all intersections. This will systematically underweight the lengths of the largest, thickest vessels. While the skeletonization procedure will reduce the lengths of “strings,” that is vessels that have a one-connected vertex as an endpoint, if we discard the “strings,” we find the same pattern for the length histogram, indicating a robust pattern.

The lack of power-law scaling in both the radius and length histograms indicates a severe difference between vascular networks, with loops on all scales (see §8.2) and treelike distribution networks. The derivations above demonstrate that power-law scaling for number of segments of radius r and length l is universal for treelike models and reflective of their internal structure. Our observation of exponential scaling puts into stark terms the changes wrought by looped morphology and implies that analogies to topologically simpler systems are not only a simplification but also incorrect. The loops are not a “decoration” on an internal treelike structure: they are fundamental to it.

One might interject, though, that the failure to observe power-law scaling is evidence is of a failure in our imagine our analysis procedures. That is, we simply are not capturing all the vessels or calculating their properties accurately. This seems unlikely. There is no signature of power-law

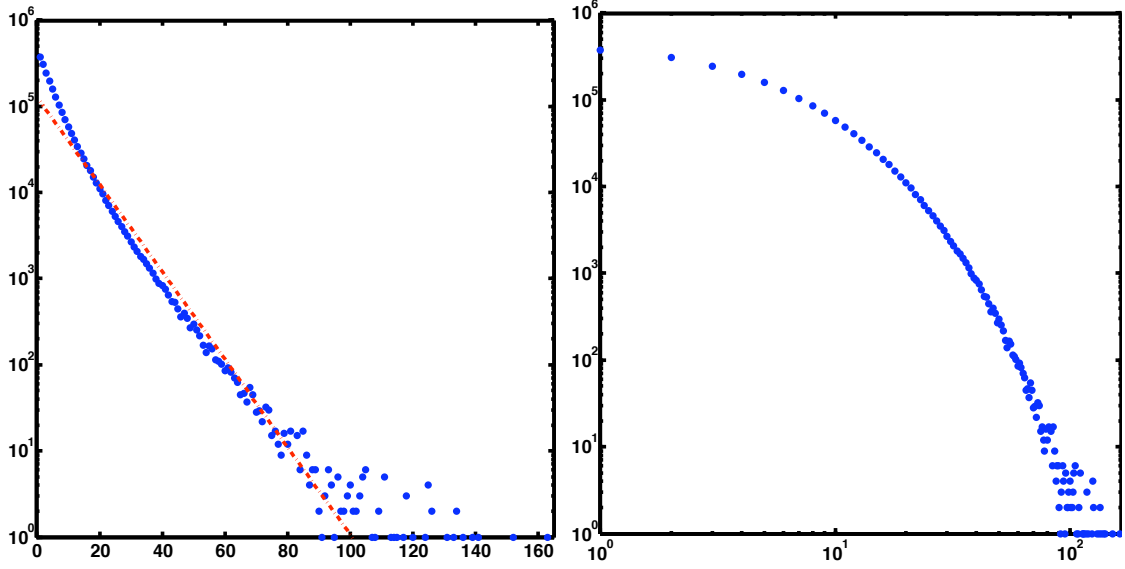


Figure 8.2. Histograms of the vessel length. Left: number of vessels versus length with each vessel counted once on semilogarithmic axes, data in blue circle. Right: the same relationship on fully logarithmic axes. From the right panel, it is clear the relationship is not a power law, though the fit, shown in red on the left hand panel, is clearly insufficient. The decay constant of the fit is 8.5 pixels or 43 μm ; $r^2 = 0.98$, even for this poor fit.

behavior in either the small vessel or the large vessel regimes. We see neither a cutoff or some kind of finite size effect truncating power-law scaling. If we are making an error, it is systematic. In that case, the error process must have statistics equivalent to an exponential minus (or divided by) a power-law. This, too, seems highly unlikely. The empirical evidence implies length scales in both the distributions of vessel radii and vessel lengths. The assumption, then, that vascular networks are fractal is contradicted by the empirical evidence, at least in the case of the hierarchical vasculature of the liver.

8.2 Topological Properties: Loops and Network Structures

How can we count the number of loops present in a network too large to comprehend mentally? At first, this task seems impossible: for instance, in Figure 8.3, the smallest loops, such as the triangles on the right-hand side, are contained within larger loops, e.g. the combination of two or three of those triangles, all of which are contained within the loop that forms the perimeter of the graph. This difficulty in counting is reflective of our not having defined what we mean by a “loop.” If we are interested in topological features, what we want to calculate is our “distance,” in a topological “metric”, from a treelike network. We can draw a spanning tree, such as in the right panel of Figure 8.3 and then count how many extra edges are present. These edges are what form the loops and

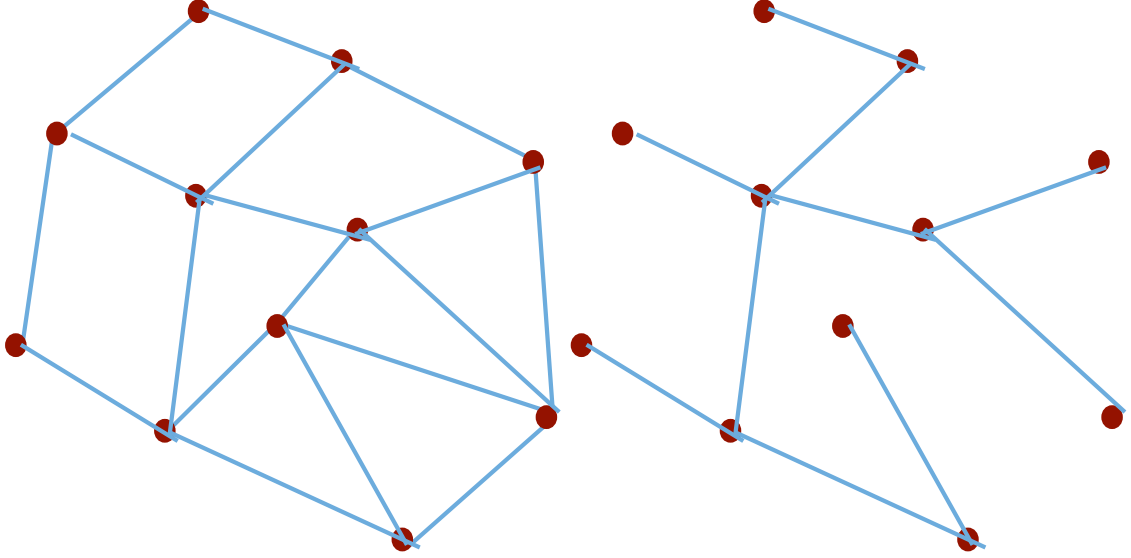


Figure 8.3. How to Count Loops: In the left-hand panel, a graph with 11 vertices and 18 edges is displayed. In the right-hand panel, a spanning tree for this graph is shown. Every edge that is not part of this spanning tree forms a loop and is part of the basis for the cycle space.

provide a way of counting them. Since a spanning tree for V vertices requires $V - 1$ edges, the number of loops, according to this definition, is $L = E - V + 1$, where E is the number of edges. In the example of Figure 8.3, this gives $18 - 11 + 1 = 8$ loops.

These loops correspond to Faces in the graph; Euler's formula tells us that the Euler Characteristic, χ , of a graph is equal to the number of Faces, minus the number of Edges, plus the number of Vertices, as we used in the skeletonization procedure. Solving for the number of faces, after plugging in $\chi = 2$, as the genus of a planar graph is 0^1 , and subtracting 1 for the face that corresponds to the region outside the graph, we get the number of loops. Returning to the spanning tree, when we add edges back in, each new edge is creating exactly one loop. The edges we are adding are in some sense a basis for a linear-algebraic space of loops, as well as forming faces. This space is known as the cycle space, and the loops we are counting are the basis elements of it. If we add two neighboring loops together, modulo 2^2 , we get a larger loop consisting of the perimeter of the two, minus the shared edge(s). Any larger loop that is not part of our original cycle basis is just the sum of linearly independent elements in the cycle basis. Depending on how we draw the spanning tree, we could make any individual loop part of the cycle basis. Consider, for instance, in Figure 8.3, including every segment along the perimeter of the graph except one in the spanning tree. The remaining edge would create a loop in the cycle space: the one formed by the perimeter of the entire

¹ $\chi = 2 - 2g$

²That is, if an edge is counted twice, $1 + 1 \mod 2 = 0$: the edge is not counted at all

graph. By subtracting all the other loops in the cycle basis, we could extract the smallest loop this edge adjoins. Ideally, however, the cycle basis will only be composed of the smallest loops in our graph [60]. The problem of constructing a spanning tree that allows this is a subject of current research.

In the “topological core” of our dataset, there are 253127 edges and 162605 vertices, leading to 90523 loops. With strings preserved, we have 2063110 edges and 1972588 vertices and exactly the same number of loops as in the topological core, a satisfying validation of our algorithms. As promised and as expected from the analogy with leaves, our data is extremely loopy, throwing off our intuitions about what sort of structures would be optimal. To begin to make sense of these loops, we can look at the scale on which they appear. If they are all at the smallest scale, composed of vessels of radius only a few of pixels (or tens of microns) in diameter, we can rationalize them as part of a transition to capillary morphology. We can segment our graph without ever assembling a full adjacency matrix, including the multigraph edges. We start by creating an adjacency matrix that only contains the connection of the largest diameter between two vertices. This link can be found by looking through the list of the edges, sorting by endpoints and then radius. We then censor our new adjacency matrix to only include connections of radius $r > r_t$, those that are larger than a certain threshold. The number of vertices is the number of nonzero rows (or columns). Censoring by vessel radius can be a destructive operation, however, separating regions that had been formerly connected. We need to calculate the number of connected components, which can be done with a simple FLOODFILL on the graph defined by the censored adjacency matrix and add them to the number of Edges. These results are plotted in Figure 8.4.

Examining Figure 8.4, we see a generally exponential distribution of components included versus the minimum vessel radius considered. This relationship is clearest for the number of vertices included. For the number of edges and loops, there is an uptick at the smallest vessel size in both, indicating that the profusion of thin vessels increases the loopiness in the network. All have a decay length of $32 \pm 1.5 \mu\text{m}$. The set length scale present in both geometrical and topological properties suggests robustness in our findings of non-fractality. While we can justify the lack of a pole at zero radius by assuming the smallest hierarchical vessels are not space filling and only drain the capillary mesh at a certain length scale, thus pushing the pole into the realm of a fictional, negative radius, we cannot explain the exponential distribution of components without recourse to different models. We are perhaps seeing hints of the lobular organization of the liver, albeit on a scale considerably smaller than typically expected in anatomy: $\sim 31 \mu\text{m}$ versus $\sim 100 - 500 \mu\text{m}$ traditionally. Perhaps this reflects the packing of the lobules and the existence of many smaller ones deep within the liver.

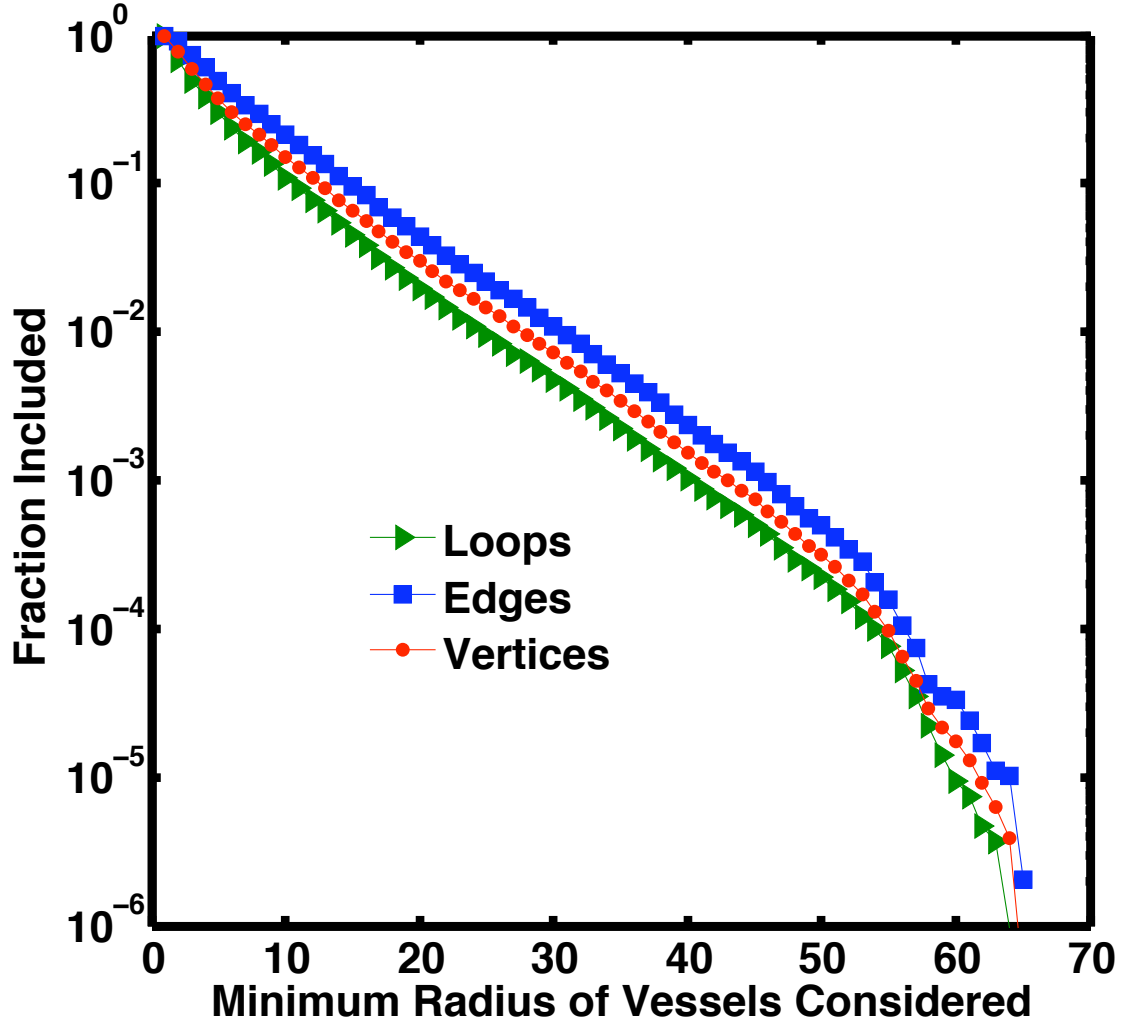


Figure 8.4. Graph Theoretical Properties of the vascular dataset, string included. We plot, on semilogarithmic axes, the fraction of the total loops (green triangles), vertices (red circles), and edges (blue squares) included when considering vessels of radius r or greater (the x axis). This chart should be read from right to left, from only the largest vessels to including progressively smaller ones. Note the exponential distribution of vertices included: this is the same pattern as in the histogram of vessel radii. The decay length is $32 \pm 1.5 \mu\text{m}$. Similarly, note the generally exponential trend in the number of loops, with a small tick upwards when the smallest vessels are considered. The thinnest vessels, thus, are more likely to be anastomoses than the larger ones.

We hope to answer this question by studying orientational order within our dataset. If there is a strong correlation length in the decay of orientational ordering between vessels, we would have considerably more evidence to support this lobular hypothesis. The lobules themselves could be scaled in a power-law fashion, much as in an Apollonian packing. Ultimately, the question will have to be answered by looking at the orientational ordering of the cells themselves, as in Figure 4.1.

We may quantify the relationship between edges and loops by taking the discrete derivative of the number of edges and loops considered in the topological core, then dividing the latter by the former, effectively giving us $\frac{dL}{dE}$, where L indicates the number of loops. This value is plotted in the left panel of Figure 8.5. For most of the range of vessel sizes, there is a constant value of around 0.35, indicating one in three vessels connects two others to form a loop, much as one might expect for a network of triangular loops. When the thinnest vessels are included, this ratio increases, slowly at first, to 0.47 for vessels of radius 3 (11% of vessels) and 0.75 for vessels of radius 1 (23% of all vessels). The smallest vessels, thus, are more likely than not to be anastomoses, and by a significant margin at that. Nearly one third of all loops (32.5%) are created by vessels of radius 1. If this analysis is repeated for the entire dataset, at most 10% of the new edges added form anastomoses: again this occurs for the vessels of radius 1.

Also plotted in Figure 8.5 is the number of connected components. The rampant disconnections present at certain radius cutoffs is troubling. Using the maximum over-edge voxels as the definition of radius instead of the mean greatly ameliorates this problem (not pictured) but does not eliminate it. The disconnected components are nearly always pairs of vertices connected by a single edge: our problem is likely noise in the vessel radii, disconnecting components on the boundary of the graph that lack redundant connections. Additionally, there is no guarantee that vessels will not shrink in size and then reexpand, especially given that the tissue has been through a traumatic series of procedures: perfusion, fixation, density matching, and freezing. Some minor distortions are perhaps to be expected. The problem is most acute for vessels of radius greater than two pixels but smaller than 20, where the largest connected component is approximately constant in size while the number of vertices included increases dramatically. Full connection rapidly returns once the smallest vessels are included as indicated both by the number of components and the sizes of the largest component.

In the future, we hope to use an extension of the Katifori algorithm, devised by Carl Modes (currently a postdoc in the lab), to understand the hierarchy of loops in the network. When applied to nonplanar graphs, the original algorithm breaks down. Consider a three-dimensional cubic lattice; clearly there are loops everywhere, forming the faces of each of the cubes. If we remove one edge, we do not create a typical planar loop. Rather, we create a $+$ sign extruded in the third dimension one

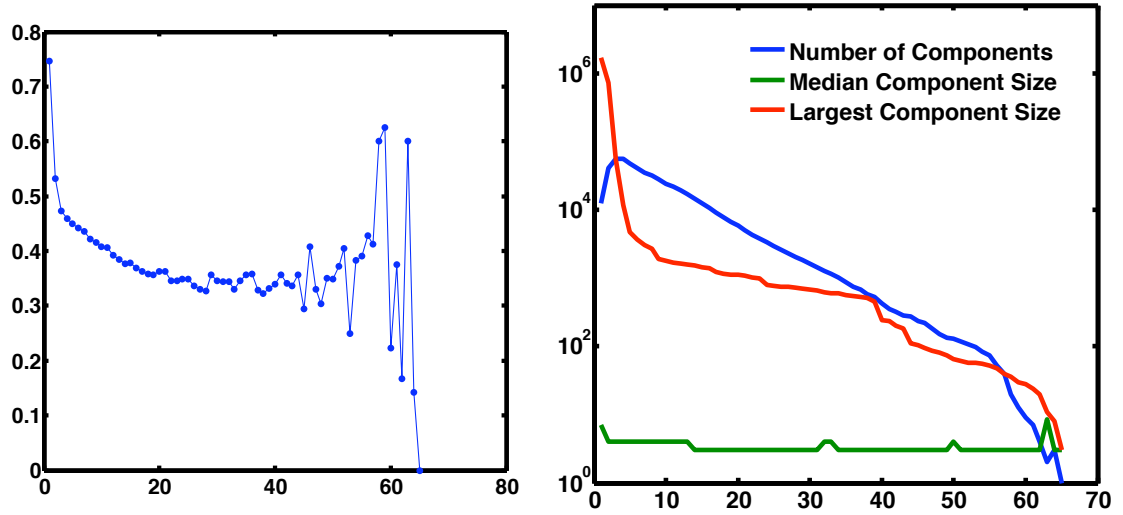


Figure 8.5. Additional Topological Properties. On the left is plotted the $\frac{dL}{dE}$, the discrete derivative (taken from the right hand side) of the number of loops added per number of new edges in the topological core. Apart from some noise at large vessel size, due to the small number of edges and loops therein (see Figure 8.4), there is a relatively constant ratio of about 0.34, suggesting a structure of triangular loops, with a sharp uptick for the thinnest vessels, indicating a greater propensity to be anastomoses. On the right, we have plotted the number of connected components (blue), the median size of those components (green), and the size of the largest component (red) for the network of vessels of radius r or greater. Note that the vast majority of disconnected components are very small and that connectivity is assured by the inclusion of the smallest vessels, for which the number of connected components drops precipitously.

lattice spacing. Four faces of cubes coming together at a common edge that no longer exists, forming a strange structure that cannot be embedded in two dimensions. This situation is clearly untenable: what is needed is to find a surface on which the graph can be embedded (in two dimensions), returning our loops to planarity. This surface will be necessarily contorted and of high genus. It may be found, for generally three-regular graphs, by constructing a spanning tree and cycle basis that contain the smallest loops possible. The few large loops that remain will be signatures of the embedding in non-Euclidean space. There will be an additional “topological” loop for each hole in the surface. If these loops can be identified, then the Katifori algorithm maybe run on the newly embedded graph, giving the hierarchy of loops.

Chapter 9

Prospects in Vasculomics

While we have seen hints of a profound morphological complexity, reflected in the scaling of geometrical and topological properties with vessel size, we are still limited in what we can say about the data. In order to understand what is going on - how the network is formed and what properties it is optimizing - we need a better understanding of what the key variables are, or what the quantitative “knobs” are. Traditionally, confronted with a large number of measurements of a complex system, one would construct a series of theoretical models and test the quantitative predictions of those models versus the data. We believe that, epistemologically, this is the incorrect way to proceed in the case of vascular mapping. What is needed are more experiments, more detailed vascular maps, to allow us to pin down the key features of the “vasculome,” before searching for those features in theoretical models.

9.1 The Paucity of Theory

If there has been one, simple theoretical prediction across models, it is the power-law scaling of $n(r)$, the histogram of vessel radius, with r . We have found an exponential relation not only for radius, but also for the number of vessels of length l , where the clearest error model can explain the deviations from an exponential fit only at the smallest and largest radii, and also for the number of loops, in the network containing only vessels radius r and larger. Our inability to find models that predict exponential scaling indicates a yawning gap between experiment and theory. Clearly, the loopiness of the network has fundamentally changed its statistics. It is possible that no true hierarchy exists. While we may define more and less “important” loops, the order of an individual vessel may not be well-defined. If so, we could not properly define the relations $d(i)$ and $n(i)$, let

alone substitute one into the other, rendering fragile our theoretical predictions.

At the same time, the volumetric argument that also predicts power laws may not completely apply. The hierarchical vasculature drains the capillary beds. While the latter are space filling, it is not clear that the former must scale as a space-filling network. The existence of flow within the capillary “lattice” may strongly change the statistics. The need to be space filling can be counterbalanced by directed flows through preferred channels in the capillary network, allowing for larger spacing between the hierarchical vessels that drain it. In a hierarchical model, the volume in each layer would be constant or a power law, depending on the sum of the radius, length, and bifurcation ratios. We see the existence of a clear peak in the distribution of volume contained in vessels of radius r , shown in Figure 9.1, indicating yet again substantially different network structure. For an exponential distribution of vessel radii and lengths, the volume of vessels of radius r , assuming no correlations between radius and length, would be a constant multiplying $r^2 e^{-r/r_0}$, exactly the type of distribution we find. The existence of weak radius length correlations alters the exponent and the length scale in the theoretical relation to approximately 1.72 and 40 μm respectively. As the relationship between vessel length and radius is neither simple nor easily approximated by a function, we cannot give a deeper analytical explanation of these values.

Even granted rules for developing theoretical models that obey this desideratum, we are faced with an enormous inverse problem. The space of networks that can be developed is enormous. For every modification of a simple network with Poiseuille flow, as used by Katifori and Magnasco, we must decide which complications to introduce (broken bond, multiple sources), choose values of the cost parameter γ and grow the networks in three, not two dimensions. Exploring this space is slow, costly, and not clearly informative. To get the same kind of resolution of network structures and statistics in three dimensions compared with two, we need n^3 lattice sites versus n^2 . Recent work by Katifori and others suggests that the initial choice can have a strong effect on the final network morphology, as the network evolution dynamics are glassy.

Beyond these networks with multiple sources and sinks, the Magnasco group has worked on several other models of network growth and formation in arbitrary dimension. One can formulate a shortest path/geodesic growth law, where the edges that are part of more shortest paths between any pair of points grow preferentially. One may also formulate a Ford-Fulkerson style approach, where each link has both a conductivity and an overall capacity. If one of those properties is updated in response to flow, looped morphologies may be favored as well. Despite these issues, we view it as highly likely that the existence of exponential scaling among components in the network is due to network evolution, rather than an *ab initio* design principle. Anatomy texts make frequent reference

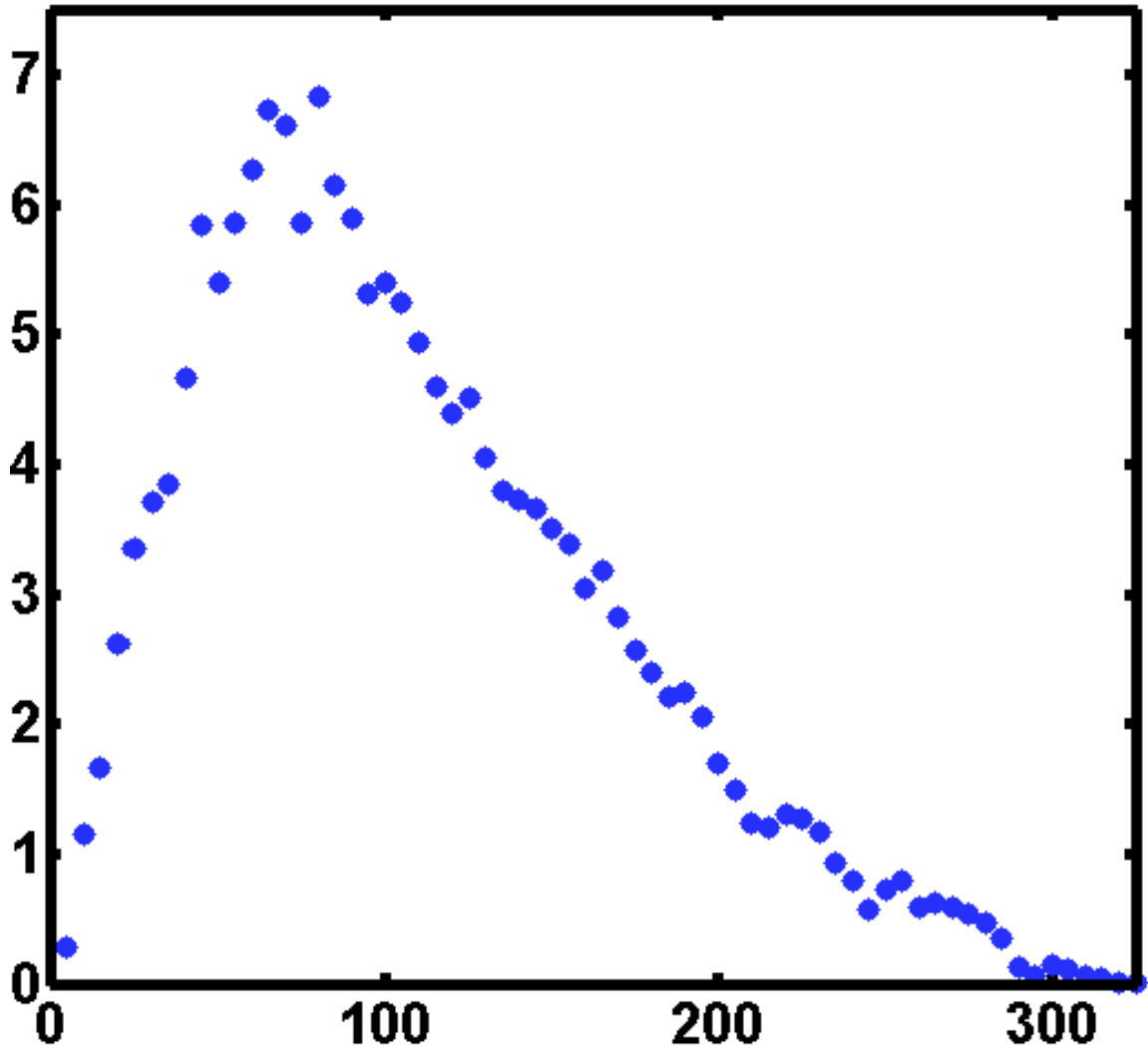


Figure 9.1. The volume in cubic millimeters contained in vessels of radius r , given in microns (one pixel corresponds to five microns). Note the existence of a clear maximum, a feature that cannot be explained by hierarchical models, which would predict a constant or a power-law distribution. The decay length is ~ 8.3 pixels or $41.5 \mu\text{m}$

to the development of the vascular system after birth when the baby’s circulatory system takes over from the mother’s and the placenta stops being the source of oxygenated blood. Some large vessels atrophy, but many more vessels widen, and hierarchy is established among previously similarly-sized vessels. These observations suggest that the proper modeling procedure is to consider an initial lattice (or other graph) of capillaries and update their sizes in response to changing demands [61]. Given these theoretical complexities, however, we would argue that the best way to proceed is to look for naturally perturbed vasculature. If we can see how the statistics change and which features are preserved, we would get a better idea of what the quantitative “knobs” are in the network. What then are the best experiments to perform? Where should we look for perturbations to network statistics?

9.2 Separation of Scales

Throughout this thesis, we have assumed a stark difference in network topology between the capillaries and the hierarchical vasculature. This has been a useful assumption, justifying our decision to image at a resolution that did not capture the capillaries. While grounded in experimental and computational evidence (Chapter 2), it has yet to be confirmed with full-scale vascular mapping. In order to proceed, a full resolution map of the vasculature of an entire organ at 1 μm resolution is necessary. The resulting dataset will be two orders of magnitude larger than ours. Computationally, it would be extremely useful if this hypothesis were true, allowing us to continue work only examining hierarchical vessels.

That said, our data strongly imply this “separation of scales” hypothesis. Stereotypically, capillary beds form in patterns similar to a honeycomb lattice of hexagons. This is the model that the Kleinfeld group proposed for the vascular networks in the mouse cortex [5]. If we turn to the classical picture of the liver, the lobules have generally radial sinusoids that frequently anastomose [61]. Even if this network is not a true lattice, we would expect to see similar statistics, as in computational cell models [1, 32].

From a lattice, one would expect smoothed-delta functions or gaussians for the distributions of vessel radii and lengths. No one vessel is more important than any other, and they all have approximately the same length. We certainly do not see these statistics in Figures 8.1 and 8.2. Similarly, radius and length of vessels would be tightly correlated; while we see a correlation, it is far from perfect, yielding a correlation coefficient of only 0.384, due to the presence of many long thin vessels. This number is likely somewhat of an underestimate. As mentioned previously, due

to our lack of ability to assign a hierarchy or an importance to intersections, the widest vessels are overly subdivided. This introduces a set of large-radius, short-length vessels that are not useful for describing correlations between vessel radius and length.

Topologically, each vertex will connect to six edges, each of which touches two vertices, suggesting that the number of edges should be thrice the number of vertices or half the vertex coordination number. For our full dataset, the number of edges is approximately the same as the number of vertices. In a two-dimensional lattice, each edge would be part of two loops with three edges per loop. In three dimensions, this number would be larger. The number of edges per loop is approximately three over much of our dataset in the topological core (as shown in Figure 8.5), which would suffice for two dimensions. For the smallest vessels, it decreases to slightly over one, but is still far from its value for a three-dimensional lattice. This analogy, too, ignores the treelike components that decorate the topological core. While there may be structural similarities between the rampant anastomosis in the topological core and a two dimensional lattice, the analogy to a capillary network is fraught.

The separation of scales hypothesis would be experimentally and clinically convenient. There would be two vascular morphologies per tissue to characterize, but each could be mapped and analyzed separately, the former with scanning blockface cryotomy, the latter with microCT. In terms of data storage, it would decrease by a factor of around 100 the amount of memory and storage necessary to analyze the data. The only way to prove it, however, is to image an entire tissue or organ at full resolution. We have designed an optical system to replace the Makro lens in our setup that can accomplish precisely this. A macroscope, or documentation microscope, is used for imaging. These devices are designed for industrial use; they make it possible to find micron-scale defects with a large working distance, for use in precision manufacturing processes. They combine a large working distance with a long enough focal length to ensure a not-too-small numerical aperture. Our choice, the Leica Z6 APO has a working distance of up to 97 mm that allows ample distance between the optics and the microtome blade and the sources of cold. With a numerical aperture of 0.117, our effective resolution will be at least $500 \text{ nm} * 1/(2 * 0.117) \approx 2 \text{ }\mu\text{m}$. The Z6 APO also allows for varying degrees of magnification, from $0.57 - 9\times$, making it efficient for imaging only the hierarchical vessels as well.

We have designed a custom fluorescence setup, to allow for epifluorescence imaging while keeping the overall weight of the optics as low as possible¹. We cut a hole into the infinity space of the macroscope, inserted a filter cube, and built an attachment for a CoolLED light source. By changing

¹The ThorLabs axes are only supposed to carry a limited amount of weight.

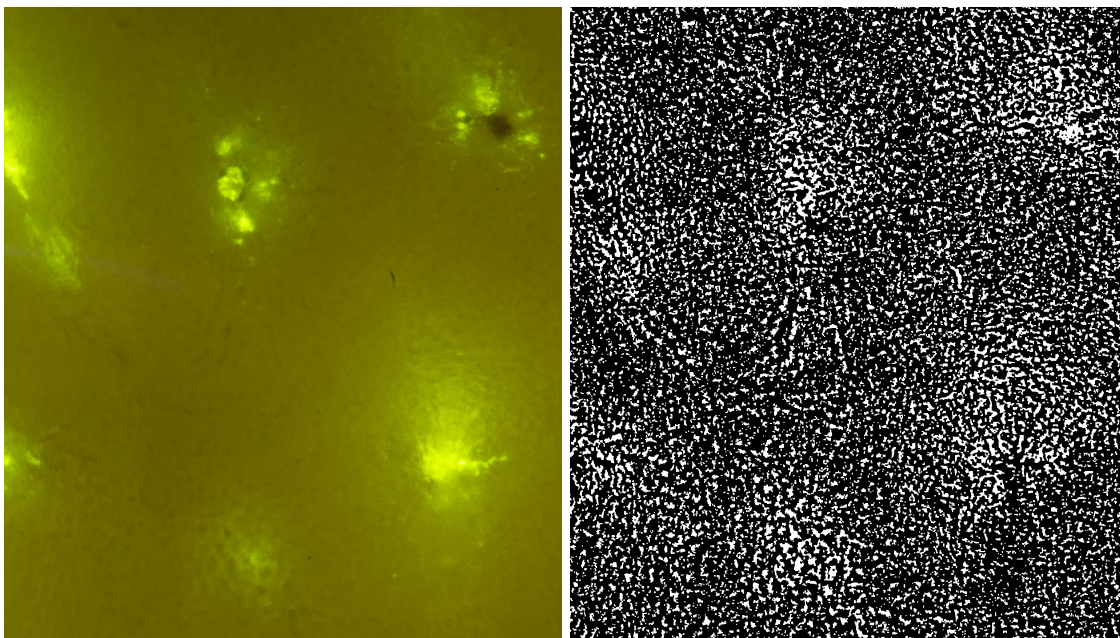


Figure 9.2. Capillaries isolated with macroscope optics. On the left is an image at $9\times$ magnification of a poor perfusion of rat liver (see text for details). Note the wavering pattern across the image, especially clear in front of the bright patches. These changes in brightness are the signatures of the sinusoidal capillaries of the liver, as can be confirmed via dissecting microscope. On the right, we have isolated the capillaries through the use of a relative median filter and morphological operations. Note the radial pattern around the central vein (the bright spots on the left).

the filter cube, we can switch from autofluorescence imaging at 400 nm to fluorescein imaging. In Figure 9.2 below, we show an example of the kinds of images we may take and the ease with which the capillaries may be segmented. We used the Z6 APO with a $1\times$ objective and at maximum zoom for $9\times$ total or about $\frac{2}{3}\mu\text{m}$ per pixel. Our sample was a poorly perfused lobe of rat liver where most of the beads stayed inside the largest vessels and the nearby capillaries, creating bright patches surrounded by small “haloes” of beads. While useless for mapping the hierarchical vasculature, the brightness of the clumps of beads allowed us to map the capillaries surrounding the large vessels using the same segmentation methodology as with the hierarchical vasculature. We took a 20-pixel-radius median filter, subtracted the original image and looked for the relatively bright pixels, performed morphological closing and opening, and arrived at the image in the lower panel of Figure 9.2. Note the radial pattern of the capillaries as in the traditional lobular model of liver structure.

Ideally, with a brighter light source, better optics, and epifluorescence, we will not need to change our contrast agents. If they prove to be insufficient for automatic segmentation, however, we believe

the solution is to adapt one of the resins used for corrosion casting for our fluorescence imaging. We would color the resin with a fluorophore (or else use black resin for a negative image). The most difficult part of this procedure would be finding a resin that could be density matched to the surrounding tissue, to ensure smooth cutting. The use of a resin would ensure perfect boundaries between vessels and the surrounding tissue. Other easier-to-implement solutions we are currently attempting are carboxyfluorescein (a fluorescein that cannot be uptaken by cells) and 2 million molecular weight dextran.

9.3 Where to Look for Perturbations

With this new experimental setup, we propose three different vascular networks to map that are of both theoretical and clinical interest. We desire networks where there are known perturbations that we can look for in the statistics, to help gain proper quantitative “handles” on vascular data. With a better understanding of what features can and cannot change, we will be better able to design and constrain theoretical models of vasculature. Vascular anomalies will also provide hints to the developmental process in showing how it may go astray. Clinically, we are interested in vasculature in cases with a direct tie to human health.

Given these desiderata, a cirrhotic liver is the logical next step. Mouse and rat models of cirrhosis exist and can be easily induced by feeding a a range of toxins to the animal in question. We know that cirrhosis alters the vasculature; perturbations are guaranteed to exist. Given a map, the challenge will be to find which statistics reflect this remodeling and whether the newly grown vasculature follows the statistics of healthy liver. In either case, we will gain insights into the developmental process.

After cirrhosis, the logical next step is to map the vasculature of cancerous hepatic tumors. Given a sense of how the vasculature can go awry, we can test whether or not cancer vasculature is in fact aberrant. If we can tell that it is, the question becomes one of isolating the best statistics to tell whether vasculature is cancerous or healthy for use as a diagnostic tool. If not, the Folkman hypothesis may be incorrect. Similarly, mapping the vasculature of tissue surrounding a tumor, which may have been altered by the demands of the nearby tumor, would be worthwhile. Potentially, vasculature in healthy tissue could provide a diagnostic tool for cancers. Both of these efforts, however, would require a stronger understanding of where to look for vascular abnormalities. A small tumor could be an order of magnitude smaller on a side than the host tissue, greatly limiting the range of size of vessels that we can image.

Ultimately, to make vascular morphology useful as a diagnostic and clinical tool, we must be able to characterize it without having mapped the blood vessels in an entire organ. Statistical anomalies should be more apparent on smaller scales, where there are more vessels that can be altered. Ideally, capillary morphology will not require study either, limiting the necessary scale on the opposite end as well. These statements, however, will remain hypothetical until we have full maps of all the vasculature of an entire organ in both a healthy and a cirrhotic (diseased) state. We have taken the first steps in this effort, developing the necessary histological, optical, image processing, and analytical techniques and presenting the first maps of the hierarchical vasculature of an entire organ. Elegant and convenient theoretical assumptions, such as fractality and a simple hierarchy with loops merely as a decoration, have been shown to be incomplete and a poor approximation of vascular morphology. We may now begin the effort of making vascular topology a useful tool in the medical arsenal.

Bibliography

- [1] BL Zaitlen A Shirinifard, JS Gens. 3d multi-cell simulation of tumor growth and angiogenesis. *PLoS One*, 4(10), October 2009.
- [2] Jayanth R Banavar, Amos Maritan, and Andrea Rinaldo. Size and form in efficient transportation networks. *Nature*, 399(6732):130–132, 1999.
- [3] Albert-László Barabási and Réka Albert. Emergence of scaling in random networks. *science*, 286(5439):509–512, 1999.
- [4] Gilles Bertrand and Grégoire Malandain. A new characterization of three-dimensional simple points. *Pattern Recognition Letters*, 15(2):169–175, 1994.
- [5] Pablo Blinder, Andy Y Shih, Christopher Rafie, and David Kleinfeld. Topological basis for the robust distribution of blood to rodent neocortex. *Proceedings of the National Academy of Sciences*, 107(28):12670–12675, 2010.
- [6] Pablo Blinder, Philbert S Tsai, John P Kaufhold, Per M Knutsen, Harry Suhl, and David Kleinfeld. The cortical angiome: an interconnected vascular network with noncolumnar patterns of blood flow. *Nature neuroscience*, 16(7):889–897, 2013.
- [7] Steffen Bohn and Marcelo O Magnasco. Structure, scaling, and phase transition in the optimal transport network. *Physical review letters*, 98(8):088702, 2007.
- [8] M. Born, E. Wolf, and A.B. Bhatia. *Principles of Optics: Electromagnetic Theory of Propagation, Interference and Diffraction of Light*. Cambridge University Press, 1999.
- [9] T.D. Boyer, M.P. Manns, A.J. Sanyal, and D. Zakim. *Zakim and Boyer’s Hepatology: A Textbook of Liver Disease*. Saunders W.B. Saunders/Elsevier, 2012.
- [10] J.D. Bronzino and D.R. Peterson. *Tissue Engineering and Artificial Organs*. The Biomedical Engineering Handbook, Third Edition. Taylor & Francis, 2006.

- [11] Thomas Caceci. Exercise 20: Accessory glands of the digestive tract, apr 2014.
- [12] UK Natural History Museum Micro-CT Scanning Center. Micro-ct scanning requests, costs and protocol, apr 2014.
- [13] Keystone College and The Countryside Conservancy. Tunkhannock creek watershed atlas, 2011.
- [14] Open Stax College. Circulatory system from anatomy and physiology, apr 2014.
- [15] Anna Cleta Croce, Uliana De Simone, Mariapia Vairetti, Andrea Ferrigno, Eleonora Boncompagni, Isabel Freitas, and Giovanni Bottiroli. Liver autofluorescence properties in animal model under altered nutritional conditions. *Photochemical & Photobiological Sciences*, 7(9):1046–1053, 2008.
- [16] Winfried Denk and Heinz Horstmann. Serial block-face scanning electron microscopy to reconstruct three-dimensional tissue nanostructure. *PLoS biology*, 2(11):e329, 2004.
- [17] Peter Sheridan Dodds and Daniel H Rothman. Unified view of scaling laws for river networks. *Physical Review E*, 59(5):4865, 1999.
- [18] Peter Sheridan Dodds and Daniel H Rothman. Geometry of river networks. ii. distributions of component size and number. *Physical Review E*, 63(1):016116, 2000.
- [19] Peter Sheridan Dodds, Daniel H Rothman, and Joshua S Weitz. Re-examination of the 3/4-law of metabolism. *Journal of Theoretical Biology*, 209(1):9–27, 2001.
- [20] Paul Erdos and Alfréd Rényi. {On the evolution of random graphs}. *Publ. Math. Inst. Hung. Acad. Sci*, 5:17–61, 1960.
- [21] Hiroshi Hama, Hiroshi Kurokawa, Hiroyuki Kawano, Ryoko Ando, Tomomi Shimogori, Hisayori Noda, Kiyoko Fukami, Asako Sakaue-Sawano, and Atsushi Miyawaki. Scale: a chemical approach for fluorescence imaging and reconstruction of transparent mouse brain. *Nature neuroscience*, 14(11):1481–1488, 2011.
- [22] William Harvey. *Exercitatio Anatomica de Motu Cordis et Sanguinis in Animalibus*. P.F. Collier & Son, New York, 1909 (1628).
- [23] Sven Hirsch, Johannes Reichold, Matthias Schneider, Gábor Székely, and Bruno Weber. Topology and hemodynamics of the cortical cerebrovascular system. *Journal of Cerebral Blood Flow & Metabolism*, 32(6):952–967, 2012.

- [24] Rakesh K Jain. Normalizing tumor vasculature with anti-angiogenic therapy: a new paradigm for combination therapy. *Nature medicine*, 7(9):987–989, 2001.
- [25] Eleni Katifori and Marcelo O Magnasco. Quantifying loopy network architectures. *PloS one*, 7(6):e37994, 2012.
- [26] Eleni Katifori, Gergely J Szöllösi, and Marcelo O Magnasco. Damage and fluctuations induce loops in optimal transport networks. *Physical review letters*, 104(4):048704, 2010.
- [27] Moritz A Konerding, Aslihan Turhan, Dino J Ravnice, Miao Lin, Christine Fuchs, Timothy W Secomb, Akira Tsuda, and Steven J Mentzer. Inflammation-induced intussusceptive angiogenesis in murine colitis. *The Anatomical Record*, 293(5):849–857, 2010.
- [28] T Yung Kong and Azriel Rosenfeld. Digital topology: introduction and survey. *Computer Vision, Graphics, and Image Processing*, 48(3):357–393, 1989.
- [29] Ta-Chih Lee, Rangasami L Kashyap, and Chong-Nam Chu. Building skeleton models via 3-d medial surface axis thinning algorithms. *CVGIP: Graphical Models and Image Processing*, 56(6):462–478, 1994.
- [30] S Lobregt, PW Verbeek, and FC Groen. Three-dimensional skeletonization: principle and algorithm. *IEEE Transactions on Pattern Analysis and Machine Intelligence*, 2(1):75–77, 1980.
- [31] Benjamin Mauroy, M Filoche, ER Weibel, and B Sapoval. An optimal bronchial tree may be dangerous. *Nature*, 427(6975):633–636, 2004.
- [32] Shirinifard A Merks RM, Perryn ED. Contact-inhibited chemotaxis in de novo and sprouting blood-vessel growth. *PLoS Computational Biology*, 4(9), September 2008.
- [33] K.L. Moore, A.F. Dalley, and A.M.R. Agur. *Clinically Oriented Anatomy*. Clinically Oriented Anatomy. Lippincott Williams & Wilkins, 2006.
- [34] DG Morgenthaler. *Three-dimensional simple points: serial erosion, parallel thinning, and skeletonization, Technical Report TR-2005*. University of Maryland at College Park. Computer Science Center, 1981.
- [35] Cecil D Murray. The physiological principle of minimum work applied to the angle of branching of arteries. *The Journal of General Physiology*, 9(6):835–841, 1926.

- [36] Cecil D Murray. The physiological principle of minimum work: I. the vascular system and the cost of blood volume. *Proceedings of the National Academy of Sciences of the United States of America*, 12(3):207, 1926.
- [37] JA Nagy, SH Chang, AM Dvorak, and HF Dvorak. Why are tumour blood vessels abnormal and why is it important to know&quest. *British journal of cancer*, 100(6):865–869, 2009.
- [38] M. Nakahara. *Geometry, Topology and Physics, Second Edition*. Graduate student series in physics. Taylor & Francis, 2003.
- [39] Thi-Hiep Nguyen and Byong-Taek Lee. The effect of cross-linking on the microstructure, mechanical properties and biocompatibility of electrospun polycaprolactone–gelatin/plga–gelatin/plga–chitosan hybrid composite. *Science and Technology of Advanced Materials*, 13(3):035002, 2012.
- [40] Karl J Oldhafer, Gregor A Stavrou, Guido Prause, Heinz-Otto Peitgen, Tim C Lueth, and Stefan Weber. How to operate a liver tumor you cannot see. *Langenbeck’s archives of surgery*, 394(3):489–494, 2009.
- [41] Keiichiro Ono. Scale free network generated by barabasi-albert model, jul 2007.
- [42] Lars Onsager. Reciprocal relations in irreversible processes. i. *Phys. Rev.*, 37:405–426, Feb 1931.
- [43] Jacob N Oppenheim and Marcelo O Magnasco. Topological phase transition in the scheidegger model of river networks. *Physical Review E*, 86(2):021134, 2012.
- [44] Kálmán Palágyi. Skeletonization in 3d via thinning and its applications, lecture notes, 2012.
- [45] Christopher R Parish. Cancer immunotherapy: The past, the present and the future*. *Immunology and cell biology*, 81(2):106–113, 2003.
- [46] J.I.M. Poiseuille. *Recherches sur les causes du mouvement du sang dans les vaisseaux capillaires*. Academie des Sciences Tome VII Savans Etranges, Paris, 1835.
- [47] renatoksheet. Mathematical morphology, jul 2008.
- [48] Don C Rockey, Stephen H Caldwell, Zachary D Goodman, Rendon C Nelson, and Alastair D Smith. Liver biopsy. *Hepatology*, 49(3):1017–1044, 2009.

- [49] Ignacio Rodríguez-Iturbe and Andrea Rinaldo. *Fractal river basins: chance and self-organization*. Cambridge University Press, 2001.
- [50] John C Russ. *The image processing handbook*. CRC press, 2010.
- [51] Adrian E Scheidegger. *Theoretical geomorphology*. Springer Verlag, Berlin, third edition, 1991.
- [52] AE Scheidegger. A stochastic model for drainage patterns into an intramontane trench. *Hydrological Sciences Journal*, 12(1):15–20, 1967.
- [53] Alexander M Seifalian, Alok Tiwari, George Hamilton, and Henryk J Salacinski. Improving the clinical patency of prosthetic vascular and coronary bypass grafts: the role of seeding and tissue engineering. *Artificial organs*, 26(4):307–320, 2002.
- [54] Dirk Selle, Bernhard Preim, Andrea Schenk, and H-O Peitgen. Analysis of vasculature for liver surgical planning. *Medical Imaging, IEEE Transactions on*, 21(11):1344–1357, 2002.
- [55] Thomas F Sherman. On connecting large vessels to small. the meaning of murray’s law. *The Journal of general physiology*, 78(4):431–453, 1981.
- [56] Matthew L Springer, Tze Kin Ip, and Helen M Blau. Angiogenesis monitored by perfusion with a space-filling microbead suspension. *Molecular Therapy*, 1(1):82–87, 2000.
- [57] Sargur N Srihari, Jayaram K Udupa, and MM Yau. Understanding the bin of parts. In *Proceedings IEEE Conference on Decision Control*, pages 44–49, 1979.
- [58] the igraph project. the igraph library: screenshots, apr 2014.
- [59] Yea-Fu Tsao and KS Fu. A 3d parallel skeletonwise thinning algorithm. In *Proc. IEEE PRIP Conf*, pages 678–683, 1982.
- [60] Oswald Veblen. An application of modular equations in analysis situs. *The Annals of Mathematics*, 14:86–94, 1912.
- [61] Roger Warwick and Peter L. Williams, editors. *Gray’s Anatomy*. W.B. Saunders Company, Philadelphia, 35th british edition edition, 1973.
- [62] Duncan J Watts and Steven H Strogatz. Collective dynamics of small-worldnetworks. *nature*, 393(6684):440–442, 1998.
- [63] Geoffrey B West, James H Brown, and Brian J Enquist. A general model for the origin of allometric scaling laws in biology. *Science*, 276(5309):122–126, 1997.

- [64] Ed Yong. Replacement parts. *SCIENTIST*, 26(8):26–31, 2012.